UNIVERSITAT
POLITÈCNICA
DE VALÈNCIA

New Non-Destructive Testing techniques based on mechanical waves: Development and application to damage characterization on non-homogeneous materials

by
Vicente Genovés Gómez

supervised by
Dr. Jordi Payá Bernabeu
Dr. Jorge Gosálbez Castillo

València, Spain
November 2018

A mi Mamá

Abstract

This doctoral thesis is developed in materials, Non-Destructive Testing (NDT) and signal processing fields. Its purpose is to make a contribution in new non destructive techniques focusing in its development and application to real systems. Durability and damage evaluation in non-homogeneous materials is the keystone of this document, assembling the structure in two main chapters. In the first instance the behaviour of Glass-fiber Reinforced Cement under bending test is evaluated. Multiple ultrasonic signals during the deformation process of the specimens were acquired, implementing a new multi-frequency acquisition technique. After the acquisition stage, linear and non-linear parameters were calculated from the pulsed ultrasonic signals correlating those parameters with the stress strain curve described during the test. In the third chapter, the impact spectroscopy analysis applied to chemical and thermal damaged mortar samples is exposed. The non-linear histeretic behaviour of the mortar specimens was studied more in depth. The analysis of the dynamic modulus softening with increment of the excitation amplitude is a hot spot at this moment for damage evaluation, being the current technique depending on the multiple signals acquisition. In this context, a new technique is proposed which allows a non-linear parameters extraction from a single reverberation signal.

Resumen

Esta tesis doctoral se encuentra desarrollada en los ámbitos de materiales, ensayos no destructivos y procesado de señal. Su propósito es aportar nuevas técnicas no destructivas centrándose tanto en su desarrollo como en su aplicación a sistemas reales. La evaluación de durabilidad y daño en materiales no homogéneos es el eje central de este documento, articulándolo en dos capítulos fundamentales. En primera instancia se evalúa el comportamiento del cemento reforzado con fibra de vidrio bajo esfuerzo de flexión. Múltiples señales ultrasónicas fueron adquiridas en todo el proceso de deformación de los elementos implementando una nueva técnica de adquisición multifrecuencia. En la fase posterior a la adquisición se determinaron parámetros lineales y no lineales de las señales ultrasónicas pulsadas correlacionando dichos parámetros con las curvas tensión - deformación descritas por los elementos ensayados. En el último bloque se expone el análisis de espectroscopía por impacto sobre probetas de mortero dañadas química y térmicamente. Se profundizó sobre el comportamiento dinámico no-lineal e histéretico de los elementos de mortero. El análisis del ablandamiento del módulo dinámico con el incremento de la amplitud de excitación es un tema de gran interés para la evaluación de daño, siendo la técnica actual dependiente de la adquisición de múltiples señales. En este contexto, se propone nueva técnica de procesado de señal capaz de extraer parámetros de esta naturaleza a partir de una única señal.

Resum

Aquesta tesi doctoral està desenvolupada als àmbits de materials, assajos no destructius i processament de senyals. El seu propòsit és aportar noves tècniques no destructives, centrades tant en el seu desenvolupament com en la seua aplicació a sistemes reals. L'avaluació de durabilitat i dany en materials no homogenis és l'eix central d'aquest document, format per dos capítols fonamentals. En primer lloc s'avalua el comportament del ciment reforçat amb fibra de vidre sotmès a esforç de flexió. Diverses senyals ultrasòniques van ser adquirides durant tot el procés de deformació dels elements que implementa una nova tècnica d'adquisició multifreqüència. En la fase posterior a l'adquisició es van determinar paràmetres lineals i no lineals de les senyals ultrasòniques polsades que correlacionen aquests paràmetres amb les corbes de tensió-deformació descrites pels elements assajats. Al tercer bloc s'exposa l'anàlisi d'espectroscòpia per impacte en provetes de morter malmeses químicament i tèrmicament. Es va aprofundir en el comportament dinàmic no lineal i histerètic dels elements de morter. L'anàlisi de l'estovament del mòdul dinàmic amb l'increment de l'amplitud de l'excitació és un aspecte molt interessant per a l'avaluació de dany, tècnica que actualment depèn de l'adquisició de diverses senyals. En aquest context, es proposa una nova tècnica de processament de senyal capaç d'extraure paràmetres d'aquesta natura a partir d'una única senyal.

Contents

Chapter 1

Introduction

This thesis has been written following the journal publishing modality, so it has been composed as a sum of five papers published in a JCR journals, one international congress and two papers submitted for publication. The reference to each publication is pointed out with a superscript number, appearing listed in Bibliography Chapter. Moreover, at the end of the document, papers and congress proceedings originated from this thesis have been pointed out but not included in the document for narrative and extension reasons (Chapter 5).

Given this context, in this chapter, a general approach with the aim of contextualize the reader is presented. The scope and structure of the thesis is commented at the end of this chapter.

The thesis organization not only follows logical order of research work within each chapter, but also the chronological order in which this study was developed. So that, the reader will go forward through the scientific achieved objectives, and also through the quality and accuracy of the formulated mathematics and later on analysis. All these aspects take part in the training evolution of the thesis author.

1.1 General approach

Lets take a rubber and tightly squeeze its surface. At this point you will notice two effects: An axial deformation and a transverse strain. The rubber is following the Hook's law and it is behaving close to a linear spring. However, it is affected by the so called Poisson's effect which implies a deformation in the perpendicular direction of the applied load. It is possible to assign then a property to this phenomena. Stiffness is a mechanical property described as the resistance of an object to be deformed when a force is applied. Thus, it could be reasonable to think that stiffer materials are better than softer ones, but, certainly, the goodness mostly depends on its usage. For that reason we never use polyurethane to make the pillars of a skyscraper and we will not use steel to coat the walls of the same building. Strength performance and acoustic insulation are two different uses that exploits the same material property. The difference is, for the first one, we need to absorb mechanical waves propagating through the air, requiring huge deformations to improve the damping of the sound waves. However, to hold the entire structure, bear the wind load, and be resistant to different structural actions, a high stiffness is required to avoid excessive deformations of the structural elements which would lead to irreversible damages in the building. Materials engineering is a wide field in science that takes care of several type of materials, with different properties, at different scales, natures, performance... Materials in our world play a key role in the development of societies, from sustaining most of great structures to incredible tiny systems allowing astonishing electrical and thermal properties. In general, there is no good or bad material in general but knowing and understanding about the properties and performance of each substance becomes essential.

Ultimately, the aim of this thesis is to show the importance of getting information from inside the structure of materials, providing newer and proper tools to analyse more in depth than common techniques and the naked eye. Also, exploding the metadata concept (the information inside the information), showing the critical importance that the signal processing has, squeezing the signals to show more and powerful information than the equipments and electronics provides at the first instance. Thus, with these tools we are able to extract new parameters and variables to know more closely the underlying phenomenons behind the materials responses to certain conditions. Variables are the messengers that give us all the information about our physical reality, like a puzzle. It is really complicated to make a puzzle with missing pieces or without having a big picture of the final result: if you miss some pieces or have a wrong reference of the reality you will not be able to understand anything. There are two options. Get more parts of your jigsaw or recompose your hypothesis. Or both. Some beautiful example for that is related to heat, molecules and atoms. Here is the statement: heat expands the matter. Heat increases the relative distance between atoms and molecules, changing its properties and reducing the density of the system. Now you can observe how an ice cube is floating over your drink. Here it is, part of the puzzle does not match with the reality, so we are forced to recompose our first statement: heat expands most matter. But certainly, we really want to know what is happening to the water (and other substances), so we need to see in other places, searching for other causes that forces water to increase its volume after some temperature threshold. Water is strongly related to our first statement, beyond the 4 °C. As the temperature increases, distance between hydrogen and oxygen in the water molecule increases, giving it more freedom. Also, the distances between molecules rises as a result of the forced motion induced by the heat. However, before 4 °C, molecules of water begin to experiment a deceleration process, reducing the relative motion between them. That happens also with all the matter, the difference is found in the structure of water itself, in the geometry of the water molecule. Water is a polar molecule, that means, it has a positive pole and a negative pole. The oxygen atom represents the negative pole while the two atoms of hydrogen the positive one. So that, the two hydrogen atoms describe an angle with the oxygen so, when temperature decreases, all the atoms begin to get closer to conserve the principle of minimum energy. But, when the electromagnetic forces between the two hydrogen atoms are too strong, the molecule cannot continue decreasing its volume because bringing the particles closer results in a huge waste of energy. As a consequence, nature tries to found another way to keep the particles organized with the minimum energy possible, crystallizing in a beautiful three dimensional hexagonal structure, occupying more space than the liquid state. This example of how we underestimate the physical reality seems to be far away from the scope of this work. Not at all. In Section 3.4 we had the same experience with mortar samples, starting our experimental program with a wrong big picture of the final result. The data did not match with our hypothesis and we were forced to see in other places, looking for an answer and, certainly, doubting about ourselves: wrong acquisitions, bad data processing, missing results... The end of this story was astonishing. Missing pieces of the puzzle and bad starting hypothesis. The physical reality was something much more fascinating than our expectations.

The need to have as much information as possible to understand what is happening to our systems, to our structures, to our materials, is very remarkable. Only having information from different angles and perspectives will bring us the opportunity to identify each degradation mechanisms that materials experiment in real applications. This is why we bet for the powerful combination between Non-Destructive Tests and Signal Processing. Traditionally, these fields have been separated with no interaction between them. On one side, we had valuable information adopting the shape of signals, sines, echoes, reflections... we had a lot of information encrypted, waiting to be understood. On the other hand, we had astonishing scripts, algorithms and beautiful maths. A lot of potential inside a tiny box, meaningless, waiting to be released and shed light. As an example, the first work which explodes all this potential so far can be found in the ISI Journal work in Chapter 5, "*Ultrasonic signal modality: A novel approach for concrete damage evaluation*" and continues with an international conference communication in Washington, "*An Advanced Ultrasonic Method based on Signal Modality for Structural Damage Characterization on Concrete: The Cube Problem*". Literally we put the two ingredients together, huge amount of acquired signals and the correct signal processing algorithm, obtaining in this way incredible results that allowed us to see much more inside a chemical attack on concrete. Things that we totally ignored before.

Definitely, the decision to work together in a multidisciplinary team to see more than we see individually was a challenging but beautiful decision. It improved in a large scale our understanding about signals and materials and also allowed us to learn new concepts totally alien to our respective fields. The things we learnt together and the way we managed the combined knowledge have much more value than the knowledge itself from my own point of view.

1.2 Objectives and Structure

The main matter of this work is to develop new non-destructive methods and procedures to characterize materials and use those to know the variation of its properties when a change in its condition is applied. We found that is an important contribution to the science community and industry: understanding and following the evolution of materials with time under different states is the cornerstone to characterise any situation in continuous media. Therefore, it will allow to reach a higher level of comprehension and knowledge about materials, dynamics and wave propagation, granting the know-how to develop real applications and industrial uses. For this, the specific objectives could be detailed by chapters.

Chapter 2 is focused on the characterisation of Glass-fiber Reinforced Cement (GRC) with ultrasonics. The continuous monitoring of the GRC samples under mechanical stress and knowing the properties of the material as the deformation (and damage) increases provide valuable information of the cracking and micro-cracking process. For that, a through-transmission continuous acquisition system was developed in order analyse the material response in a wide range of frequencies. Thus, we have established four stages. In Section 2.1, the characterisation with frequency sweep ultrasonics of different types of GRC in static test is done. The monitoring of four point bending test with ultrasonics at a fixed frequency is described in Section 2.2. In Section 2.3, the developing of a broadband ultrasonic signal method to obtain the frequency response of ultrasonic waves in non-homogeneous materials is described. Finally, in Section 2.4, a complete monitoring of the bending test on GRC plates with broadband signals is carried out in order to obtain non-dependant and dependant frequency parameters during the whole flexural event.

The scope of Chapter 3 is to deeply analyse the reverberation stage of mortar specimens, calculating linear and non-linear parameters and proposing a new signal processing algorithm to extract new features about the relaxation process of a specimen under an impact excitation. This chapter is not only focused on impact resonance, but also contains ultrasonics measurements with the aim to complement the results and shed light to complex damage processes in mortar samples. Section 3.1 tries to evaluate the ageing process of GRC plate samples by means of linear and non-linear acoustics parameters. Section 3.2 evaluates the internal sulphate attack on mortar samples by means of ultrasonic and impact acoustic methods. In Section 3.3, a complete thermal damage monitoring on mortar samples was performed using acoustic non-linear methods, ultrasonics and physical and mechanical techniques in order to understand the physical mechanisms under this kind of damaging conditions. In Section 3.4, a new technique developed in this thesis was evaluated using thermal damaged samples in order to know the robustness and reproducibility of its results. General conclusions and future investigations are addressed in Chapter 4. Moreover, a list of published works in ISI Journals, conferences and patents related to the thesis are given in Chapter 5 .

Chapter 2

Frequency sweep ultrasonics: Case on bending test monitoring on Glass-fiber Reinforced Cement

The scope of this chapter is to evaluate the mechanical evolution of Glass-fiber Reinforced Cement plates under flexural stress. This material has interesting properties in construction and building engineering due to the exceptional toughness given by the contribution of glass-fibers. These fibers allow the material to bend avoiding brittle breakage leading the samples to reach more deformation before the point of fracture. Under these conditions, detecting the first crack and its propagation, the assessment of the micro-cracking process in the matrix is essential because it determines the performance of the whole system. Thus, this chapter characterise the material to know its ultrasonic and mechanical properties at the beginning in order to monitor different parameters depending on its stress state and also its dosage.

The first section describes the features of GRC plates in resting conditions. The scope of this work is to characterise and find the differences between ultrasonic, mechanical and microstructure parameters between two dosages of GRC. The core of this study is the ultrasonic analysis and its correlation with mechanical and microstructural tests. Ultrasonic velocity and wave attenuation at different injected frequencies were extracted and the main differences found with the other tests was successfully represented (Section 2.1). After this study, the ultrasonic layout and the signal processing was in the perfect disposition to arrange a dynamic experiment when the properties of the material varies with testing loading. In the second section the specimens were subjected to a four point bending test while measured with an ultrasonic layout. Due to the quick change of the stress conditions of the samples, fixed frequency tone burst signals were used. This study allowed us to identify the differences in velocity, energy, attenuation and non-linearity of the injected wave in each instant of time during the flexural test (Section 2.2). In the third section of this chapter an optimized ultrasonic measurement was developed. The purpose of this method was to reduce significantly the acquisition time in a frequency sweep layout. The use of broadband signals were deeply analysed and compared with burst and continuous signals. This method also allowed to measure materials when time is a critical variable (Section 2.3). Section 2.4 was the combination of Section 2.2 and Section 2.3: four point bending test monitored with broadband (chirp) signals obtaining a lot of information of the condition of the material under stress. All the parameters extracted from Section 2.2 developed a frequency dimension, showing interesting results about the cracking propagation and micro-cracking process as the test evolved.

The sequential investigation in this chapter allowed us to optimize a procedure where the time is a critical variable. In the course of this chapter, all the steps from a fiber reinforced material characterisation to capture the material response under a continuous changing stress field were described. The procedure demonstrates to be consistent and robust and perfectly applicable to other materials and mechanical testing methods. Thus, this technique is also suitable for different phenomena when an effective and quick acquisition system with frequency dependant parameters is required.

2.1 Ultrasonic characterization of GRC with high percentage of fly ash substitution[1]

[1] *V. Genovés, J. Gosálbez, R. Miralles, M. Bonilla, and J. Payá. "Ultrasonic characterization of GRC with high percentage of fly ash substitution," Ultrasonics, vol. 60, pp. 88–95, 2015.*

Abstract

New applications of Non-Destructive Testing (NDT) techniques with ultrasonic tests (attenuation and velocity by means of ultrasonic frequency sweeps) have been developed for the characterization of fibre-reinforced cementitious composites. According to new lines of research on glass-fibre reinforced cement (GRC) matrix modification, two similar GRC composites with high percentages of fly ash and different water/binder ratios will be studied. Conventional techniques have been used to confirm their low $Ca(OH)_2$ content (Thermogravimetry), fibre integrity (Scanning Electron Microscopy), low porosity (Mercury Intrusion Porosimetry) and good mechanical properties (Compression and four points bending test). Ultrasound frequency sweeps allowed the estimation of the attenuation and pulse velocity as functions of frequency. This ultrasonic characterization was correlated successfully with conventional techniques.

2.1.1 Introduction

Glass-fibre Reinforced Cement (GRC) is a composite made of Portland cement mortar with low water/cement (w/c) ratio with a large amount of paste in relation to the aggregate quantity. Addition of a high proportion of glass fibres to the mortar matrix (3%–5% by weight of mortar) improves the mechanical properties of the elements formed with this material, especially the toughness and ductility. This composite has an important role in non-steel reinforced pre-cast concrete elements, such as sheets, panels, and other slim shapes usually employed in building engineering and architecture, and also in cast-in-situ sprayed-on surfaces [1, 2].

The most important problem with this kind of material is the glass-fibre degradation. Exposure of the glass fibres to an alkaline environment (e.g.: the Portland cement matrix) leads to a rapid degradation process which involves strength and weight losses, and reduction in the filament diameter. This process can be attributed to the breaking of the Si–O–Si bonds in the glass network, by the OH^- ions which are present in high concentration in the pore solution of the cement matrix [2, 3].

For that reason, research on this topic has focused on three main lines:

1. Fibre modification, making it more stable to a highly alkaline environment;
2. Matrix modification, adding moderate quantities of pozzolanic powders partially substituting for the Portland cement content;
3. Fibre and matrix modification at the same time.

As to fibre modification investigations, research has focused on modifying the chemical composition of the glass (e.g.: ZrO_2), which makes the system more chemically stable in alkaline solutions [3, 4], and fibre-coating modification [5, 6].

As to matrix modification, several authors have reported successful results by means of the partial replacement of cement by reactive mineral admixtures such as silica fume, fly ash, metakaolin or blast-furnace slag. These modifications of the matrix have resulted in an improvement of the fibre–matrix interface, partially inhibiting fibre degradation due to the reduction of the pH level and the $Ca(OH)_2$ content [7–10]. Thus, the mechanical properties of the GRC specimens are improved significantly. Usually, the characterization of this kind of cement composite is carried out through conventional techniques such as X-ray diffraction, thermogravimetry, and mechanical tests [10, 11].

Recently, several researchers have focused on non-destructive concrete and mortar characterization in order to obtain more reliable information and new aspects of cementitious composites without damaging the specimen under test. During recent years, Non-Destructive Test (NDT) techniques applied to concrete have been investigated, especially ultrasonics and acoustic spectroscopy, in order to obtain parameters related to the physical and mechanical properties of the material [12]. Some experimental studies have demonstrated that wave parameters such as the ultrasonic pulse velocity of P-waves are suitable to predict the dynamic elastic modulus of concrete, and also S-waves for its dynamic shear modulus. These parameters are proportional to the elastic and shear modulus of concrete and also to its compressive strength [13, 14]. Other studies based on ultrasound propagation indicate that wave attenuation can be measured for various frequencies, in order to define different cementitious materials, distinguishing their microstructure, porosity, and other qualities in both the hardened [15–18] and the fresh state [19]. Some studies have shown interesting correlations between other properties of cementitious composites, such as their permeability or porosity, with ultrasonic parameters such as pulse velocity, signal attenuation, or reflection coefficients, using a specific test setup [20].

NDT techniques for characterizing GRC specimens have been applied: acoustic resonance techniques (Non-linear Impact Resonance Acoustic Spectroscopy, NIRAS) and ultrasonic guided waves have been used to obtain more information about the composite material and its ageing process than traditional tests on GRC [21]. The scope of this study is to characterize GRC specimens with high substitutions of the cement content by fly ash. As a novelty for fibre-reinforced cementitious composites, the characterization will be carried out by means of ultrasonic frequency sweeps that will allow obtaining ultrasonic parameters as functions of the frequency. The frequency response will be correlated with the porosity and the mechanical behaviour of this type of material. Thermogravimetry and scanning electron microscopy will be used to assess the pozzolanic reaction and fibre integrity.

2.1.2 Experimental

2.1.2.1 Materials

Two different matrices with the same type of glass fibre and content were designed, as can be seen in Table 2.1.1. In both mixtures the proportion of Portland cement to fly ash was 40/60.

Table 2.1.1: Dosages (in grams) used on GRC plate manufacturing.

Material	Type	fa-035 [g]	fa-030 [g]
Cement	CEM I-52,5 R	726	726
Fly Ash	F*	1089	1089
Water	-	635.25	544.50
Aggregate	Silica sand 0/2	1216	1216
Superplastizicer	Policarboxilate ether	3.50	7
Fibre**	Glass AR 12 mm ⌀12 μm	73.50	73.50

* ASTM C-618

** Cem-FIL® 62 82Tex

The raw materials and their brief description are summarized in Table 2.1.1. The main difference between both composites was the water/binder (w/b) ratio: fa-035 corresponds to 0.35 w/b ratio whereas fa-030 corresponds to 0.30 w/b ratio. The plates used for the ultrasonic tests and the four-point bending test were manufactured according to the BS EN 1170-5 standard [22]. In this experiment, a 400 × 400 × 20 mm^3 mother plate was chosen, according to the standard, seven specimens of 325 × 50 × 20 mm^3 were prepared by cutting the hardened mother plate. Three mortar specimens of each series (40 × 40 × 160 mm^3) were manufactured for the compressive strength test. A sample of each series was taken for Mercury Intrusion Porosimetry (MIP). For the thermogravimetry tests, pastes with neither fibres nor sand were made. The plate manufacturing process was carried out on mixing the raw materials following the next procedure:

1. 60 s of mixing water + 2/3 superplasticizer + cement + fly ash
2. 30 s of adding sand and mixing
3. 30 s adding 1/3 superplasticizer
4. 60 s mixing mortar
5. 60 s adding fibre and mixing

The mechanical and the non-destructive tests were performed 90 days after the plates were manufactured, in order to allow the completion of any hydration and pozzolanic reactions in the matrix. All the specimens were cured in a wet chamber at 20 °C and 100 % HR.

Table 2.1.2 gives details of the cement and fly ash chemical composition. As can be observed, the fly ash contains a large amount of SiO_2 and Al_2O_3 (the sum of these oxides was higher than 75%), important components for the progress of a pozzolanic reaction.

2.1.2.2 Test methodology

Several tests were done on this study in order to compare the performance of ultrasonic tests and other characterization techniques. Mechanical tests (INSTRON universal testing machine, model 3382), Scanning Electron Microscopy (JEOL JSM 6300 aplying a 20 kV voltage), Mercury Instrusion Porosimetry (AutoPore IV 9500 of Micrometrics Instrument Corporation with a range of pressures between 13,782 Pa and 227.4 MPa) and Thermogravimetry (Mettler TGA 850).

Description of the Ultrasonic test equipment

An ultrasonic through-transmission setup was selected because it offers good penetration and good accuracy for velocity and attenuation estimation [15, 23–25]. The disposition of the equipment is shown in Figure 2.1.1. The transducers used were the $K1SM$ (for transmission) and $K1SC$ (for reception) from General Electric. Both are broadband transducers with a bandwidth centered at 1 MHz and a circular active surface of $\varnothing$28 mm. Due to the cross section of the specimens (50 × 20 mm^2), part of the active surface of the transducers ($\approx$18%) keeps out of the samples. This fact will produce an identical reduction of the injected and received energy effectiveness for all measures.

Table 2.1.2: Cement and fly ash composition by % weight.

Component	LOI[*]	SiO_2	Al_2O_3	Fe_2O_3	CaO	MgO	SO_3	K_2O	C_4AF	C_3A	C_3S	C_2S
CEM I-52,5 R	2.05	20.52	3.37	3.92	63.36	1.96	2.59	0.99	11.93	2.33	55.7	16.94
Fly ash type F	1.97	49.91	25.80	13.94	3.84	1.06	1.00	2.47	-	-	-	-

[*] Loss on ignition

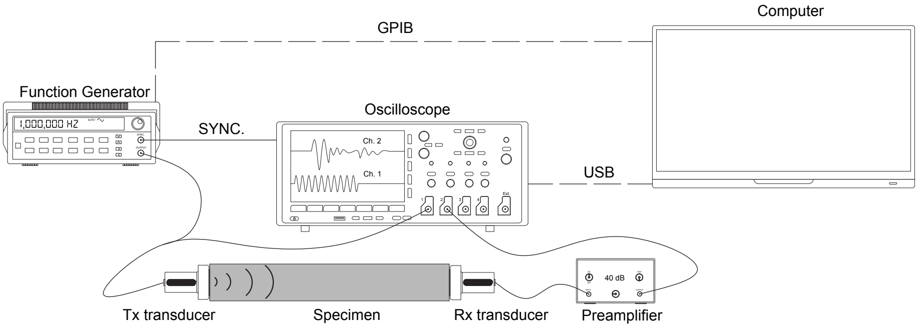

Figure 2.1.1: Ultrasonic equipment layout.

The transmitter transducer was excited directly by a programmable signal generator (Agilent 33120*A*) while the reception transducer was connected to a 40 dB preamplifier (Panametrics 5600*B*). The received and amplified ultrasonic signal was captured by a digital oscilloscope (Tektronix $DPO3014$) with a sampling frequency of 25 MHz. Finally, a laptop was used to control the signal generator and to acquire and store the digitized signals by the oscilloscope.

The ultrasonic transducers were placed facing the longitudinal axis of the specimen as shown in Figure 2.1.2. They were fixed by two plastic clamps: a movable one to adjust to the specimen, and a fixed one. Ultrasonic gel was used as an impedance coupling medium between the transducers and the specimen.

The emitter transducer was excited by means a sinusoidal tone burst generated by the signal generator (see Fig. 2.1.3). From this signal, different ultrasonic parameters can be estimated. As is explained in Section Appendix: Burst Signal, the main set-up parameters of the tone burst signal are: fundamental frequency f_0, amplitude of the signal A_0, the number N of periods included in the burst, and the repetition period T_{PRF}.

The transmitted signal propagates through the specimen and is altered by its physical and mechanical properties and also by the measurement equipment. Comparing the transmitted and the received signals (see Fig. 2.1.3) allows of assessing the ultrasonic propagation parameters. Taking into account that most of the tone burst energy is concentrated around its fundamental frequency (see Appendix: Burst Signal), it is possible to obtain ultrasonic curves doing a frequency sweep of the tone burst f_0.

The selected values for the transmitted signal were: $A_0 = 10$ V, $N = 5$, and $T_{PRF} = 20$ ms. The signal generator was set to sweep the fundamental frequency of the tone burst, f_0, from 1 kHz up to 1 MHz with increments of 5 kHz and a delay of 1 s between each analysed frequency. Therefore, for each specimen, 200 measurements were acquired (one for each fundamental frequency) and a frequency

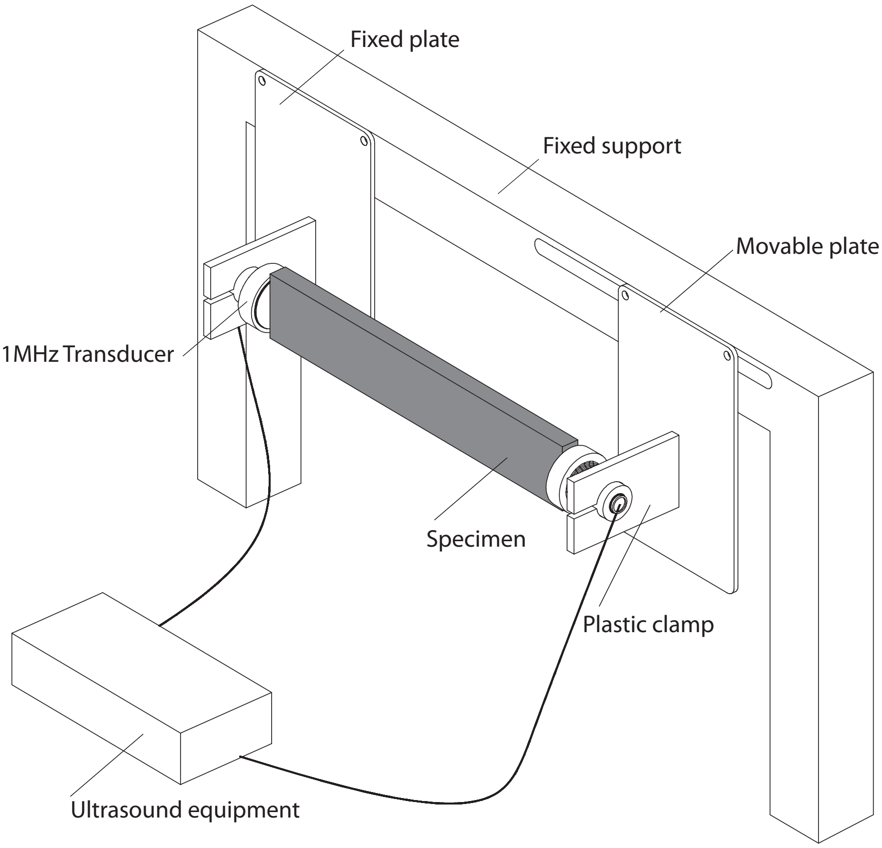

Figure 2.1.2: Test disposition: Specimen and ultrasonic transducers.

response of 200 points is obtained for each ultrasonic parameter. Specifically, the P-wave velocity (v_p [m/s]) and attenuation (α_{mat} [dB/cm]) were the ultrasonic parameters for this analysis [15, 26].

v_p is obtained as the ratio between the length of the specimen, d_{mat}, and the signal time arrival, t_a (Eq. 2.1.1). The t_a was estimated as the time when the received signal ($x_{f_0}^{(rx)}(t)$) level exceeds 20% of the noise level ($p = 1.2$)(Eq. 2.1.2). The noise level, $Noise_{level}$, was estimated as the mean value of the absolute signal at first $t_d = 20\,\mu$s (Eq. 2.1.3).

$$v_p(f_0) = \frac{d_{mat}}{t_a} \tag{2.1.1}$$

$$|x_{f_0}^{(rx)}(t_a)| > p \cdot Noise_{level} \tag{2.1.2}$$

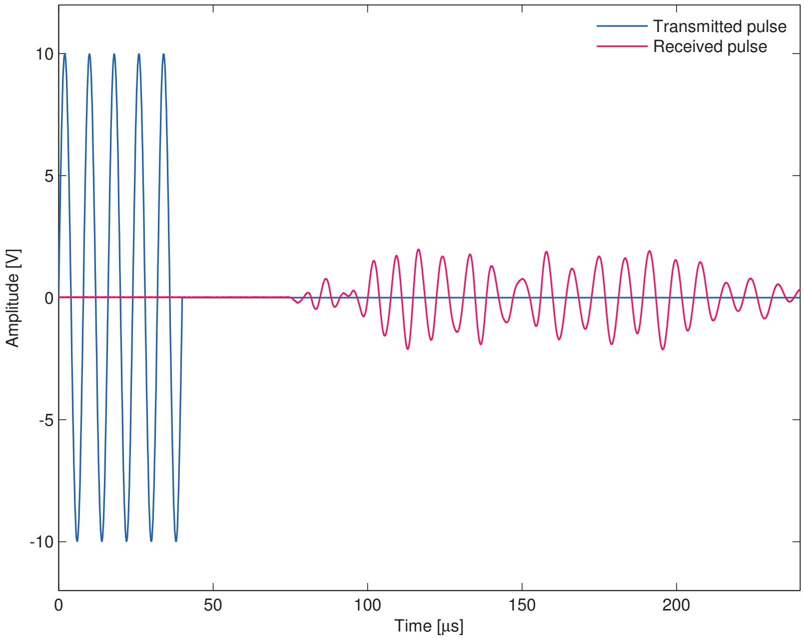

Figure 2.1.3: Transmitted and received tone burst.

$$Noise_{level} = \frac{1}{t_d}\int_0^{t_d} |x_{f_0}^{(rx)}(t)|dt \tag{2.1.3}$$

Additionally, the attenuation of the material, $\alpha_{mat}(f_0)$ [dB/cm], was obtained as the difference between the transmitted energy, $E_{tx}(f_0)$ [dB] and the received energy, $E_{rx}(f_0)$ [dB], plus the attenuation due to the equipment, $\alpha_{equip}(f_0)$ [dB], divided by the total length of the specimen, d_{mat} [cm] (Eq. 2.1.4). $E_{tx}(f_0)$ is obtained theoretically from Eq. 2.1.11, meanwhile $E_{rx}(f_0)$ was obtained from the received signal in the frequency domain from Eq. 2.1.10. The $\alpha_{equip}(f_0)$ is associated to the frequency response of the measurement equipment (transducers, amplifier, cables, acquisition module, ...) and is independent of the tested material. Therefore a calibration process is required.

$$\alpha_{mat}(f_0) = \frac{E_{tx}(f_0) - E_{rx}(f_0) - \alpha_{equip}(f_0)}{d_{mat}} \tag{2.1.4}$$

The calibration process was carried out with the emitter and receiver transducers face to face without any material between them. In this situation, Eq. 2.1.4 simplifies to Eq. 2.1.5 due to the absence of the material. The testing process was similar to the material analysis except that the input signal was reduced up to $0.5V_p$ to avoid saturation.

$$\alpha_{equip}(f_0) = E_{tx}(f_0) - E_{rx}(f_0) \tag{2.1.5}$$

Figure 2.1.4 shows the $-\alpha_{equip}(f_0)$ which was obtained from the calibration process. This curve was used to compensate the received energy during the normal measurement process.

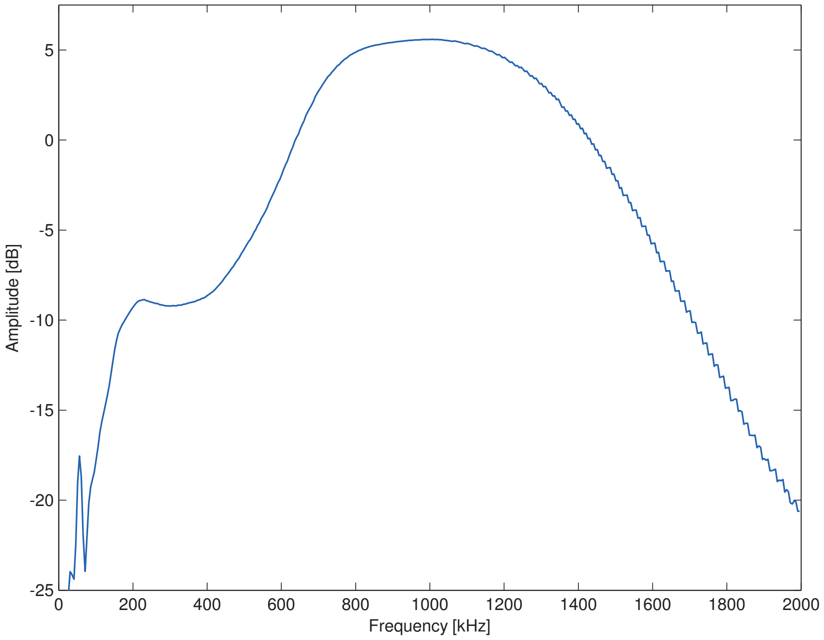

Figure 2.1.4: Frequency response of the measurement module ($-\alpha_{equip}(f_0)$) during the calibration process.

2.1.3 Results and discussion

2.1.3.1 Mechanical results

The specimens used for the compression test were 40 × 40 × 160 mm^3, in accordance with the UNE-EN-1015-11 standard, and were manufactured without fibres in order to obtain the compressive strength of the matrix and extract some fragments to analyse by means of Mercury Intrusion Porosimetry (MIP). The specimens used for the four-point flexural test were 325 × 50 × 20 mm^3, in accordance with BS EN 1170-5.

Table 2.1.3: Parameters obtained from mechanical tests.

Serie	σ_{comp} [Mpa]	σ_{flex} [Mpa]	Ec [GPa]	Work of fracture [Nmm]
fa - 030	92.2±2.2	10.9±1.2	20±2	882±174
fa - 035	86.1±4.1	14.0±0.6	19±2	1926±232

The specimens used for the bending test were extracted from a 400 × 400 × 20 mm^3 mother plate and used to obtain the work of fracture [Nmm], the maximum flexural strength σ_{flex} [MPa], and the elastic modulus Ec_{flex} [GPa]. The mechanical data are summarized in Table 2.1.3.

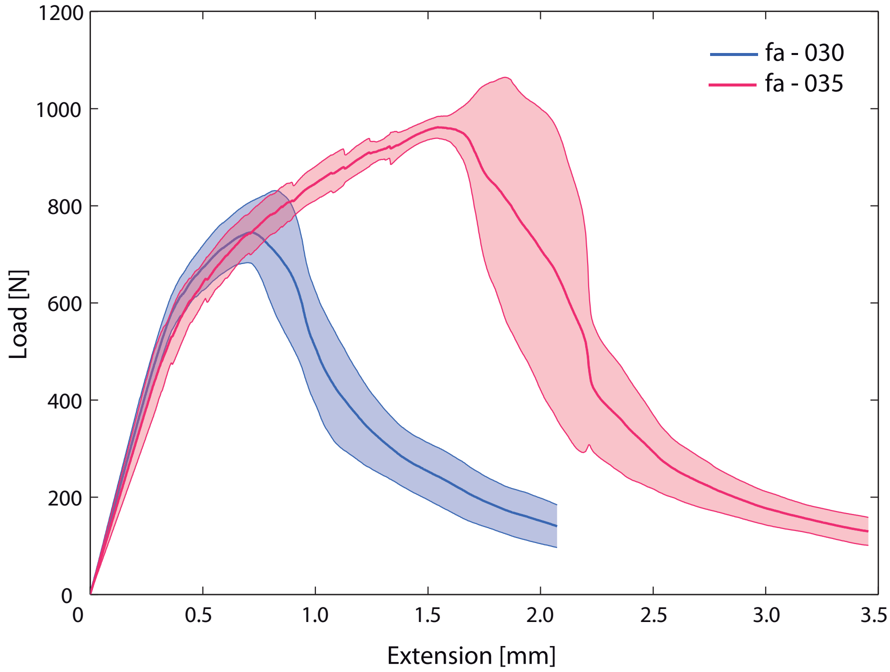

Figure 2.1.5: Load versus extension curves for both series. Mean value of the parameters is represented by a coarse line. The shaded area represent the 90% confidence interval.

The mechanical results obtained show that the series possess different properties. The compressive strength of the fa-030 was higher than that of fa-035: lower w/b ratios make the material more compact and better for compressive stress. The flexural strength of fa-035 was higher, because the specimen suffers high tensile stress on the lower fibre of the element and the glass fibre begins to work. For this type of composite, the reduction of the w/b ratio produces a more rigid matrix, yielding a more brittle fracture. Additionally, the fibres better distribute the tensile stresses into a more ductile matrix. The work of fracture calculated from the curves shown in Figure 2.1.5 have the best behaviour in toughness for the fa-035 series.

2.1.3.2 Thermogravimetry results

After mixing the raw components of the pastes, the samples were kept in closed containers at 20 °C. After 28 and 90 days of curing, portions of the samples were taken and pulverized with an agate mortar adding a small amount of acetone. The solid was filtered and dried at 60 °C for 15 minutes. These samples were studied by means of a thermogravimetric analysis. Sealed aluminium crucibles of 100 μm were used with a lid that with a micro hole to create a water vapour self-generated atmosphere. The analysis was carried out in a dry nitrogen atmosphere with a flow of 75 mL/min, a heating rate of 10 °C/min, and a temperature range of 35 °C to 600 °C. A thermogravimetric test was performed on the samples to check the progression of a pozzolanic reaction between $Ca(OH)_2$ (portlandite) produced from the hydration of the Portland cement and fly ash. As mentioned before, the pozzolanic reaction is important in reducing the pH of the matrix and its $Ca(OH)_2$ consumption, enhancing the chemical stability of the glass fibre.

Table 2.1.4: Thermogravimetric parameters for 90-day cured pastes.

Series	Total loss [%]	$Ca(OH)_2$ [%]	Hydrates [%]	Comb. $Ca(OH)_2$ [%]	% $Ca(OH)_2$*
control	18.36	9.41	16.07	-	100
fa - 030	12.68	1.44	12.33	65.82	15.28
fa - 035	15.75	1.89	15.29	55.08	20.08

* Respect to the control

Figure 2.1.6 shows the results of the thermogravimetric analysis (derivative curves, DTG) for fa-035 and the control material manufactured without fly ash and the same w/b ratio. The DTG curve for fa-030 was very similar to that for fa-035, and it is not plotted, for the sake of clarity. The control sample was necessary for calculating the percentage of the portlandite fixation. The portlandite fixation parameters are shown in Table 2.1.4. As can be observed, both series (fa-030 and fa-035) have high percentages (55%–65%) of combined $Ca(OH)_2$, indicating an important pozzolanic activity on the fly ash. The matrices containing fly ash have only 15%–20% of $Ca(OH)_2$ in comparison to the control, and consequently, the chemical stability of the fibres is enhanced.

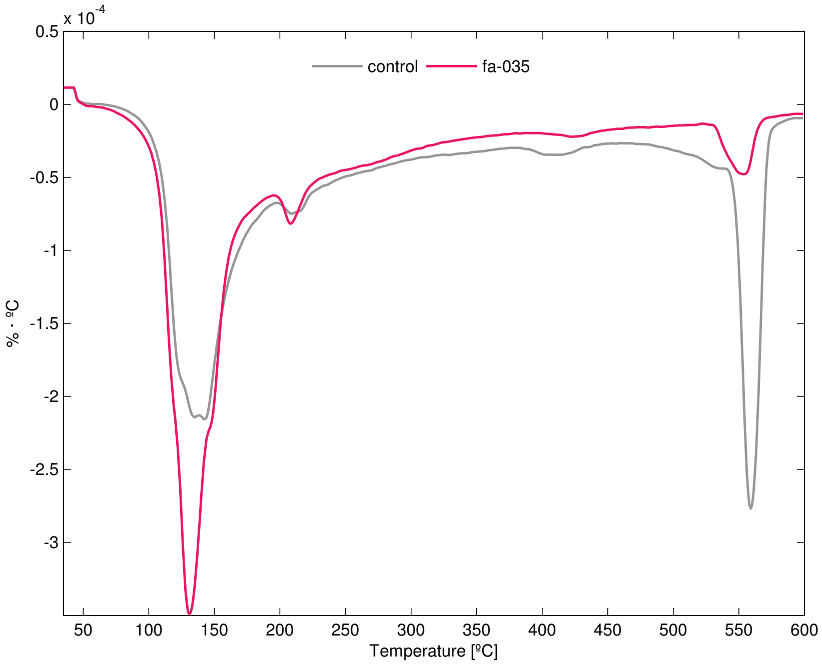

Figure 2.1.6: Thermogravimetric analysis of matrix samples and cement control.

2.1.3.3 Mercury Intrusion Porosimetry (MIP)

Due to the relevance of the capillary net, pores, and density, Mercury Intrusion Porosimetries were performed on both series to allow comparison with ultrasonic parameters.

In Figure 2.1.7, the fa-030 and fa-035 pore distribution curves are shown. fa-035 shows a more porous structure than fa-030. This behaviour is due to the fact that fa-035 has a higher water to binder ratio than fa-030. In addition, fa-030 has slightly different pore sizes than fa-035: the fa-030 curve shifts to smaller pore sizes in comparison to the fa-035 curve.

The MIP data are summarized in Table 2.1.5. The mortar prepared with the highest w/b ratio (fa-035) showed the highest total porosity and the lowest bulk density, since more water remained chemically uncombined as hydra-

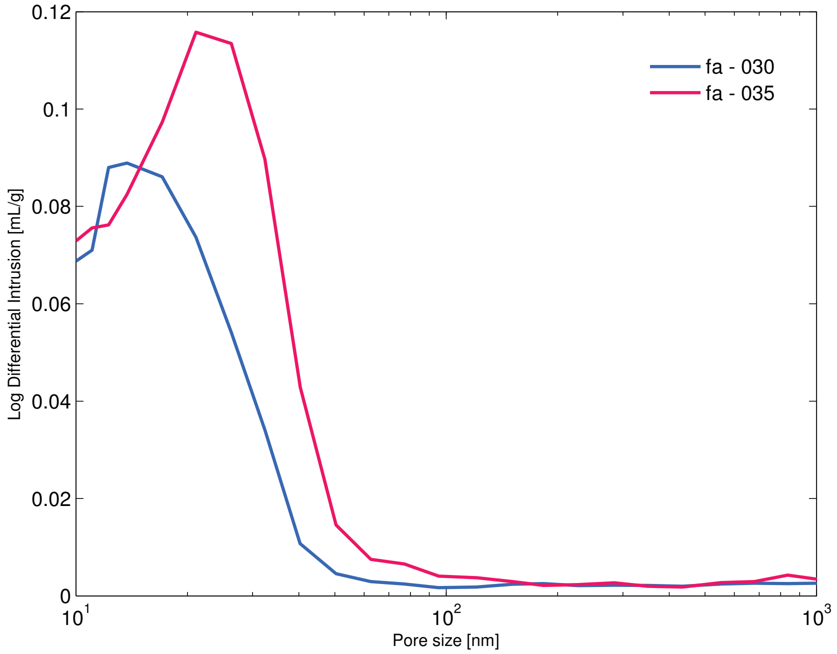

Figure 2.1.7: Pore distribution curves of both series tested without fibres.

Table 2.1.5: MIP obtained parameters.

Serie	Total porosity [%]	Bulk density [g/mL]	Median pore diameter [nm]
fa - 030	15.07	1.96	18.3
fa - 035	18.29	1.89	22.2

tion/pozzolanic products. These results, as will be seen in Section 2.1.3.5, correlate with the ultrasonic characterization and also with the mechanical test data.

2.1.3.4 Scanning Electron Microscopy (SEM) observations

Visual observations were performed with SEM on the GRC specimens to verify that pozzolanic products were formed and the glass fibres were embedded properly into the matrix.

In Figure 2.1.8a, it can be observed that the fibres were perfectly surrounded by the matrix and several hydration and pozzolanic products were also found. Figure 2.1.8b shows a more detailed view of the fibres with unreacted fly ash

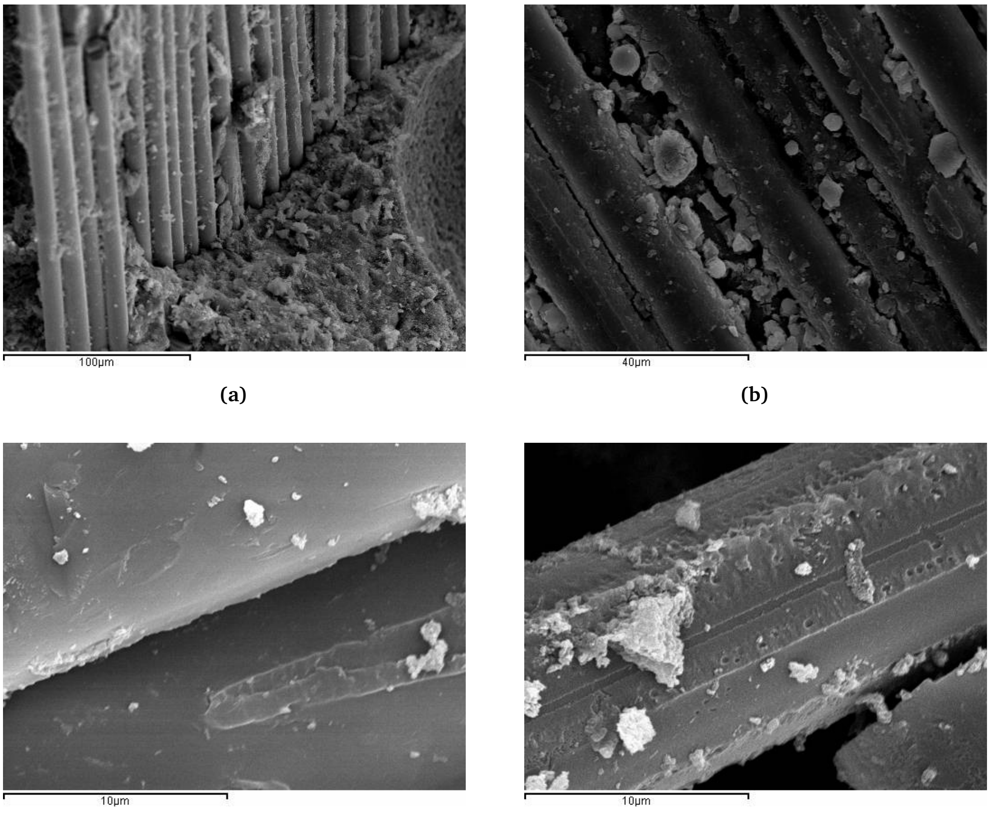

(a) (b)

(c) (d)

Figure 2.1.8: SEM observations with different magnification of the GRC specimens. Figure 2.1.8a ×500 magnification glass fibre embedded on matrix. Figure 2.1.8b ×1500 magnification glass fibre with unreacted fly ash spheres. Figure 2.1.8c ×6000 magnification glass fibre surface detail. Figure 2.1.8d ×6000 magnification glass fibre surface detail.

on top of the fibres. A pozzolanic reaction had a successful progression, as was observed previously on thermal analysis, but a small amount of these particles did not react. Both images correspond to the fa-035 specimen because there was no substantial difference between the fa-035 and fa-030 in the SEM, as expected. In Figs 2.1.8c and 2.1.8d, detailed views of the glass fibre surfaces can be seen. Is important to highlight that the fibres are not attacked by the matrix.

2.1.3.5 Ultrasonics results

The velocity, $v_p(f_0)$, and attenuation, $\alpha_{mat}(f_0)$, responses of the specimens are shown in Figure 2.1.9 and Figure 2.1.10 respectively.

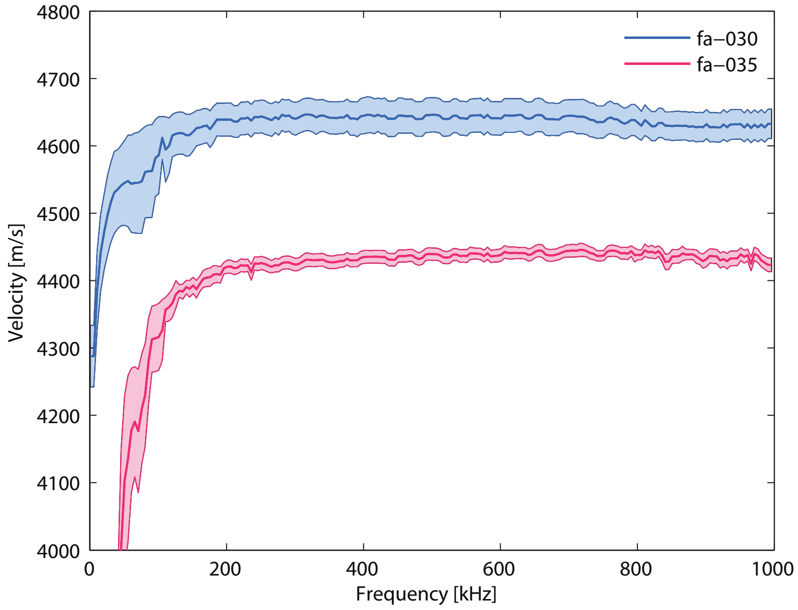

Figure 2.1.9: Velocity response versus frequency. Mean value of the parameters is represented by a coarse line. The shaded area represent the 90% confidence interval.

From Figure 2.1.9, the velocity can be assumed to be constant over a large frequency range [15]. The velocity dependence at low frequencies (0–200 Hz) is due to surface waves generated for these frequencies, which are slower than P-waves, and due to the velocity estimation algorithm, which detects, by the increase of the signal level over a threshold, the arrival time of the signal, t_a. Due to the fact that the slope of the signal is smaller for low frequencies, the increment of the level signal is also slower. Therefore the detected arrival time is later than the real one and the velocity measurements are lower than expected. Over 200 kHz, this effect can be neglected and a precise estimation of velocity is obtained. Taking into account this fact, we can assume that the primary velocity response is mainly flat for both specimens although a systematic difference exists between them. For fa-030, the mean velocity is $v_p = 4639 \pm 29$ m/s while for fa-035, it is 200 m/s lower ($v_p = 4435 \pm 19$ m/s). This result is consistent with the mechanical analysis which offers a higher compressive strength for fa-030. It also indicates that fa-030 yields a higher modulus of elasticity than fa-035, E_c, which is also consistent with the calculated E_c from the stress–strain curve, 20 GPa for fa-030 and 19 GPa for fa-035.

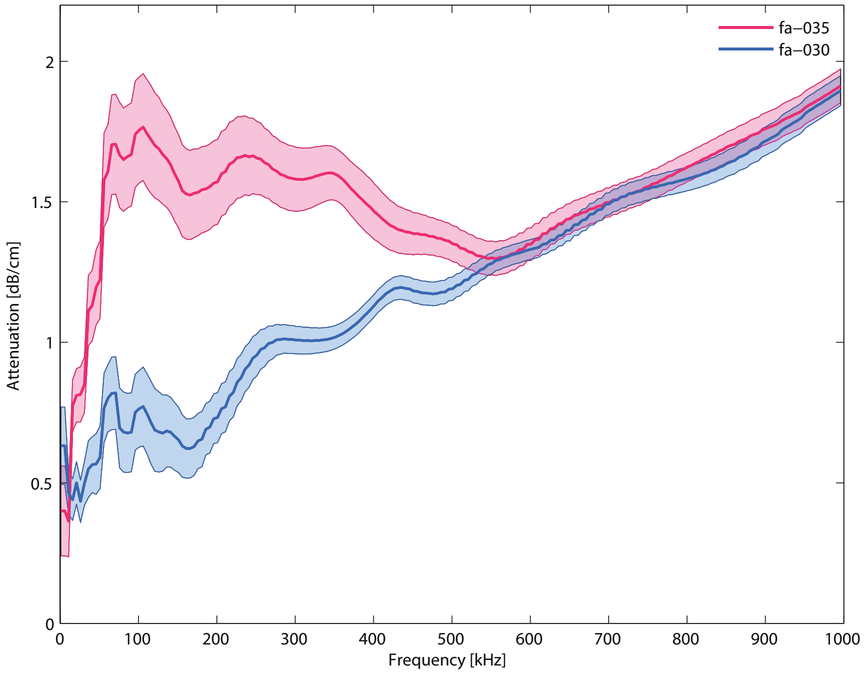

Figure 2.1.10: Attenuation response versus frequency. Mean value of the parameters is represented by a coarse line. The shaded area represent the 90% confidence interval.

The attenuation response for both specimens (Fig. 2.1.10) shows that fa-035 specimens present a generally higher attenuation than fa-030 specimens. Taking into account that both of them have a very similar matrix, this different behaviour can be attributed to the differences in the porosity of the specimens. The average pore size of fa-035 is greater than the average pore size of fa-030, as is shown in Table 2.1.5. Therefore the attenuation for the Rayleigh and stochastic zones (< 550 kHz) is higher for fa-035, as shown in Figure 2.1.10. For frequencies over 550 kHz (the diffusion region, [15, 24]), both specimens converge with a similar linear positive dependence.

2.1.4 Conclusions

Two glass-fibre reinforced cementitious materials (GRC) with different porosity and mechanical properties were evaluated using different techniques. It has been demonstrated that ultrasonic tests allow distinguishing between both materials and provide additional information on the material behaviour and mechanical parameters. The attenuation curves could be used to establish a relationship between the porosity parameters and some mechanical properties extracted from a four-point bending test. The P-wave velocity was also stable and indicated a strong relationship with the elastic modulus.

Acknowledgments

This work has been supported by the Government of Spain under grant TEC2011-23403 01/01/2012.

Appendix: Burst Signal

The mathematical model of a tone burst signal is shown in Eq. 2.1.6, where a sinusoidal signal, $A_0 \sin(2\pi f_0 t)$ is active for a specific period of time (NT_0). This is repeated periodically, obtaining Eq. 2.1.7. The main parameters of this signal are: T_0 is the period of the fundamental frequency ($f_0 = 1/T_0$), A_0 is the amplitude of the signal, N is the number of periods included in the burst, and T_{PRF} is the repetition period. Figure 2.1.11a shows an example of a tone burst signal.

$$x(t) = \begin{cases} A_0 \sin(2\pi f_0 t) \ , 0 < t < NT_0 \\ 0 \ , \text{otherwise} \end{cases} \tag{2.1.6}$$

$$x_{periodic}(t) = \sum_{k=-\infty}^{\infty} x(t - kT_{PRF}) \tag{2.1.7}$$

The real model used for the experiments corresponds to Eq. 2.1.7 because the burst signal is repeated periodically and the signal should have finite non-zero power. Despite this, the oscilloscope captures just a few microseconds, $t_{capture}$, and the signal is cut off and limited in time. As a result of this, the acquired signal is of finite time duration and has finite energy. Therefore, Eq. 2.1.6 will be the expression for theoretical analysis and T_{PRF} will not influence the operations, provided it will be bigger than the capture time of the oscilloscope. This last condition is satisfied in this analysis because $T_{PRF} = 20$ ms and $t_{capture} = 100\,\mu$s.

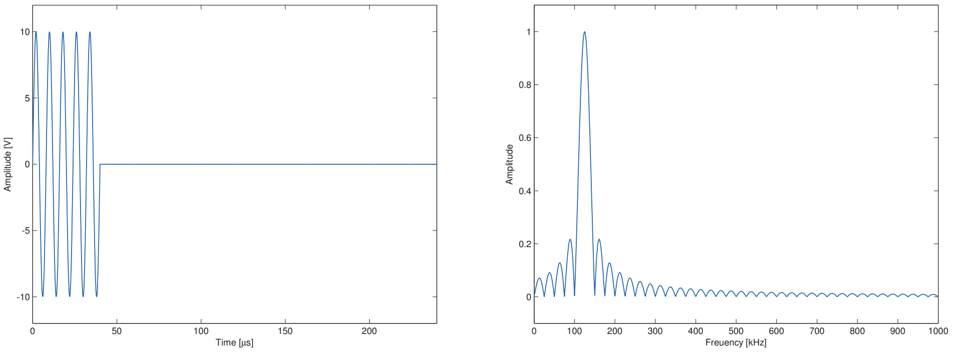

(a) **(b)**

Figure 2.1.11: Figure 2.1.11a Tone burst signal: $f_0 = 125$ kHz, $A_0 = 10$, $N = 5$. Figure 2.1.11b Normalized magnitude spectrum of tone burst signal ($f_0 = 125$ kHz, $N = 5$).

The theoretical energy of a burst signal is given by Eq. 2.1.8. It is important to take into account the following facts: first, the transmitted energy depends on its fundamental frequency, f_0. Second, the energy is not completely concentrated on its fundamental frequency, f_0, but is distributed over a bandwidth. If the Fourier transform is applied to Eq. 2.1.6, we obtain the spectrum of the burst signal, Eq. 2.1.9, for positive frequencies. The absolute value of $X(f)$ is represented in Figure 2.1.11b. For these reasons, the energy of the transmitted and received signals will be calculated from the spectrum over a bandwidth following Eq. 2.1.10 [27]. The bandwidth has been chosen to correspond to the main lobe of the spectrum, $f_0 \pm \frac{f_0}{N}$. If the theoretical expression of the spectrum, Eq. 2.1.9, is used in Eq. 2.1.10, a theoretical expression for the transmitted energy is obtained, Eq. 2.1.11. This expression also depends on f_0. The ratio between the bandwidth energy, Eq. 2.1.11, and the total energy, Eq. 2.1.8, is a constant ratio of 0.9, which means that 90% of the energy is concentrated within the main lobe.

$$E_{tx}(f_0)\ [J] = A_0^2 N \frac{1}{2f_0} \tag{2.1.8}$$

$$X(f) = \frac{A_0 N T_0}{2} sinc\left((f - f_0) N T_0\right) e^{-j(2\pi f - 2\pi f_0)\frac{NT_0}{2}} \tag{2.1.9}$$

$$E[J] = 2\int_{<BW>} |X(f)|^2 df = 2\int_{f_0-\frac{f_0}{N}}^{f_0+\frac{f_0}{N}} |X(f)|^2 df \tag{2.1.10}$$

$$E_{tx,BW}(f_0)\ [J] = A_0^2 N \frac{1}{f_0} \frac{Si(2\pi)}{\pi} \tag{2.1.11}$$

References

[1] A. J. Majumdar, J. Ryder, and B. R. Station, *Glass fibre reinforcement of cement products*. Garston, England: Building Research Station, 1968.

[2] A. Bentur, *Fibre reinforced cementitious composites*. Taylor & Francis, 1990.

[3] A. J. Majumdar, J. M. West, and L. J. Larner, "Properties of glass fibres in cement environment," *Journal of Materials Science*, vol. 12, no. 5, pp. 927–936, 1977.

[4] L. J. Larner, K. Speakman, and A. J. Majumdar, "Chemical interactions between glass fibres and cement," *Journal of Non-Crystalline Solids*, vol. 20, no. 1, pp. 43–74, 1976.

[5] P. C. Ma, J. W. Liu, S. L. Gao, and E. Mäder, "Development of functional glass fibres with nanocomposite coating: A comparative study," *Composites Part A: Applied Science and Manufacturing*, vol. 44, pp. 16–22, 2013.

[6] S. L. Gao, E. Mäder, and R. Plonka, “Nanocomposite coatings for healing surface defects of glass fibers and improving interfacial adhesion,” *Composites Science and Technology*, vol. 68, no. 14, pp. 2892–2901, 2008.

[7] P. Purnell, N. R. Short, C. L. Page, A. J. Majumdar, and P. L. Walton, “Accelerated ageing characteristics of glass-fibre reinforced cement made with new cementitious matrices,” *Composites Part A: Applied Science and Manufacturing*, vol. 30, no. 9, pp. 1073–1080, 1999.

[8] S. Leonard and A. Bentur, “Improvement of the durability of glass fiber reinforced cement using blended cement matrix,” *Cement and Concrete Research*, vol. 14, no. 5, pp. 717–728, 1984.

[9] B. A. Proctor, D. R. Oakley, and K. L. Litherland, “Developments in the assessment and performance of GRC over 10 years,” *Composites*, vol. 13, no. 2, pp. 173–179, 1982.

[10] J. Payá, M. Bonilla, M. V. Borrachero, J. Monzó, E. Peris, and L. F. Lalinde, “Reusing fly ash in glass fibre reinforced cement: A new generation of high-quality GRC composites,” *Waste Management*, vol. 27, no. 10, pp. 1416–1421, 2007.

[11] W. T. Lin, A. Cheng, R. Huang, and S. Y. Zou, “Improved microstructure of cement-based composites through the addition of rock wool particles,” *Materials Characterization*, vol. 84, pp. 1–9, 2013.

[12] V. M. Maholtra and N. J. Carino, Eds., *Handbook on Non destructive Testing on Concrete*. CRC Press, 2004, vol. 1.

[13] J. A. Bogas, M. G. Gomes, and A. Gomes, “Compressive strength evaluation of structural lightweight concrete by non-destructive ultrasonic pulse velocity method,” *Ultrasonics*, vol. 53, no. 5, pp. 962–972, 2013.

[14] A. Jain, A. Kathuria, A. Kumar, Y. Verma, and K. Murari, “Combined use of non-destructive tests for assessment of strength of concrete in structure,” *Procedia Engineering*, vol. 54, pp. 241–251, 2013.

[15] T. P. Philippidis and D. G. Aggelis, “Experimental study of wave dispersion and attenuation in concrete,” *Ultrasonics*, vol. 43, no. 7, pp. 584–595, 2005.

[16] S. Popovics, J. L. Rose, and J. S. Popovics, “The behaviour of ultrasonic pulses in concrete,” *Cement and Concrete Research*, vol. 20, no. 2, pp. 259–270, 1990.

[17] L. Vergara, J. Gosálbez, J. V. Fuente, R. Miralles, and I. Bosch, “Measurement of cement porosity by centroid frequency profiles of ultrasonic grain noise,” *Signal Processing*, vol. 84, no. 12, pp. 2315–2324, 2004.

[18] L. Vergara, R. Miralles, J. Gosálbez, F. J. Juanes, L. G. Ullate, J. J. Anaya, M. G. Hernández, and M. A. G. Izquierdo, "NDE ultrasonic methods to characterise the porosity of mortar," *NDT & E International*, vol. 34, no. 8, pp. 557–562, 2001.

[19] D. G. Aggelis and T. P. Philippidis, "Ultrasonic wave dispersion and attenuation in fresh mortar," *NDT & E International*, vol. 37, no. 8, pp. 617–631, 2004.

[20] Z. Lafhaj, M. Goueygou, A. Djerbi, and M. Kaczmarek, "Correlation between porosity, permeability and ultrasonic parameters of mortar with variable water/cement ratio and water content," *Cement and Concrete Research*, vol. 36, no. 4, pp. 625–633, 2006.

[21] J. N. Eiras, T. Kundu, M. Bonilla, and J. Payá, "Nondestructive monitoring of ageing of alkali resistant glass fiber reinforced cement (GRC)," *Journal of Nondestructive Evaluation*, vol. 32, no. 3, pp. 300–314, 2013.

[22] B. Standard, *Precast concrete products - Test method for glass-fibre reinforced cement - Part 5. Measuring bending strength, 'Complete bending test' method.* 1998.

[23] J. Krautkrämer and H. Krautkrämer, *Ultrasonic testing of materials*. Springer-Verlag, 1983.

[24] P. A. Gaydecki and F. M. Burdekin, "The propagation and attenuation of medium-frequency ultrasonic waves in concrete: a signal analytical approach," *Measurement Science and Technology*, vol. 3, p. 126, 1992.

[25] M. Molero, I. Segura, S. Aparicio, M. G. Hernández, and M. A. G. Izquierdo, "On the measurement of frequency-dependent ultrasonic attenuation in strongly heterogeneous materials," *Ultrasonics*, vol. 50, no. 8, pp. 824–828, 2010.

[26] L. Vergara, J. V. Fuente, J. Gosálbez, R. Miralles, and I. Bosch, "Processing of ultrasonic grain noise signals for the estimation of depth-and frequency-dependent attenuation," *Measurement Science and Technology*, vol. 14, no. 7, pp. 1–7, 2003.

[27] S. S. Soliman and M. D. Srinath, *Continuous and Discrete Signals and Systems*. Prentice-Hall International, 1998.

2.2 Ultrasonic monitoring on glass-fiber reinforced cement (GRC) bending test[2]

[2] V. Genovés, J. Gosálbez, R. Miralles, L. Soriano, and J. Payá. "Ultrasonic monitoring on glass-fiber reinforced cement (GRC) bending test," Materials Characterisation VII. vol. 90. WIT Transactions on Engineering Sciences, 2015, pp. 149–158.

Abstract

Glass-fiber reinforced cement (GRC) is a composite material based on Portland cement and alkali resistant glass-fibers. This composite has good mechanical properties including toughness and flexural strength. The characterization of this material is carried out by four points bending test. During this test, elastic and plastic behaviour are identified from load versus deflection curves. The scope of the research is to monitor this bending test by means on ultrasonic pulses in order to detect changes on the material and to correlate them with mechanical behaviour. In this sense, pulse velocity, energy, attenuation and non-linearities of the ultrasonic received signals have been analysed. First changes in energy, attenuation and non-linearities were detected during the change from elastic to plastic step and the first pulse velocity change were observed during the plastic step.

2.2.1 Introduction

Glass-fiber Reinforced Cement (GRC) is a composite made of Portland cement mortar with low water/cement (w/c) ratio with a large amount of paste in relation to the aggregate quantity. The addition of a high proportion of glass-fibers to the mortar matrix (3%-5% by weight of mortar) improves the mechanical properties of the elements produced with this material reinforcement, especially the toughness, flexural strength and ductility. This composite has an important role in non-steel reinforced pre-cast concrete elements, such as sheets, panels and other slim shapes usually employed in building engineering and architecture, and also in cast-in-situ sprayed-on surfaces [1, 2].

Recently, several researchers have focused on non-destructive concrete and mortar characterization in order to obtain more reliable information and new aspects of cementitious composites without damaging the specimen under test. During recent years, Non-Destructive Techniques (NDT) applied on concrete have been investigated, especially ultrasonics and acoustic spectroscopy, in order to obtain parameters related to the physical and mechanical properties of the material [3]. Some experimental studies have demonstrated that wave parameters such as the ultrasonic pulse velocity of P-waves are suitable to predict the dynamic elastic modulus of concrete and also S-waves for dynamic shear modulus. These parameters are proportional to the elastic and shear moduli of concrete and also to its compressive strength [4, 5]. Other studies based on ultrasound propagation indicate that wave attenuation can be measured for various frequencies, in order to define different cementitious materials, distinguishing the microstructure, porosity, and other characteristics in both hardened [6–9] and fresh states [10]. Some studies have shown interesting correlations between other properties of cementitious composites, such as their permeability or porosity, using ultrasonic parameters such as pulse velocity, signal attenuation, or reflection coefficients, by means of an specific test set-up.

Many studies on construction materials tests monitored by ultrasounds were published by researchers [11]. Research on metallic specimens are predominant because this material is used in other engineering fields. However, recent studies on reinforced concrete slabs bending tests with an ultrasonic monitoring were done successfully [12]. The scope of this paper is to monitor bending tests of GRC specimens in order to assess the changes on most important linear ultrasonic parameters (P-wave velocity, energy and attenuation) and non-linear ultrasonic behaviour.

2.2.2 Experimental

2.2.2.1 Materials

In this experiment the specimen dimension for bending test was chosen as 325 × 50 × 20 mm.

Table 2.2.1: Used dosage for one GRC plate specimen.

Material	Type	Weight [g]
Cement	CEM I 52.5 R	7260
Water	-	2541
Sand	Silica sand 0/2	4864
Superplasticizer	polycarboxylate ether	14
Fiber	Glass AR 12 mm	294

The specimens were cut from 400 × 400 × 20 mm mother plates. From mother plate three specimens were obtained. Table 2.2.1 shows the proportions and information about the raw materials used to fabricate the GRC plate.

2.2.2.2 Experimental layout

An ultrasonic through-transmission setup was selected because it offers good penetration and good accuracy for velocity and attenuation estimation [6, 13–15]. The disposition of the equipment is shown in Figure 2.2.1.

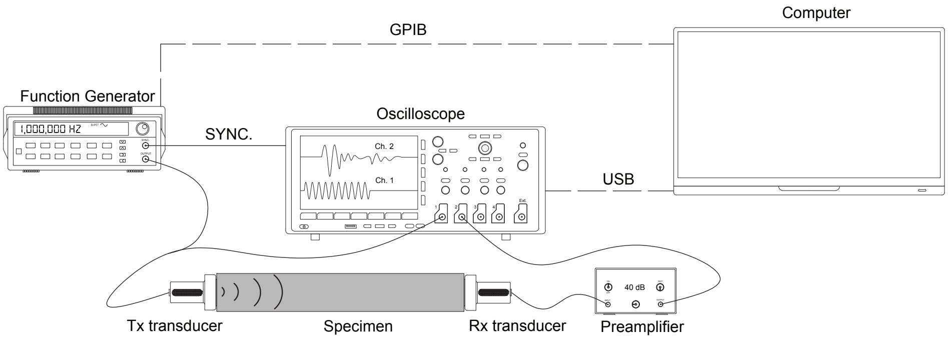

Figure 2.2.1: Ultrasonic equipment layout.

The transducers used were the K1SM (for transmission) and K1SC (for reception) from General Electric. Both are broadband transducers with a bandwidth centered at 1 MHz.

GRC specimens were made according to the BS EN 1170-5 [16]. Instron universal testing machine (model 3382) was used for the mechanical test and the distance for the supports was 295 mm for passive supports and 98 mm for active ones. The displacement of the actuator was constant during the test (1.2 mm/min).

The transmitter transducer was excited directly by a programmable signal generator (Agilent 33120A). The transmitted signal was a sinusoidal burst signal Eq. 2.2.1 and the selected values were: amplitude, $A_{tx} = 10V$, number of cycles, $N = 10$, and fundamental frequency, $f_0 = 300kHz$ (Fig. 2.2.2).

The reception transducer was connected to a 40 dB preamplifier (Panametrics 5600B). The received and amplified ultrasonic signal was captured by a digital oscilloscope (Tektronix DPO3014) with a sampling frequency of 25 MHz. Finally,

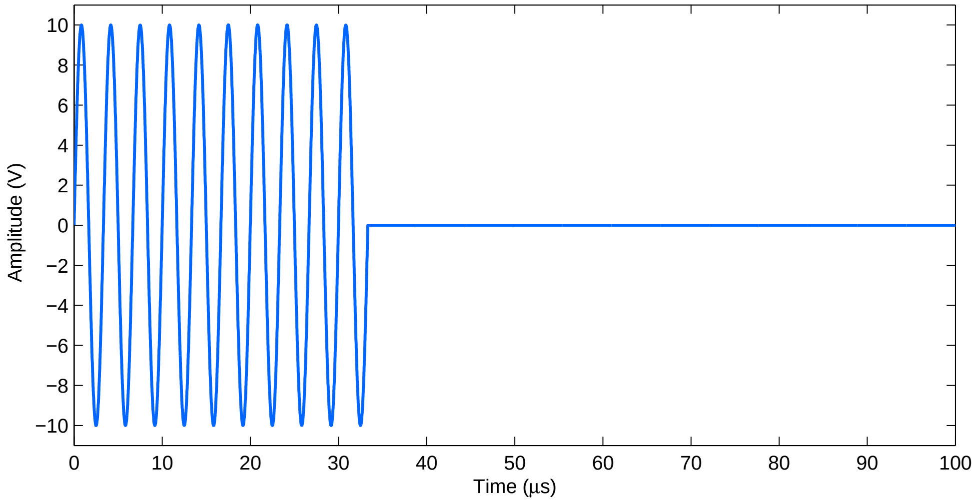

Figure 2.2.2: Tone burst signal: $f_0 = 300kHz$, $A_{tx} = 10$, $N = 10$.

a laptop was used to control the signal generator and to acquire and store the digitized signals by the oscilloscope.

$$x_{tx}(t) = \begin{cases} A_{tx} \sin(2\pi f_0 t) & , \quad 0 < t < NT_0 \\ 0 \quad , \quad \text{otherwise} \end{cases} \tag{2.2.1}$$

In Figure 2.2.3 the experimental layout of simultaneous mechanical test and ultrasonic continuous data acquisition system is shown. The plate rests on the passive supports and four metallic angles were attached to it. These elements serve to hold the elastic bands which keep the pressure of the transducers on the faces of the plate. This system is similar to that other authors used previously, in which rubber bands keep the appropriate coupling between transducers and specimen [17]. To ensure proper coupling between transducer and specimen faces, water-based gel was used.

2.2.2.3 Monitorized ultrasound parameters

The estimated ultrasound parameters from received ultrasonic signal are: p-wave velocity, received energy, attenuation of the material and non-linear behaviour. These parameters will depend on the time of the assay (t).

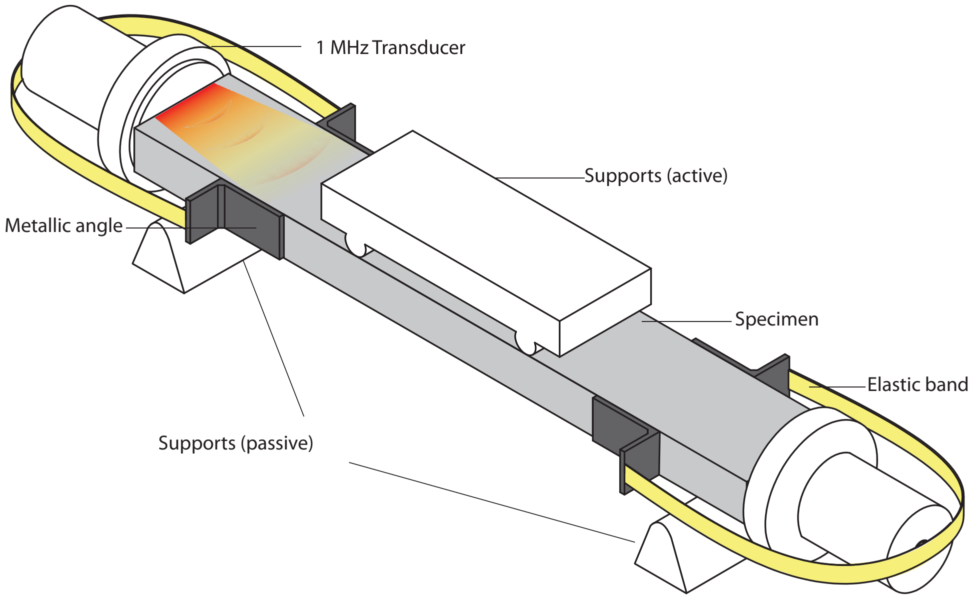

Figure 2.2.3: Experimental layout.

P-wave velocity ($v_p(t)$ [m/s]) is obtained as the ratio between the length of the specimen, d_{mat}, and the signal time arrival, $t_a(t)$, Eq. 2.2.2. The t_a was estimated as the time when the received signal level exceeds 50 % of the noise level.

$$v_p(t) = \frac{d_{mat}}{t_a(t)} \tag{2.2.2}$$

Received energy, $E_{rx}(t)$ [J] is the energy of the received signal measured by the oscilloscope. The $x_{rx,t}$ is the amplitude of the signal at each instant of time τ. Its value is obtained from Eq. 2.2.3.

$$E_{rx}(t)\ [\mathrm{J}] = \int_0^\infty x^2_{rx,t}(\tau)d\tau \tag{2.2.3}$$

Attenuation of the material $\alpha_{mat}(t)$ [dB/cm], is obtained as the difference between transmitted energy, E_{tx} [dB] and the received energy, $E_{rx}(t)$ [dB], plus attenuation due to the equipment, α_{equip} [dB], divided by the total length of the specimen, d_{mat} [cm], Eq. 2.2.4. Taking into account that analytical expression and specific parameters of the transmitted signal are known, Eq. 2.2.5, E_{tx} can be obtained theoretically using Eq. 2.2.5. This value, 1.7 mJ, is constant through the test. Meanwhile $E_{rx}(t)$ is obtained from Eq. 2.2.3. The $\alpha_{equip} = -5$dB is the attenuation associated to the measurement equipment (transducers, amplifier, cables, acquisition module,...) and, it is independent of the tested material and it is constant through the test although a calibration process was required.

$$\alpha_{mat}(t)\ [\text{dB/cm}] = \frac{E_{tx} - E_{rx}(t) - \alpha_{equip}}{d_{mat}} \tag{2.2.4}$$

$$E_{tx}\ [J] = A_{tx}^2 N \frac{1}{2f_0} \tag{2.2.5}$$

$\beta_3(t)$ was selected as non-linear parameter. It is defined as the ratio between the amplitude of the third harmonic (A_3) and the fundamental harmonic (A_1) following Eq. 2.2.6 and it is very sensitive to the formation of cracks. Therefore, the variation of this parameter respect to its initial value will be represented as $\beta_3^{\%}(t)$, according to Eq. 2.2.7, where $\beta_3^{\%}(0)$ is the non-linear parameter before beginning the loading (t=0).

$$\beta_3(t) = \frac{A_3(t)}{A_1^3(t)} \tag{2.2.6}$$

$$\beta_3^{\%}(t) = 100\frac{\beta_3(t)}{\beta_3(0)} \tag{2.2.7}$$

2.2.3 Results and discussion

Mechanical parameters of each plate were obtained from bending tests (Tab. 2.2.2).

Table 2.2.2: Mechanical parameters extracted from bending test.

Specimen	Toughness [Nmm]	Ec$_{flex}$ [GPa]	σ_{max} [MPa]
A	595	18.2	10.3
B	438	17.3	9.5
C	794	23.5	12.9

After completion of the tests, ultrasound parameters and load versus extension curves were plotted on the same figures. The time x-axis was used because the active supports velocity was constant throughout the test as described in the experimental subsection, thus, the understanding of the graphs is improved.

In Figure 2.2.4, P-wave velocity was plotted for each specimen. It can be observed that the wave velocity (v_p) does not change during the elastic material

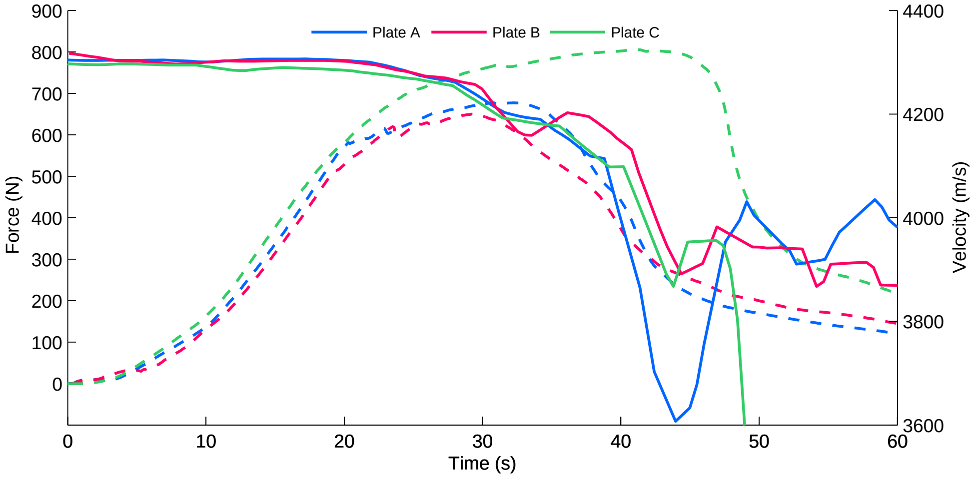

Figure 2.2.4: P-wave velocity and Force versus Time.

behaviour (t=0-25 s). When the material comes in plastic stage (t=25-35s), p-wave velocity changes to lower values due to the micro-cracking process. This microcracking produce a diminution in the Young modulus. When the material was very damaged (t <40s), v_p values shown a non-defined trend because the large size of cracks.

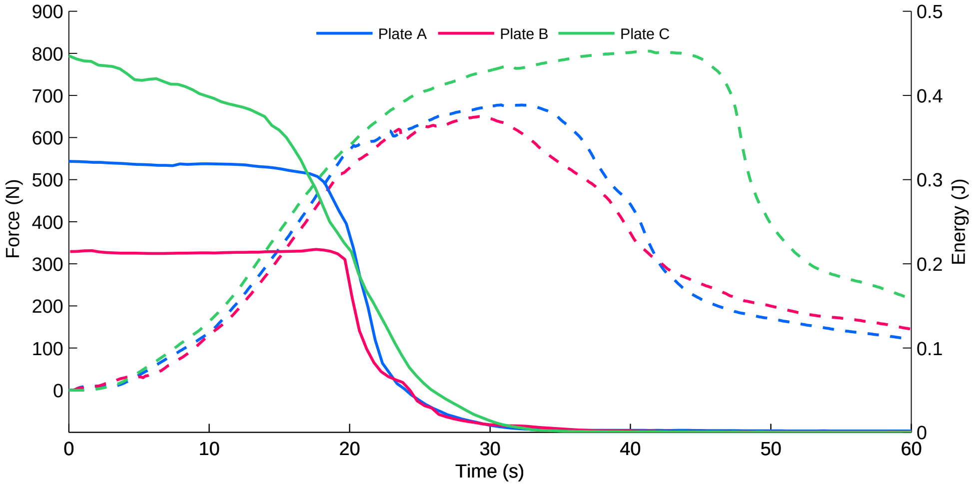

Figure 2.2.5: Received Energy and Force versus Time.

Velocity parameter fluctuates after 40 seconds of testing because the signal amplitude is too low to determine correctly the time of flight of the ultrasonic signal. In Figure 2.2.5, received energy (E_{rx}) was plotted for each specimen. It can be observed that the energy is constant during the elastic phase of the curve.

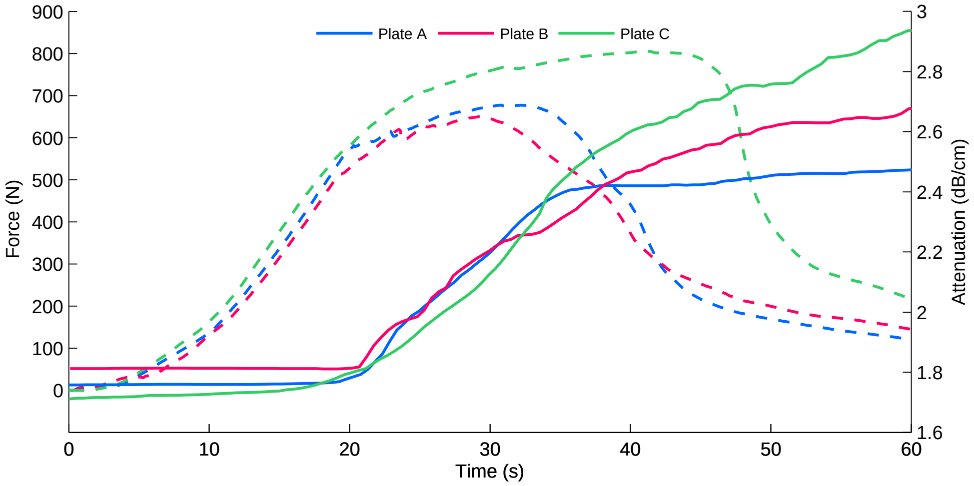

Figure 2.2.6: Material Attenuation and Force versus Time.

However, when the first microcraks appeared (change from elastic to plastic phase) the E_{rx} parameter drastically drops to very low values. Thus, after the plastic step, the value was negligible. This behaviour means that the energy transmission strongly depends on the formation of the first microcracks during the test. When the material comes in plastic stage, energy decays quickly to zero due to the cracks and subsequent subsection loss.

Figure 2.2.6 shows the attenuation (α_{mat}) of the material during the bending test. This parameter is inversely related to received energy (E_{rx}), therefore it has similar trends. The α_{mat} is being constant at the beginning of the essay and reaching higher values when the plastic stage starts. Non-linear parameter ($\beta_3^{\%}(t)$) curves were plotted in Figure 2.2.7. This parameter shows clearly the instant when the curve in elastic stage turns on plastic behaviour due to the micro-cracking (and subsequent macro-cracking and subsection loss), beginning with a slight increment for few seconds (between 15 and 20 second testing time) and high increment when plastic stage begins indicating greater damage.

As can be observed, both mechanical and ultrasonic parameters behaviours were very similar among three specimens. In Figure 2.2.8 all parameters for one specimen (plate B) are plotted in order too see directly differences among them during the test. Mechanical and ultrasonic parameters were normalized, thus all

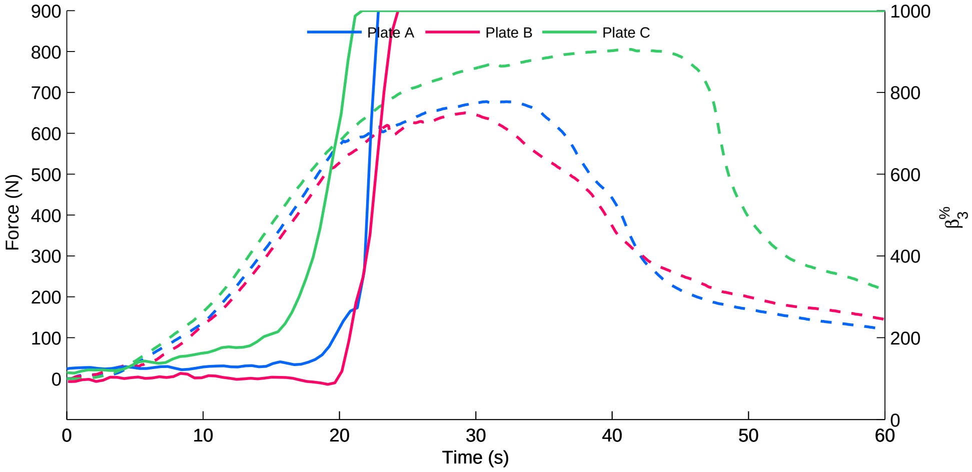

Figure 2.2.7: Non-linear parameter and Force versus Time.

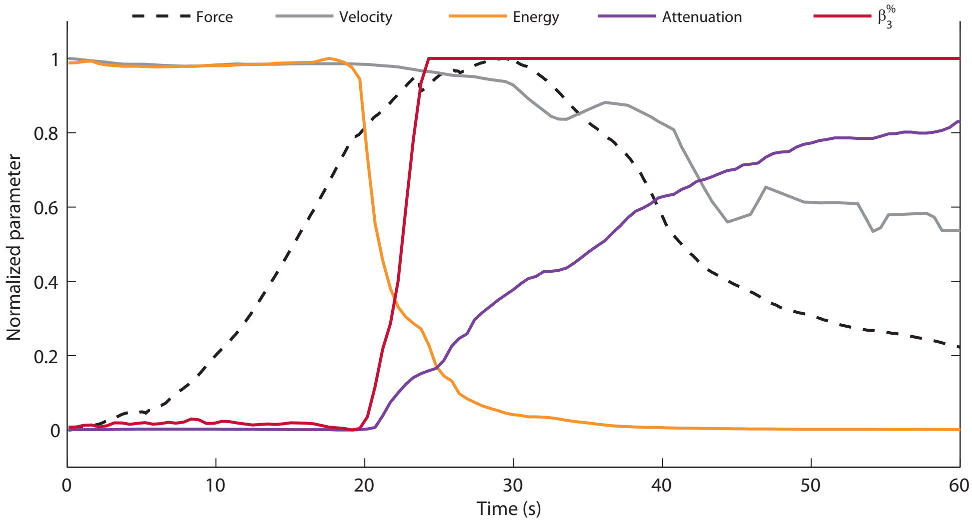

Figure 2.2.8: Normalized parameters versus Time.

values were in the 0-1 range. All wave parameters are sensitive to the changes of the material when the mechanical behaviour of the material turns from elastic to plastic stage but $\beta_3^{\%}(t)$ has a sudden change on early plastic stage, marking the beginning of the plastic deformations.

2.2.4 Conclusions

The bending test process of glass-fiber reinforced cement (GRC) has been successfully monitored by means of the study of ultrasonic pulses. Loading (constant displacement rate) and ultrasonic parameters were compared in the time scale. Elastic deformation step in the mechanical test does not produce significative changes in pulse velocity, energy, attenuation and non-linearities of the ultrasonic received signals. In the beginning of the plastic step in the mechanical test, significant changes in energy, attenuation and non-linearities has been identified. However, the change in the velocity pulse was very less important. The change in the ratio of the fundamental harmonic (A_1) and the third harmonic (A_3) was the highest found, being thus this parameter (non-linearity) the most relevant for detecting the plastic step. In this step, microcraking of the matrix has been produced because the mechanical loading, and this alteration in the matrix activates the generation of non-linearities.

References

[1] A. J. Majumdar, J. Ryder, and B. R. Station, *Glass fibre reinforcement of cement products*. Garston, England: Building Research Station, 1968.

[2] A. Bentur, *Fibre reinforced cementitious composites*. Taylor & Francis, 1990.

[3] V. M. Maholtra and N. J. Carino, Eds., *Handbook on Non destructive Testing on Concrete*. CRC Press, 2004, vol. 1.

[4] J. A. Bogas, M. G. Gomes, and A. Gomes, “Compressive strength evaluation of structural lightweight concrete by non-destructive ultrasonic pulse velocity method,” *Ultrasonics*, vol. 53, no. 5, pp. 962–972, 2013.

[5] A. Jain, A. Kathuria, A. Kumar, Y. Verma, and K. Murari, “Combined use of non-destructive tests for assessment of strength of concrete in structure,” *Procedia Engineering*, vol. 54, pp. 241–251, 2013.

[6] T. P. Philippidis and D. G. Aggelis, “Experimental study of wave dispersion and attenuation in concrete,” *Ultrasonics*, vol. 43, no. 7, pp. 584–595, 2005.

[7] S. Popovics, J. L. Rose, and J. S. Popovics, “The behaviour of ultrasonic pulses in concrete,” *Cement and Concrete Research*, vol. 20, no. 2, pp. 259–270, 1990.

[8] L. Vergara, J. Gosálbez, J. V. Fuente, R. Miralles, and I. Bosch, “Measurement of cement porosity by centroid frequency profiles of ultrasonic grain noise,” *Signal Processing*, vol. 84, no. 12, pp. 2315–2324, 2004.

[9] L. Vergara, R. Miralles, J. Gosálbez, F. J. Juanes, L. G. Ullate, J. J. Anaya, M. G. Hernández, and M. A. G. Izquierdo, “NDE ultrasonic methods to characterise the porosity of mortar,” *NDT & E International*, vol. 34, no. 8, pp. 557–562, 2001.

[10] D. G. Aggelis and T. P. Philippidis, “Ultrasonic wave dispersion and attenuation in fresh mortar,” *NDT & E International*, vol. 37, no. 8, pp. 617–631, 2004.

[11] H. Ogi, T. Hamaguchi, and M. Hirao, “In-situ monitoring of ultrasonic attenuation during rotating bending fatigue of carbon steel with electromagnetic acoustic resonance,” *Journal of Alloys and Compounds*, vol. 310, no. 1-2, pp. 436–439, 2000.

[12] F. Moradi-Marani, P. Rivard, C. Lamarche, and S. Kodjo, “Evaluating the damage in reinforced concrete slabs under bending test with the energy of ultrasonic waves,” *Construction and Building Materials*, vol. 73, pp. 663–673, 2014.

[13] J. Krautkrämer and H. Krautkrämer, *Ultrasonic testing of materials*. Springer-Verlag, 1983.

[14] P. A. Gaydecki and F. M. Burdekin, “The propagation and attenuation of medium-frequency ultrasonic waves in concrete: a signal analytical approach,” *Measurement Science and Technology*, vol. 3, p. 126, 1992.

[15] M. Molero, I. Segura, S. Aparicio, M. G. Hernández, and M. A. G. Izquierdo, “On the measurement of frequency-dependent ultrasonic attenuation in strongly heterogeneous materials,” *Ultrasonics*, vol. 50, no. 8, pp. 824–828, 2010.

[16] B. Standard, *Precast concrete products - Test method for glass-fibre reinforced cement - Part 5. Measuring bending strength, 'Complete bending test' method.* 1998.

[17] A. Shah and Y. Ribakov, “Non-linear ultrasonic evaluation of damaged concrete based on higher order harmonic generation,” *Materials & Design*, vol. 30, no. 10, pp. 4095–4102, 2009.

2.3 Optimized ultrasonic attenuation measures for non-homogeneous materials[3]

[3] *V. Genovés, J. Gosálbez, A. Carrión, R. Miralles, and J. Payá. "Optimized ultrasonic attenuation measures for non-homogeneous materials," Ultrasonics, vol. 65, pp. 345–352, 2016.*

Abstract

In this paper the study of frequency-dependent ultrasonic attenuation in strongly heterogeneous materials is addressed. To determine the attenuation accurately over a wide frequency range, it is necessary to have suitable excitation techniques. Three kinds of transmitted signals have been analysed, grouped according to their bandwidth: narrowband and broadband signals. The mathematical formulation has revealed the relation between the distribution of energy in their spectra and their immunity to noise. Sinusoidal and burst signals have higher signal-to-noise ratios (SNRs) but need many measurements to cover their frequency range. However, linear swept-frequency signals (chirp) improve the effective bandwidth covering a wide frequency range with a single measurement and equivalent accuracy, at the expense of a lower SNR. In the case of highly attenuating materials, it is proposed to use different configurations of chirp signals, enabling injecting more energy, and therefore, improving the sensitivity of the technique without a high time cost. Thus, if the attenuation of the material and the sensitivity of the measuring equipment allows the use of broadband signals, the combination of this kind of signal and suitable signal processing results in an optimal estimate of frequency-dependent attenuation with a minimum measurement time.

2.3.1 Introduction

Concrete is a non-homogeneous material prepared by mixing cement, aggregates, and water, used mainly in the field of civil and building engineering [1]. Due to its non-homogeneous structure, this material in its hardened state is composed by air voids, interfaces between the aggregates and hydrated cement paste, microcracks, and other defects inside its microstructure. For that reason, concrete is a very dispersive material and hard to measure (in order to know its physical and mechanical conditions) indirectly with Non-Destructive Testing (NDT) techniques [2].

Several authors have tried to test cement-based materials using different NDT in order to characterize the properties of concrete and detect damage by means of monitoring diverse parameters [3–5].

Due to its robustness, one of the most widely used parameters for ultrasonic NDT is the ultrasonic pulse velocity. However, attenuation is considered to be a parameter that is very sensitive to the structural properties of the material. Taking into account that it is a parameter related to the energy of the wave, it is more affected than ultrasonic velocity in an experimental setup, such as by coupling problems between the ultrasonic sensors and the analysed material, and energy losses due to wires, connectors, devices, etc. [6–9]. Despite these problems, the determination of the frequency-dependent ultrasonic attenuation, $\alpha_{mat}(f)$, [6, 8, 10–12], is a useful parameter due to its sensitivity to many defects in a material (voids, cracks...) and properties, specifically for concrete, where the water to cement ratio and the cement to aggregate ratio are important variables for concrete design and determine its mechanical and physical properties.

Several authors have used different techniques to measure the attenuation in cementitious materials. The typical setup is a through-transmission, where the transmission transducer is excited by an electrical signal to generate an ultrasonic signal. The transmitted signals include narrowband [8, 13–15] and broadband signals [6, 8, 16]. On the one hand, narrowband signals provide good performance against high attenuating materials, due to their high signal to noise ratio (SNR), but they require a large number of measurements to estimate the $\alpha_{mat}(f)$ curve (one measurement per each point of the curve). On the other hand, broadband signals require much less measurements because they cover a wider frequency range, but are more affected by noise because its energy is distributed over a wider frequency range.

Using broadband signals implies several advantages. Beyond the practical ones (time cost), there exist real applications which cannot be correctly monitored due to the fact that the system under study varies quickly in time. In such a situations, what is needed is the use of a configuration which allows measuring the attenuation efficiently without losing accuracy. The aims of this paper are to analyse each kind of transmitted signal, to provide an optimal method to obtain the frequency-dependent attenuation, $\alpha_{mat}(f)$, and to compare the attenuation results achieved by each configuration in a particular real application: measuring Portland cement mortar specimens.

The remainder of this paper is structured as follows. Section 2.3.3 describes and mathematically formulates the analysis of two narrowband signals (sinusoidal and burst signals) and a broadband signal (chirp signal), as well as the theoretical and experimental expressions for $\alpha_{mat}(f)$ in each case. Different configurations for the chirp signal are analysed in order to evaluate their noise immunity. In Section 2.3.2 the materials and test layout for the experiment which validates the aforementioned expressions are explained. Section 2.3.4 presents the attenuation results and, finally, the conclusions are summarized.

2.3.2 Experimental

2.3.2.1 Materials and sample preparation

Mortar specimens were manufactured according to Spanish standard UNE EN 196-1:2005 [17]. In order to improve the statistical analysis of the processed signals, three mixes were performed. Each mix was composed of 450 grams of CEM I 52,5-R Portland cement, 1350 grams of silica sand, and 225 grams of water. The results of these mixes were nine specimens of 40 × 40 × 160 mm^3 standardized mortar, with 0.5 water to cement ratio and 1:3 cement to aggregate ratio. After the iron moulds were filled with the fresh mortar, they were stored in a wet chamber (20 °C and 100% RH) for 24 hours. After that, the specimens were released and cured under water (saturated with calcium hydroxide) at 20 °C in the wet chamber for 90 days.

2.3.2.2 Test layout

An ultrasonic through-transmission setup was selected because it offers good penetration and good accuracy for determination of attenuation. The disposition of the equipment is shown in Figure 2.3.1. The transducers (transmitter and receiver) used were the $K1SC$ (General Electric). Both are broadband transducers with a bandwidth centered at 1 MHz.

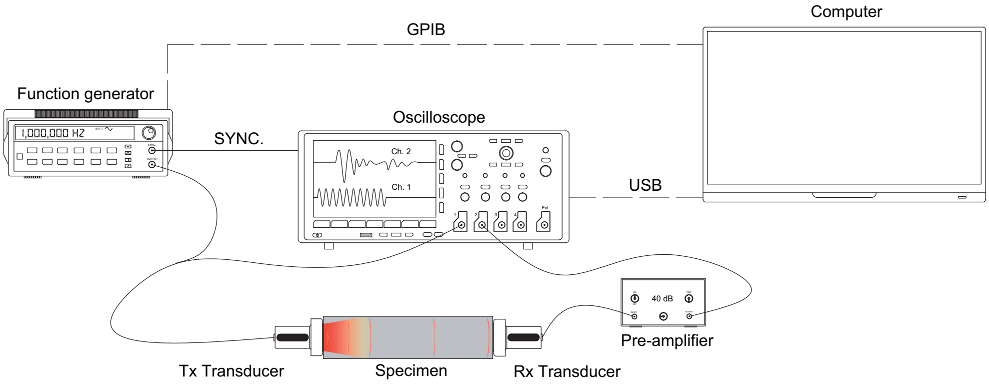

Figure 2.3.1: Scheme of equipment used in a typical ultrasonic inspection.

The transmitter transducer was excited directly by a programmable signal generator (Agilent 33120A) while the reception transducer was connected to a

40 dB preamplifier (Panametrics $5600B$). The received and amplified ultrasonic signals were captured using a digital oscilloscope (Tektronix $DPO3014$) with a sampling frequency of 25 MHz. Finally, a laptop was used to control the signal generator and to acquire and store the digitized signals. The ultrasonic transducers were placed facing the longitudinal axis of the specimen. They were fixed by two plastic clamps: a movable one to adjust to the specimen, and a fixed one. Ultrasonic gel at the transducer specimen interface was used as an impedance coupling medium.

2.3.3 Mathematical background

In a through-transmission inspection, the energy spectral density (ESD)[†] of the received signal (in the frequency domain), $S_{rx}(f)\ [dB]$, can be modeled by

$$S_{rx}(f) = S_{tx}(f) - \alpha_{mat}(f) \cdot d_{mat} - \alpha_{equip}(f) \tag{2.3.1}$$

where $S_{tx}(f)\ [dB]$ is the ESD of the transmitted signal, $\alpha_{mat}(f)\ [dB/cm]$ is the attenuation produced by the specimen, $d_{mat}\ [cm]$ is the distance between both transducers, and $\alpha_{equip}(f)\ [dB]$ is the attenuation due to the measuring equipment (amplifier, wires, and frequency response of the emitter and receiver).

From Eq. 2.3.1, the attenuation $\alpha_{mat}(f)[dB/cm]$ of the material can be obtained in terms of the other variables, yielding

$$\alpha_{mat}(f) = \frac{10log\left(S_{tx}(f)\right) - 10log\left(S_{rx}(f)\right) - \alpha_{equip}(f)[dB]}{d_{mat}}. \tag{2.3.2}$$

The challenge of this study lies in the estimation of the $S(f)$, which relates the transmitted energy/power and received energy/power as a function of frequency. The following aspects must be taken into account.

The signal to noise ratio (SNR) is directly proportional to the sensitivity of the attenuation parameter. Therefore, the kind of transmitted signal and its energy distribution in the frequency domain will affect the accuracy of the method. Working with sinusoidal or burst signals, the energy will be concentrated in a narrow band (higher SNR), but the estimation of $\alpha_{mat}(f)$ will correspond only to that narrow bandwidth. Consequently, in order to cover a wide spectrum, it is required to employ a higher number of input signals varying the fundamental frequency (f_0). On the other hand, in the case of a chirp signal, the energy will be distributed over a wider band (lower SNR) and the estimation of $\alpha_{mat}(f)$ covers a higher range of

---

[†] The energy spectral density, $S(f)$, of a finite time signal, $x(t)$, is defined as $S(f) = |X(f)|^2$, where $X(f) = \int_{t_0}^{t_1} x(t)e^{-j2\pi f t}dt$ is the Fourier Transform of the signal $x(t)$.

frequencies with a single input signal. It must be noticed that a good characterization of a highly attenuating material could require the use of signals with a high density energy. In Figure 2.3.2, the temporal and frequency domains of the three types of signals are shown. It can be easily appreciated how the density of energy of the sinusoidal and burst signals is higher than that of the chirp signal.

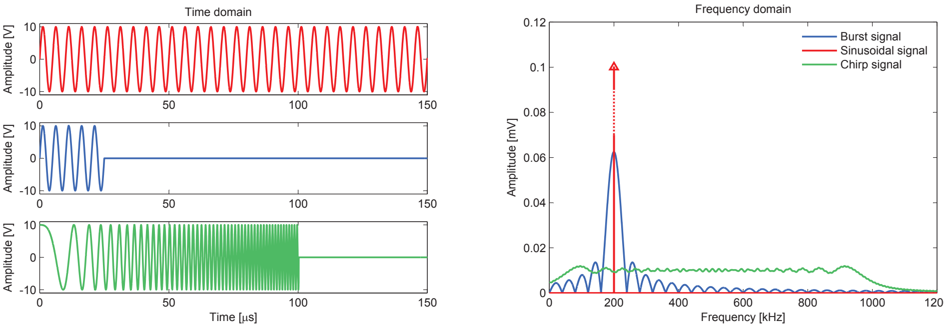

Figure 2.3.2: Comparison between narrowband signals (sinusoidal and burst) and broadband signals (chirp) in the temporal domain (left column) and frequency domain (right column). The red line represents a sinusoidal signal at 200 kHz, the blue line represents a burst signal of 5 cycles at 200 kHz, and the green line represents a chirp signal sweeping a frequency range from 100 to 900 kHz in 100 μs.

The frequency response of the equipment and, mainly, of the transducers, $\alpha_{equip}(f)$, limits the bandwidth that they are able to manage. Usually, the best performance is obtained at the fundamental frequency of the transducer, but it is also possible to work on the pass-band taking into account the required calibration process. The choice of the fundamental frequency depends on the material under inspection.

In this paper, the aforementioned transmitted signals are analysed and proposed for evaluating the attenuation of the material, $\alpha_{mat}(f)$, in order to compare their accuracies and time costs. To obtain $\alpha_{mat}(f)$, it will be necessary to estimate the power/energy of the transmitted and received signals as well as the attenuation introduced by the equipment. The power/energy of the transmitted signal will be computed from its well-known theoretical expressions. However, the power/energy of the received signal will be estimated from the real acquired signals digitalized by the oscilloscope. The attenuation of the equipment will be obtained by the calibration process described in Section 2.3.3.4.

2.3.3.1 Sinusoidal signal

The theoretical model of a transmitted pure sinusoidal signal is

$$s_{tx}(t) = A_{tx} cos\left(2\pi f_0 t + \phi_{tx}\right), \tag{2.3.3}$$

where A_{tx} is the amplitude of signal, f_0 is its fundamental frequency, and ϕ_{tx} is its phase, which will be assumed null. An example is shown in Figure 2.3.2, where the selected parameters for are $A_{tx} = 10$ and $f_0 = 200$ kHz. It is accepted that this signal is periodic, and therefore, it has an infinite time duration.

The theoretical spectrum of this signal (Eq. 2.3.4) gives the power contributed by a single frequency, shown in Figure 2.3.2. The power of this signal (P_{tx}) can be estimated directly from its amplitude, A_{tx} (Eq. 2.3.5). It has been assumed that the propagation medium, equipment, and transducers behave linearly. This implies that no new frequency components will be generated, and the received signal will be the same as the input signal except with a different amplitude and phase, which will depend only on the behaviour of the material and equipment, so that the power of the received signal can be estimated from the amplitude of the received sinusoidal signal, $A_{rx}^{(f_0)}$ (Eq. 2.3.6).

$$S_{tx}(f) = \left| \frac{A_{tx}}{2} \left(\delta(f - f_0) + \delta(f + f_0) \right) \right|^2 \tag{2.3.4}$$

$$P_{tx} = \frac{A_{tx}^2}{2} = \frac{\max\{s_{tx}^2(t)\}}{2} \tag{2.3.5}$$

$$s_{rx}(t) = A_{rx}^{(f_0)} cos\left(2\pi f_0 t + \phi_{rx}^{(f_0)}\right) \rightarrow P_{rx}^{(f_0)} = \frac{\left(A_{rx}^{(f_0)}\right)^2}{2} \tag{2.3.6}$$

Hence, the attenuation due to the material for the input frequency $\alpha_{mat}(f_0)$ can be calculated by using both Eq. 2.3.5 and Eq. 2.3.6, resulting in the following equation:

$$\begin{aligned} \alpha_{mat}(f_0) &= \frac{P_{tx}[dB] - P_{rx}^{(f_0)}[dB] - \alpha_{equip}(f_0)[dB]}{d_{mat}} \\ &= \frac{10log_{10}\left(\frac{A_{tx}^2}{2}\right) - 10log_{10}\left(\frac{\left(A_{rx}^{(f_0)}\right)^2}{2}\right) - \alpha_{equip}(f_0)[dB]}{d_{mat}} \end{aligned} \tag{2.3.7}$$

In order to obtain the values of the $\alpha_{mat}(f_0)$ curve, it is required to do a sweep of the input fundamental frequency (f_0). The described calculations must be repeated as many times as the number of points which make up the $\alpha_{mat}(f_0)$ curve. The main advantage of sinusoidal signals is the high SNR, which allows working properly on highly attenuating materials.

2.3.3.2 Burst signal

The burst signal is a common configuration used in NDT applications since it allows estimating simultaneously several ultrasonic parameters (attenuation, velocity, etc.). Its theoretical expression is a time-limited sinusoidal signal:

$$s_{tx}(t) = A_{tx} \cdot cos\left(2\pi f_0 t\right) \cdot rect\left(\frac{t - \frac{NT_0}{2}}{NT_0}\right) \tag{2.3.8}$$

where A_{tx} is the amplitude of the signal, f_0 is its fundamental frequency, $T_0 = \frac{1}{f_0}$ is its fundamental period, N is the number of cycles of the signal, and $rect(\cdot)$ is the rectangular function. An example is shown in Figure 2.3.2, where the parameters selected are $A_{tx} = 10$, $f_0 = 200$ kHz, and $N = 5$.

The total energy of a burst signal (Eq. 2.3.9) depends on its fundamental frequency f_0, the amplitude A_{tx}, and the number of cycles N, but its theoretical spectrum (Eq. 2.3.10) represented in Figure 2.3.2 shows that this energy is distributed over a bandwidth around the fundamental frequency. For this reason, the energy of the transmitted and received signals must be calculated from the spectrum over the bandwidth following Eq. 2.3.11 [18]. The selected bandwidth corresponds to the main lobe of the transmitted spectrum, $f_0 \pm \frac{f_0}{N}$, and the theoretical expression for the transmitted energy over this bandwidth is Eq. 2.3.12. This energy, $E^{(f_0)}_{tx,BW}$, also depends on f_0 and constitutes a constant ratio, 90%, of the total transmitted energy.

$$E^{(f_0)}_{tx} = \frac{A^2_{tx}}{2} N T_0 = \frac{A^2_{tx}}{2 f_0} N \tag{2.3.9}$$

$$S_{tx}(f) = \left| \frac{A_{tx} N T_0}{2} sinc\left((f - f_0) N T_0\right) e^{-j2\pi (f - f_0) N T_0} \right|^2 \tag{2.3.10}$$

$$E^{(f_0)}_{tx|rx,BW} = 2 \int_{<BW>} S_{tx|rx}(f) df = 2 \int_{f_0 - \frac{f_0}{N}}^{f_0 + \frac{f_0}{N}} S_{tx|rx}(f) df \; [J] \tag{2.3.11}$$

$$E^{(f_0)}_{tx,BW} = A^2_{tx} N \frac{1}{f_0} \frac{Si(2\pi)}{\pi} \; [J] \tag{2.3.12}$$

where $Si(\cdot)$ is the sine integral function. Using the theoretical transmitted energy (Eq. 2.3.12), and the received energy (Eq. 2.3.11), the expression of the attenuation for the corresponding input fundamental frequency, $\alpha_{mat}(f_0)$, becomes

$$\begin{aligned} \alpha_{mat}(f_0) &= \frac{E^{(f_0)}_{tx,BW}[dB] - E^{(f_0)}_{rx,BW}[dB] - \alpha_{equip}(f_0)[dB]}{d_{mat}} \\ &= \frac{10log\left(A^2_{tx}N\frac{1}{f_0}\frac{Si(2\pi)}{\pi}\right) - 10log\left(2\int_{f_0-\frac{f_0}{N}}^{f_0+\frac{f_0}{N}} S_{rx}(f)df\right) - \alpha_{equip}(f_0)[dB]}{d_{mat}} \end{aligned} \tag{2.3.13}$$

Each signal has associated a fundamental frequency, f_0, so that each measurement will evaluate just one point of the curve, $\alpha_{mat}(f)$. This implies that a frequency sweep of the fundamental frequency, f_0, has to be implemented to obtain the curve $\alpha_{mat}(f)$ evaluated over the whole defined interval. This means taking at least one temporal measurement for each frequency, thereby restricting the number of analysed frequencies due to the increase in the measurement time.

2.3.3.3 Chirp signal

Swept-frequency signals (chirp) are broadband signals which enable the estimation of the curve $\alpha_{mat}(f)$ with a single measurement. The mathematical expression of a linear chirp signal is

$$s_{tx}(t) = A_{tx}cos\left(2\pi f_0 t + \pi\Delta_{f_{max}}t^2\right)rect\left(\frac{t-\frac{T}{2}}{T}\right) \tag{2.3.14}$$

$$\Delta_{f_{max}} = \frac{f_{max} - f_0}{T} \tag{2.3.15}$$

where A_{tx} is the amplitude of the signal, f_0 is its fundamental frequency, T is the active time of the signal, and $\Delta_{f_{max}}$ controls the maximum frequency ($f_{max} = f_0 + T\Delta_{f_{max}}$) which is reached at T seconds (Eq. 2.3.15). An example is shown in Figure 2.3.2, where the parameters selected are $A_{tx} = 10$, $f_0 = 10$ kHz, $f_{max} = 1$ MHz, and $T = 100\,\mu$s.

The mathematical expression of the spectrum of a chirp signal is more complicated than the other analysed spectra (Eq. 2.3.16)[†], but it allows estimating $\alpha_{mat}(f)$ by applying Eq. 2.3.2 directly.

$$\begin{aligned} S_{tx}(f) = \Bigg| & \frac{A_{tx}}{\sqrt{2\Delta_{f_{max}}}} e^{-j\pi(f-f_0)^2} \left[C\left(\sqrt{2}\frac{f-f_0}{\sqrt{\Delta_{f_{max}}}} \right) + jS\left(\sqrt{2}\frac{f-f_0}{\sqrt{\Delta_{f_{max}}}} \right) \right. \\ & \left. -C\left(\sqrt{2}\frac{\Delta_{f_{max}}T+f-f_0}{\sqrt{\Delta_{f_{max}}}} \right) - jS\left(\sqrt{2}\frac{\Delta_{f_{max}}T+f-f_0}{\sqrt{\Delta_{f_{max}}}} \right) \right] \Bigg|^2 \end{aligned} \tag{2.3.16}$$

As shown in Figure 2.3.2, the spectrum of the transmitted pulse is distributed along a frequency bandwidth. At the expense of decreasing the SNR, broadband signals excite several frequencies simultaneously. A single acquisition allows computing the $\alpha_{mat}(f)$ curve from the theoretical transmitted and received spectra. Additionally, a pseudo-continuous attenuation curve is obtained instead of a discretization of $\alpha_{mat}(f)$.

[†] $C(x)$ and $S(x)$ are the Fresnel integrals defined as $C(x) = \int_0^x cos(t^2)dt$ and $S(x) = \int_0^x sin(t^2)dt$.

Table 2.3.1: Main parameters of each configuration: Constant Interval Energy and Constant Total Energy.

Number of intervals	Bandwidth/ int [kHz]	Mode 1: Constant Interval Energy			Mode 2: Constant Total Energy		
		T/int [μs]	E/int [mJ]	E_{Tot} [mJ]	T/int [μs]	E/int [mJ]	E_{Tot} [mJ]
1	990	100	5.2	5.2	100	5.2	5.2
2	495	100	5.2	10.4	50	2.6	5.2
4	247.5	100	5.2	20.8	25	1.3	5.2
6	165	100	5.2	31.2	16.6	0.9	5.2
8	123.75	100	5.2	41.6	12.5	0.6	5.2
10	99	100	5.2	52	10	0.5	5.2

Taking into account that the energy is distributed over the bandwidth of the chirp signal, the original chirp signal, which swept from 10 KHz to 1 MHz, has been split up into smaller frequency intervals. The division can be done in two different ways: keeping constant the energy in each interval (Mode 1) or keeping constant the total energy (Mode 2). This analysis allows controlling the SNR of each interval and, therefore, comparing the accuracy of each configuration versus the number of intervals.

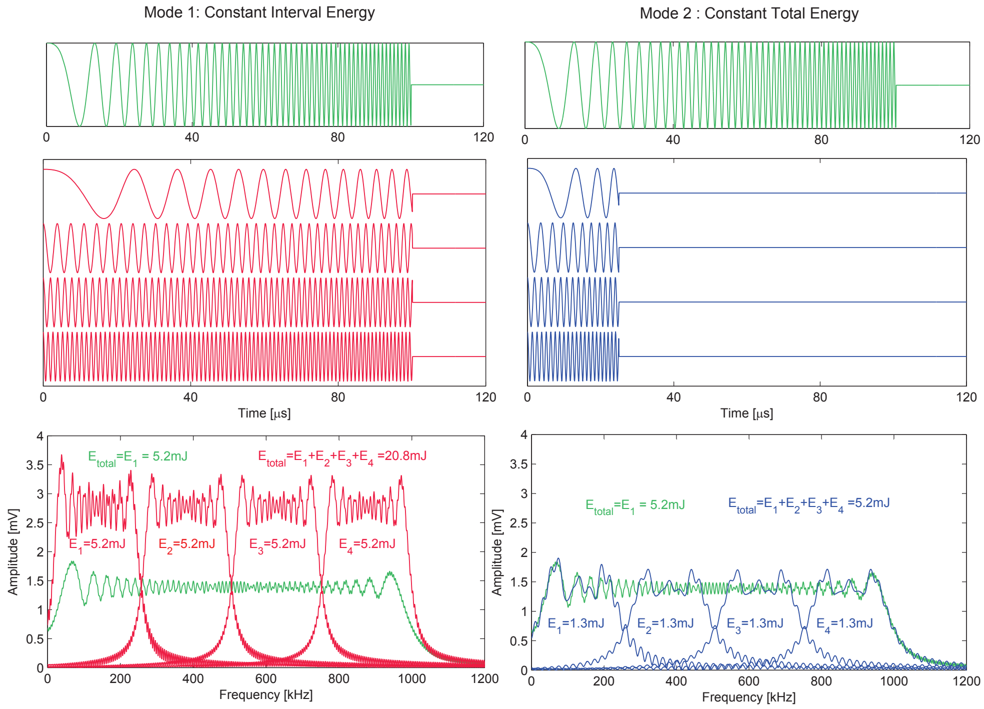

Figure 2.3.3: Comparison between an original chirp signal and its equivalent signals, Mode 1 (Constant Interval Energy) and Mode 2 (Constant Total Energy) in the time domain (second row) and frequency domain (third row).

Figure 2.3.3 compares the original chirp signal and both setups in the time and frequency domains. The first column corresponds to Mode 1: Constant Interval Energy. For this setup, the value T was fixed to 100 μs and the energy to 5.2 mJ in each frequency interval. Therefore, the more intervals, the greater the total injected energy. In the frequency domain, it can be noticed that the total energy is four times (four intervals) greater than in the original chirp.

The second column corresponds to Mode 2: Constant Total Energy. In this configuration, the total energy injected was fixed to 5.2 mJ by reducing T depending on the number of intervals. Its spectrum shows that the energy of each interval is reduced to keep constant the total energy (by keeping down the signal duration). Table 2.3.1 summarizes the main parameters of these setups for different numbers of intervals.

2.3.3.4 Calibration process

The calibration process was carried out with the emitter and receiver face to face without any material between them. In this situation, Eq. 2.3.2 simplifies to Eq. 2.3.17 (due to the absence of the tested material):

$$\alpha_{equip}(f) = S_{tx}(f) - S_{rx}(f)\ [dB] \tag{2.3.17}$$

where $S_{tx}(f)\ [dB]$ is the energy spectral density (ESD) of the transmitted signal and $S_{rx}(f)\ [dB]$ is the ESD of the received signal. Both variables must be computed according to the analysed expressions seen in Section 2.3.3, depending on the transmitted waveform. The testing process parameters were equal to the material analysis ones except for the transmitted signal amplitude, which was reduced by up to 0.5 Vp, to avoid saturation.

Figure 2.3.4 shows the $-\alpha_{equip}(f)$ obtained from calibration process. The three curves correspond to the three different transmitted signals: sinusoidal, burst, and chirp signals. The fact that the curves are almost equivalent (mean standard deviation is 2.67%) shows that the outlined expressions in Section 2.3.3 are correct. These curves are used to compensate the received signal during the material measurement process.

2.3.4 Results and discussion

In this section, the results for the three types of signals are presented. The common parameter for all the signals is the amplitude of the transmitted signal, which was fixed at $A_{tx} = 10$ V. For the burst signal, the number of cycles was $N = 5$. For the sinusoidal and burst signals, the signal generator was set to sweep the fundamental frequency, f_0, from 1 kHz up to 1 MHz with increments of 5 kHz and a delay of 1 second between each analysed frequency. Therefore, for each specimen, 200 measurements were acquired (one for each fundamental frequency) and a frequency response of 200 points is obtained for $\alpha_{mat}(f)$. For the chirp signal, the analysed bandwidth was the same as for the sinusoidal and burst signals, but with just one measurement. The next sections describe and compare the results of the three signals applied to prismatic mortar specimens.

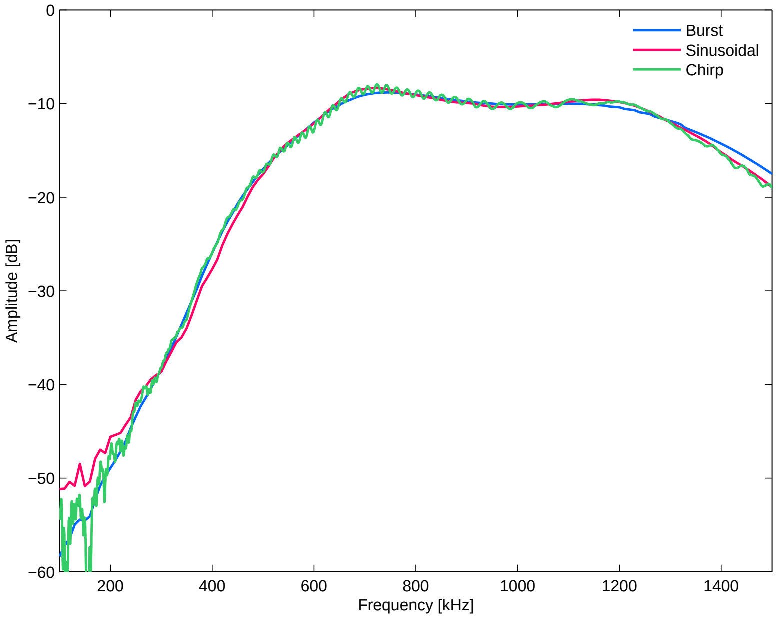

Figure 2.3.4: Frequency response of measuring equipment ($-\alpha_{equip}(f)$).

2.3.4.1 Sinusoidal signal

The attenuation curve, $\alpha_{mat}(f)$, obtained with a transmitted sinusoidal signal using the expressions developed in Section 2.3.3.1, is shown in Figure 2.3.5, in which can be seen the positive trend of the attenuation values as the frequency increases, as well as its low dispersion between measures (the shadowed area represents the 90% confidence intervals).

The evolution of the attenuation curve is proportional to the internal composition of the material under study (as the frequency increases, the attenuation parameter is sensitive to smaller particles/inhomogeneities). However, the results obtained for the attenuation of frequencies below 450 kHz are likely to correspond to the propagation of surface waves, proportional to the mechanical properties of the material and its geometry and not so much to its internal composition.

Throughout this section, the attenuation curve obtained for the sinusoidal input signal is defined as the reference attenuation curve. In order to compare the

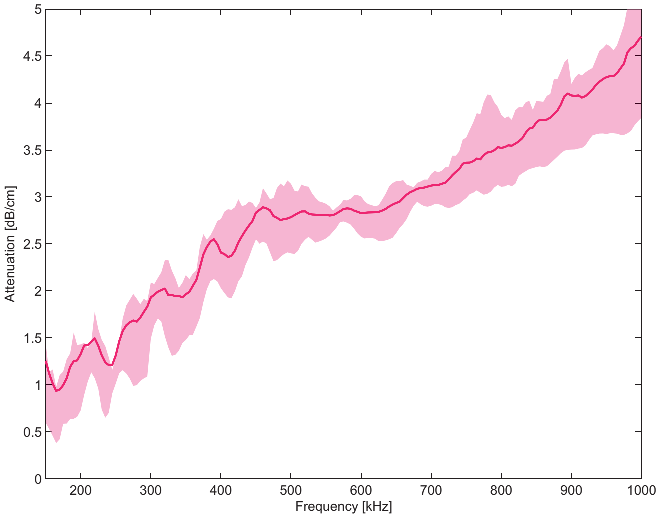

Figure 2.3.5: Frequency-dependent ultrasonic attenuation, $\alpha_{mat}(f)$, obtained with sinusoidal signal.

different results obtained, the root-mean-square error ($error_{RMS}$) expressed in Eq. 2.3.18 will be computed, where the function $error(f)$ is defined by Eq. 2.3.19.

$$error_{RMS} = \sqrt{\frac{1}{f_2 - f_1}\int_{f_1}^{f_2} |error(f)|^2 df} \tag{2.3.18}$$

$$error(f) = \alpha(f) - \alpha_{reference}(f) \tag{2.3.19}$$

2.3.4.2 Burst signal

The attenuation obtained with the burst sinusoidal signal is shown in Figure 2.3.6a. The result has the same trend as the case of the pure sinusoidal signal but it seems to have a smoother behavior. This is due to the fact that the attenuation here is computed as the integral of the power spectrum in the main lobe of the fundamental frequency (Eq. 2.3.11), which implies a frequency filtering. Figure 2.3.6b compares the attenuation curves obtained with the sinusoidal and burst signals. The $error_{RMS}$ between both curves is 0.15 dB (5.2%).

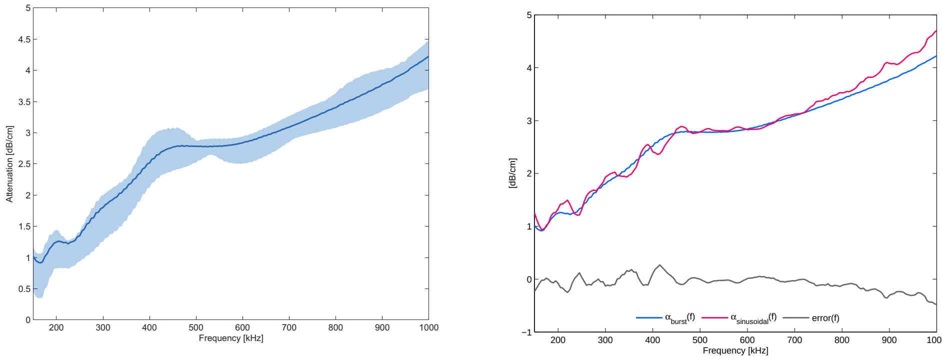

(a) **(b)**

Figure 2.3.6: Frequency-dependent ultrasonic attenuation, $\alpha_{mat}(f)$, obtained with burst signal.Comparison of the frequency-dependent ultrasonic attenuation, $\alpha_{mat}(f)$, obtained with sinusoidal (red) and burst (blue) signals. Error curve (black), $error(f)$ between the two results.

2.3.4.3 Chirp signal

In this section, the results obtained for the chirp signal are presented. Firstly, both setups (Constant Interval Energy and Constant Total Energy) are analysed in terms of the $error_{RMS}$ and compared in order to determine the optimal setup. To this end, the total bandwidth has been divided into different numbers of frequency intervals, as was explained in Section 2.3.3.3. With the optimal setup, the results are offered and compared with those of the sinusoidal and burst signals.

Table 2.3.2 shows the mean value of $error_{RMS}$ for the two setups and the different numbers of intervals. The errors between them are quite similar, although those for the Constant Interval Energy are slightly lower than those for the Constant Total Energy as the number of intervals increases. The error is smaller for Mode 1 and as the number of intervals increases, this seems logical since it enhances the injected energy for the analysis of the material. However, the differences between the configurations are not very significant because the material does not attenuate too much and any setup allows enough SNR for the required analysis.

Table 2.3.2: RMS Error for intervals and setup mode.

Number of intervals	Bandwidth per interval [kHz]	Mode 1: Constant Interval Energy $error_{RMS}$ [dB]	Mode 2: Constant Total Energy $error_{RMS}$ [dB]
1	990	0.22 ± 0.05	0.23 ± 0.04
2	495	0.21 ± 0.04	0.25 ± 0.04
4	247.5	0.22 ± 0.05	0.25 ± 0.03
6	165	0.20 ± 0.05	0.24 ± 0.04
8	123.75	0.21 ± 0.04	0.25 ± 0.02
10	99	0.20 ± 0.04	0.23 ± 0.03

Figs. 2.3.7a and 2.3.7b represent three curves: the sinusoidal attenuation (as the reference attenuation), the chirp attenuation, and $error(f)$ for the Constant Interval Energy setup for one specimen. Figure 2.3.7a corresponds to 1 interval (the bandwidth is not divided), while Figure 2.3.7b corresponds to 4 intervals. As can be seen, both graphs offer similar trends and errors despite four independent signals having been used in the latter case.

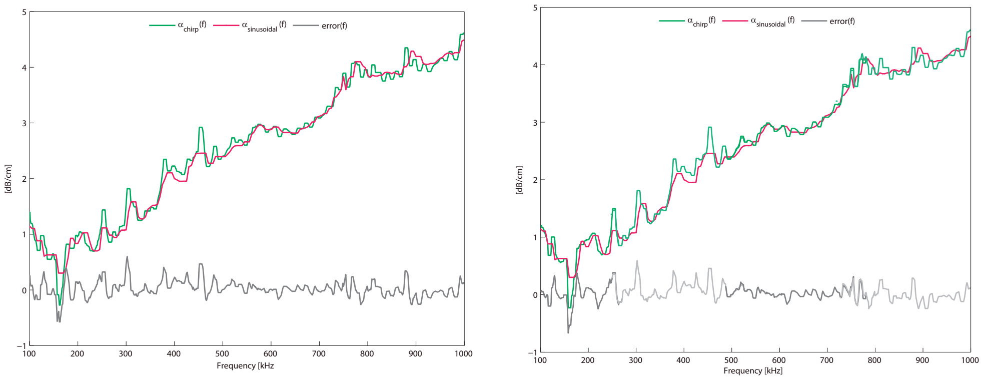

(a) **(b)**

Figure 2.3.7: Comparison of the frequency-dependent ultrasonic attenuation, $\alpha_{mat}(f)$, obtained with sinusoidal (red) and original chirp (green) signals. Error curve (black), $error(f)$ between these two results. Figure 2.3.7a one interval. Figure 2.3.7b four intervals.

Taking into account that using the Constant Interval Energy configuration, no significant improvement was achieved by dividing the chirp signal into subintervals, only one interval is selected as the optimal setup for attenuation estimation by means of the chirp signal. The attenuation obtained with the chirp signal is shown in Figure 2.3.8a. The mean attenuation curves of the three analysed signals are superimposed and shown in Figure 2.3.8b for comparison. It can be seen that the three methods behave similarly, with minimal deviations. The behavior of the chirp attenuation is more similar to that of the sinusoidal attenuation because none of them perform a bandwidth integration for the attenuation estimation as does the burst signal. The $error_{RMS}$ (assuming the sinusoidal curve as the reference) is 0.15 dB for the burst signal and 0.08 dB for the chirp signal, which means the three signals offer similar estimations of $\alpha_{mat}(f)$. Table 2.3.3 summarizes all the quantified results: the mean value of the deviation between the measurements, $error_{RMS}$, as well as the acquisition time needed by each transmitted signal assuming that 200 points of the curve of attenuation are analysed.

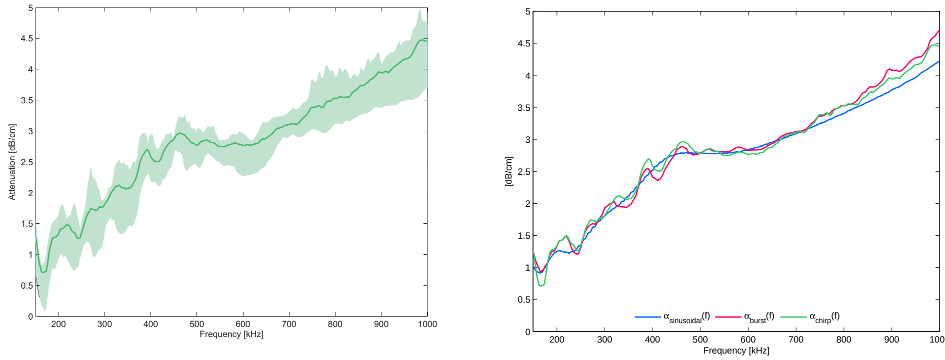

(a) **(b)**

Figure 2.3.8: Figure 2.3.8a, Frequency-dependent ultrasonic attenuation, $\alpha_{mat}(f)$, obtained with chirp signal. Figure 2.3.8b,Comparison of the frequency-dependent ultrasonic attenuation, $\alpha_{mat}(f)$, obtained with sinusoidal (red), burst (blue) and chirp (green) signals.

Table 2.3.3: Comparison of results of different transmitted signals. The acquisition time has been computed as the sum of the transmission time (approximately 0.5 seconds) and the delay between measurements (1 second, enough for the signal to stabilize).

	Deviation [dB]	$error_{RMS}$ [dB]	Acquisition time [s]
Sinusoidal signal	0.35	-	300
Burst signal	0.28	0.15	300
Chirp signal	0.34	0.08	0.5

2.3.5 Conclusions

In this paper the study of frequency-dependent ultrasonic attenuation in strongly heterogeneous materials was addressed. To determine the attenuation accurately over a wide frequency range, it is necessary to have suitable excitation techniques. Three kinds of transmitted signals have been analysed, grouped according to their bandwidth: narrowband and broadband signals. The mathematical formulation has revealed the relation between the distribution of energy in their spectra and their immunity to noise. Sinusoidal and burst signals have higher signal-to-noise ratios (SNRs) but need many measurements to cover their frequency range. However, linear swept-frequency signals (chirp) improve the effective bandwidth covering a wide frequency range with a single measurement and equivalent accuracy, at the expense of a lower SNR. In the case of highly attenuating materials, the use of different configurations of chirp signals was proposed, enabling injecting more energy, and therefore, improving the sensitivity of the technique without a high time cost. Thus, if the attenuation of the material and the sensitivity of the measuring equipment allows the use of broadband signals, the combination of this kind of signal and suitable signal processing results in an optimal estimate of frequency-dependent attenuation with a minimum measurement time. In future applications, the use of the optimal configuration for proper monitoring of processes with high temporal variation is proposed. Such processes do not allow the acquisition of a large number of measurements at a fixed fundamental frequency, and therefore, require the use of faster techniques.

Aknowledgements

This work has been supported by the Spanish Administration under grant BIA2014-55311-C2-2-P and BIA2014-55311-C2-1-P.

References

[1] P. C. Aïtcin, *Binders for Durable and Sustainable Concrete*, ser. Modern Concrete Technology. Taylor & Francis, 2007.

[2] V. M. Maholtra and N. J. Carino, Eds., *Handbook on Non destructive Testing on Concrete*. CRC Press, 2004, vol. 1.

[3] X. G. Tang, Y. J. Xie, and G. C. Long, "Application of non-destructive technology in evaluating concrete to sulfate attack," *Advanced Materials Research*, vol. 168-170, pp. 2565–2570, Dec. 2010.

[4] K. J. Leśnicki, J. Y. Kim, K. E. Kurtis, and L. J. Jacobs, "Characterization of ASR damage in concrete using Nonlinear Impact Resonance Scoustic Spectroscopy technique," *NDT & E International*, vol. 44, no. 8, pp. 721–727, 2011.

[5] C. Payan, V. Garnier, J. Moysan, and P. A. Johnson, "Applying nonlinear resonant ultrasound spectroscopy to improving thermal damage assessment in concrete," *The Journal of the Acoustical Society of America*, vol. 121, no. 4, EL125, 2007.

[6] M. Molero, I. Segura, S. Aparicio, M. G. Hernández, and M. A. G. Izquierdo, "On the measurement of frequency-dependent ultrasonic attenuation in strongly heterogeneous materials," *Ultrasonics*, vol. 50, no. 8, pp. 824–828, 2010.

[7] M. S. Diallo, M. Prasad, and E. Appel, "Comparison between experimental results and theoretical predictions for P-wave velocity and attenuation at ultrasonic frequency," *Wave Motion*, vol. 37, no. 1, pp. 1–16, 2003.

[8] D. G. Aggelis and T. P. Philippidis, “Ultrasonic wave dispersion and attenuation in fresh mortar,” *NDT & E International*, vol. 37, no. 8, pp. 617–631, 2004.

[9] V. Garnier, B. Piwakowski, O. Abraham, G. Villain, C. Payan, and J. F. Chaix, “Acoustic techniques for concrete evaluation: Improvements, comparisons and consistency,” *Construction and Building Materials*, vol. 43, pp. 598–613, 2013.

[10] T. P. Philippidis and D. G. Aggelis, “Experimental study of wave dispersion and attenuation in concrete,” *Ultrasonics*, vol. 43, no. 7, pp. 584–595, 2005.

[11] T. Seldis, “Enhanced experimental approach to measure the absolute ultrasonic wave attenuation.,” *Ultrasonics*, vol. 50, no. 1, pp. 9–12, 2010.

[12] P. A. Gaydecki and F. M. Burdekin, “The propagation and attenuation of medium-frequency ultrasonic waves in concrete: a signal analytical approach,” *Measurement Science and Technology*, vol. 3, p. 126, 1992.

[13] A. Shah, Y. Ribakov, and C. Zhang, “Efficiency and sensitivity of linear and non-linear ultrasonics to identifying micro and macro-scale defects in concrete,” *Materials & Design*, vol. 50, pp. 905–916, 2013.

[14] B. C. Kim and J. Y. Kim, “Characterization of ultrasonic properties of concrete,” *Mechanics Research Communications*, vol. 36, no. 2, pp. 207–214, 2009.

[15] W. Punurai, J. Jarzynski, J. Qu, K. E. Kurtis, and L. J. Jacobs, “Characterization of entrained air voids in cement paste with scattered ultrasound,” *NDT & E International*, vol. 39, no. 6, pp. 514–524, 2006.

[16] W. Punurai, J. Jarzynski, J. Qu, J. Y. Kim, L. J. Jacobs, and K. E. Kurtis, “Characterization of multi-scale porosity in cement paste by advanced ultrasonic techniques,” *Cement and Concrete Research*, vol. 37, no. 1, pp. 38–46, 2007.

[17] UNE, *EN 196-1:2005. Métodos de ensayo de cementos. Parte 1: Determinación de resistencias mecánicas*. 2005.

[18] S. S. Soliman and M. D. Srinath, *Continuous and Discrete Signals and Systems*. Prentice-Hall International, 1998.

2.4 Ultrasonic broadband signals monitoring of glass-fiber reinforced cement (GRC) bending tests[4]

[4] *V. Genovés, J. Gosálbez, A. Carrión, R. Miralles, and J. Payá. "Ultrasonic broadband signals monitoring of glass-fiber reinforced cement (GRC) bending tests," Cement and Concrete Composites, vol. 80, pp. 55–63, 2016.*

Abstract

In this study, complete ultrasonic monitoring of Glass-fiber Reinforced Cement plates under bending tests was addressed. In this kind of experiment, the mechanical properties of the specimen continuously change during the test, thus, the acquisition time of the ultrasonic signals is a critical variable. In order to overcome this drawback, a new ultrasonic procedure based on broadband signals (chirp) has been applied. Following this line of thought, the analysed ultrasonic parameters have been split into the parameters that only depend on time, and those that depend on both time and frequency. In particular, the frequency dependent attenuation parameter allows characterizing the evolution of the plate being damaged over a wide frequency range and significantly detecting the main two events happening during the experiment: the first crack and the maximum stress point. In short, this paper demonstrates the suitability of ultrasonic broadband signals for characterizing fiber-reinforced cementitious composites under bending stress.

2.4.1 Introduction

Glass-fiber reinforced cement (GRC) is a composite made of Portland cement mortar with a low water/cement (w/c) ratio with a high percentage of paste (water + cement) in relation to the aggregate. The addition of a high proportion of alkali resistant (AR) glass fibers to the mortar matrix (3%–5% by weight of mortar) improves the mechanical properties of the composite, particularly its toughness, flexural strength, and ductility. This composite has an important role in non-steel reinforced pre-cast concrete elements, such as sheets, panels and other slim shapes usually employed in building engineering and architecture, as well as in cast-in-situ sprayed-on surfaces [1, 2].

Recently, Non-Destructive Testing (NDT) techniques applied to concrete have been investigated, especially ultrasonics and acoustic spectroscopy, in order to obtain parameters related to the physical and mechanical properties of the material and its durability [3]. Some experimental studies have demonstrated that wave parameters such as the ultrasonic pulse velocity of P-waves are suitable for predicting the dynamic elastic modulus of the concrete, and that the velocity of the S-waves can predict the dynamic shear modulus. These parameters are proportional to the elastic and shear moduli of concrete and also to its compressive strength [4, 5]. Other studies based on ultrasound propagation indicate that wave attenuation should be measured for various frequencies, in order to characterise cement-based materials, determining their microstructure, porosity, and other characteristics in both the hardened [6–9] and fresh states [10].

Some studies of construction material tests by ultrasound monitoring have been reported in the literature. Many of them are related to research on metallic specimens because this type of material is used in other engineering fields. However, recent studies of bending tests of reinforced concrete slabs, using ultrasonic monitoring, have been carried out successfully [11, 12]. The first approach was recently published by the authors, in which the monitoring of GRC plates under a four point bending test using an ultrasonic pulse with a fixed frequency was carried out. Thus, the P-wave velocity, attenuation, energy and non-linear parameters were obtained [13](Section 2.2). Monitoring mechanical tests with non-destructive techniques provides a wealth of information about the material under study, allowing the prediction of its behaviour. Ultrasonic waves could be appropriate for following the changes during the mechanical test. GRC plates change their internal structure because micro-cracks develop during the bending test. In these conditions, different ultrasonic frequencies are needed to cover all the changes in the specimen. The disadvantage of this kind of test is the fact that the mechanical properties of the GRC plates change quickly during the test, and it is difficult to inject various signals with different frequencies to cover a wide spectrum. To solve this problem, the authors have also recently published a study of the suitability of broadband signals, comparing different methods and signals to obtain a reliable method to acquire the information of a wide bandwidth with one single signal (chirp) [14] (Section 2.3). This procedure permits monitoring a huge range of situations where the test-time has critical effects. The aim of this paper is to apply new ultrasonic acquisition techniques to support the previous results and provide new information about the GRC plates under stress, making use of the attenuation and non-linear ultrasonic parameters in the time and frequency domain.

The remainder of this paper is structured as follows. Section 2.4.2 describes the materials and specimens used in this study. It also presents the test layout, composed of the ultrasonic equipment and the mechanical test machine, as well as the ultrasonic parameters extracted from the signals during the experiments. In Section 2.4.3, the results are presented, correlating the ultrasonic parameters with mechanical curves. Finally, in Section 2.4.4, the conclusions are summarized.

2.4.2 Experimental

2.4.2.1 Materials and specimens

In this experiment, the specimen dimensions for the bending test were 325 × 50 × 20 mm. The specimens were cut from a 400 × 400 × 20 mm mother plate, obtaining five plates for the tests. Table 3.1.2 shows the proportions and information about the raw materials used to fabricate the GRC mother plate. The specimens were made according to the BS EN 1170-5 standard [15].

Table 2.4.1: Used dosage for one GRC plate specimen.

Material	Type	Weight [g]
Cement	CEM I 52.5 R	7260
Water	-	2541
Sand	Silica sand 0/2	4864
Superplasticizer	Polycarboxylate ether	14
Fiber	Glass AR 12 mm length	294

2.4.2.2 Experimental layout

An ultrasonic through-transmission setup was selected due to its penetration capability and accuracy for velocity and attenuation estimation [6, 16–18]. The transducers used for transmission and reception were K1SC (General Electric). Both are broadband transducers with a bandwidth centered at 1 MHz. Universal testing machine (Instron model 3382) was used for the four point bending test. The distance between the supports was 295 mm for the passive supports and 98 mm for the active ones. The displacement of the actuator was constant during the test (0.6 mm/min). The transmitter transducer was excited directly by a programmable signal generator (Agilent 33120A).

In order to do a broadband analysis, the transmitted signal was a swept-frequency signal (chirp). The use of chirp signals enables estimating any parameter in a wide frequency range with a single measurement by applying the proper signal processing. The mathematical expression of the transmitted linear chirp signal is

$$s_{tx}(t) = A_{tx} cos\left(2\pi f_0 t + \pi \Delta_{f_{max}} t^2\right) rect\left(\frac{t - \frac{T_w}{2}}{T_w}\right) \tag{2.4.1}$$

$$\Delta_{f_{max}} = \frac{f_{max} - f_0}{T_w} \tag{2.4.2}$$

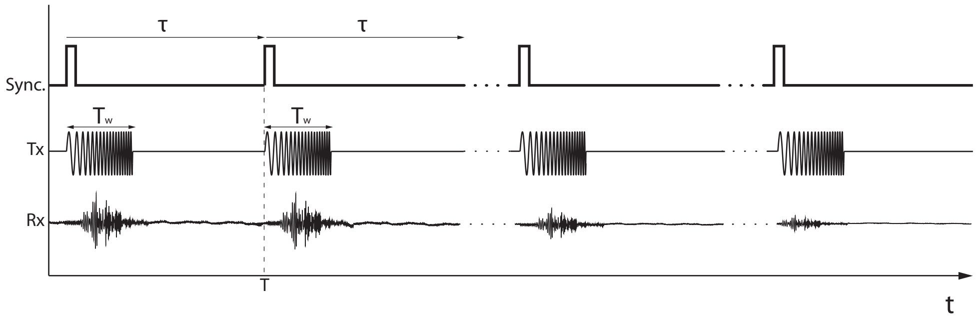

Figure 2.4.1: Time line of the test where three signals are represented: A synchronization signal between events (Sync.), and the transmitted (Tx) and received (Rx) signals, as well as some of the variables used in the mathematical analysis (τ, T and T_w).

where A_{tx} is the amplitude of the signal, f_0 is the fundamental frequency, $rect(\cdot)$ is the rectangular function, T_w is the active time of the signal, and $\Delta_{f_{max}}$ controls the maximum frequency ($f_{max} = f_0 + T_w\Delta_{f_{max}}$) which is reached at T_w seconds (Eq. 2.4.2). The selected parameters for the transmitted chirp signal are $A_{tx} = 10$ V, $T_w = 10$ μs and the frequency range varies from 200 to 1000 kHz. The experiment was monitored by injecting chirp signals with a period (T) equal to 0.5 seconds. Figure 2.4.1 shows a time line of the test, where three signals are represented: a signal of synchronization between events (Sync.), the transmitted (Tx) and received (Rx) signals, as well as some of the variables used in the mathematical analysis.

The reception transducer was connected to a linear 40 dB preamplifier (Panametrics 5600B). The received and amplified ultrasonic signal was captured by a digital oscilloscope (Tektronix DPO3014) with a sampling frequency of 25 MHz. Finally, a laptop was used to control the signal generator and to store the digitized signals.

The experimental layout of the mechanical test is shown in Figure 2.4.2. The plate rests on the passive supports and four metallic angles were attached to the plate in the positions shown. These elements serve to hold the elastic bands which keep constant the pressure between the faces of the transducers and the specimen. A similar system was presented in [19], yielding consistent results and suitable performance, where the rubber bands kept the appropriate pressure between the transducers and specimen. Pure vaseline was used to ensure an appropriate coupling between the transducers and the faces of the specimen.

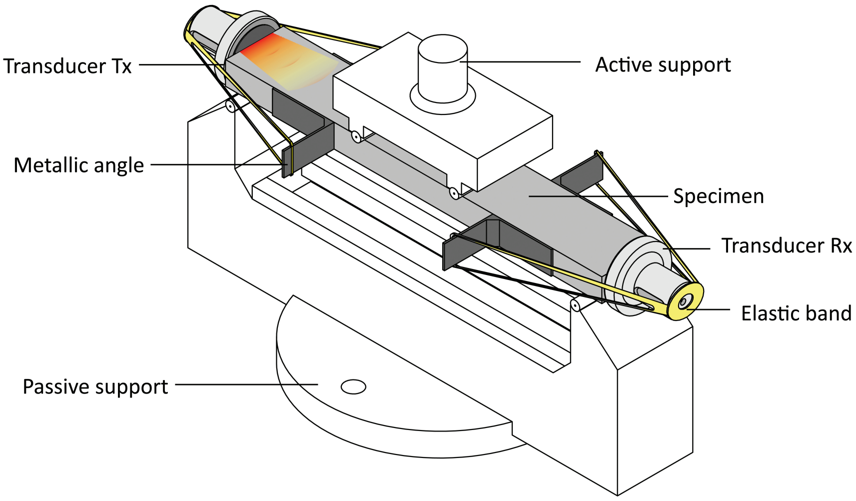

Figure 2.4.2: Experimental layout used in the ultrasonically monitored bending test. Four metallic angles are attached to the sides of the plate to support the elastic bands that keep constant the pressure between the faces of the transducers and the specimen.

2.4.2.3 Ultrasonic parameters

Using broadband signals in the analysis allows computing some ultrasound parameters which not only vary in the time domain (during the test) but also in the frequency domain. In order to support the previous results, only the time dependent parameters are also analysed. In the following, the analysed ultrasonic parameters are classified into two groups: parameters dependent on the time alone, and parameters dependent on both time and frequency.

Time dependent parameters

Many parameters were extracted from the received signals, giving information about the material for every instant of time. Let $x_{t,rx}$ be the amplitude of the received signal at time t, and let τ be the time variable in the interval from 0 to T seconds (Fig. 2.4.1). The propagation velocity, $v_p(t)$, is obtained as the ratio between the length of the specimen, d_{mat}, and the time of arrival of the signal, $\tau_{t,a}$ (Eq. 2.4.3), which was estimated as the point in time when $x_{t,rx}$ exceeds 50% of the noise level.

$$v_p(t)[m/s] = \frac{d_{mat}}{\tau_{t,a}} \tag{2.4.3}$$

The total received energy, $E_{tot}(t)$, is the energy of the received signal acquired by the oscilloscope, obtained as in Eq. 2.4.4.

$$E_{tot}(t)\ [\mathrm{J}] = \int_0^T x_{t,rx}^2(\tau)d\tau \tag{2.4.4}$$

The total attenuation of the material, $\alpha_{tot}(t)$, is obtained using Eq. 2.4.5. Given the analytical expression and the specific parameters of the transmitted signal (Eq. 2.4.1), the transmitted energy E_{tx} can be theoretically obtained using Eq. 2.4.6. In this paper, E_{tx} equals 0.5 mJ Meanwhile, $E_{rx}(t)$ is obtained from Eq. 2.4.4. The global attenuation associated to the measurement equipment (transducers, amplifier, wires, acquisition module,...), α_{equip}, is independent of the tested material and also constant throughout the test. In this paper, $\alpha_{equip} = -5$dB. The value of the preamplifier must also be subtracted ($\alpha_{preamp} = 40$ dB).

$$\alpha_{tot}(t)\ [\mathrm{dB/cm}] = \frac{E_{tx} - E_{rx}(t) - \alpha_{equip} - \alpha_{preamp}}{d_{mat}} \tag{2.4.5}$$

$$\begin{gathered} E_{tx}\ [J] = \int_0^{T_w} s_{tx}(\tau)d\tau = \frac{A_{tx}^2 T_w}{2} + \frac{A_{tx}^2}{2} \\ \int_0^{T_w} cos(2\pi(2f_0)\tau + \pi(2\Delta f_{max})\tau^2)d\tau \approx \frac{A_{tx}^2 T_w}{2} \end{gathered} \tag{2.4.6}$$

The main advantage of the attenuation versus the total energy is that it is normalized by the input energy and the distance travelled through the material. That allows comparing the attenuation between different materials and experiments.

Time and frequency dependent parameters

The characteristic attenuation of the material can not only be analysed globally, $\alpha_{tot}(t)$, but also in terms of the attenuation introduced in each frequency band. This two-dimensional variable depends on the analysis time and the frequency, $\alpha_{mat}(t,f)$. In this case, the attenuation can be modelled by Eq. 2.4.7 [14].

$$\alpha_{mat}(t,f) = \frac{10log\left(S_{tx}(t,f)\right) - 10log\left(S_{rx}(t,f)\right) - \alpha'_{equip}(f) - \alpha_{preamp}}{d_{mat}} \tag{2.4.7}$$

where $S_{tx}(t,f)$ is the energy spectral density (ESD)[†] of the transmitted signal at time t, $S_{rx}(t,f)$ is that of the received signal, d_{mat} is the distance of the specimen, and $\alpha'_{equip}(f)$ is the attenuation due to the measurement equipment. Note that $\alpha'_{equip}(f)$ is equivalent to α_{equip} in Eq. 2.4.5 when decomposed by frequency bands. This analysis considers the frequency response of the equipment used in the experiment. For further details about the calibration process and the computation of the ESD of a chirp signal, see [14] (Section 2.3).

The appearance of micro-cracks in the tested material leads to a non-linear effect known as Contact Acoustic Non-linearity (CAN) [19, 20]. This non-linear effect can be measured in terms of the variation of the amplitude of the higher harmonics. $\beta_3(t,f)$ is defined by Eq. 2.4.8 as the ratio between the amplitude of the third harmonic ($X_{rx}(t,3f)$) and the fundamental harmonic ($X_{rx}(t,f)$). The ratio between this parameter and the non-linear parameter before beginning the loading (t=0) will be denoted by $\beta_3^{\%}(t,f)$, as in Eq. 2.4.9.

$$\beta_3(t,f) = \frac{|X_{rx}(t,3f)|}{|X_{rx}(t,f)|^3} \tag{2.4.8}$$

$$\beta_3^{\%}(t,f) = 100\frac{\beta_3(t,f)}{\beta_3(0,f)} \tag{2.4.9}$$

In order to follow the same scheme as in previous papers [13] (Section 2.2), this parameter has also been analysed for a fixed working frequency, thus obtaining an index that depends only on the time. In the present paper, the chosen fixed frequency is 363 kHz since the third harmonic appears in the center of the transducer band (≈ 1 MHz), being more sensitive to its location in the spectrum. This parameter, in the following denoted by $\beta_3(t,363)$, complements the time dependent parameter analysis presented in the previous subsection.

A common way to display results depending on these two independent variables is a time–frequency diagram. In these graphs, the x-axis corresponds to the time, the left y-axis indicates the stress/strain curve, the right y-axis is the frequency range, and the color axis represents the intensity of the analysed parameters, $\alpha_{mat}(t,f)$ and $\beta_3(t,f)$.

2.4.3 Results and discussion

In the first instance, due to the fact that the stress–strain curves are different and the characteristic events of the test occur at different time instants (depending

---

[†] The energy spectral density, $S(f)$, of a finite time signal, $x(t)$, is defined as $S(f) = |X(f)|^2$, where $X(f) = \int_{\tau_0}^{\tau_1} x(\tau)e^{-i2\pi f\tau}d\tau$ is the Fourier Transform of $x(t)$.

on the specimen), no statistical values were extracted (mean, standard deviation, confidence intervals...) and a single plate was selected to follow the discussion and make it clear and understandable. The rest of the plots have been located in Section Figures, which shows the reproducibility and consistency of the results. Moreover, no corrections were made to the mechanical curves, in order not to disrupt the correlation between the mechanical and ultrasonic parameters.

In this section, the ultrasonic parameters and stress–strain curves were correlated. Firstly, the time dependent parameters, $v_p(t)$, $E_{tot}(t)$, $\alpha_{tot}(t)$, and $\beta_3^{\%}(t, 363)$, are represented and analysed (subsection 2.4.3.1 and Fig. 2.4.3). Then, the time and frequency dependent parameters, $\alpha_{mat}(t, f)$ and $\beta_{3f}^{\%}(t, f)$, are described in subsection 2.4.3.2.

2.4.3.1 Time dependant parameters

The results for the time dependent parameters are plotted in Figure 2.4.3 using a double y-axis with the corresponding absolute values of each parameter.

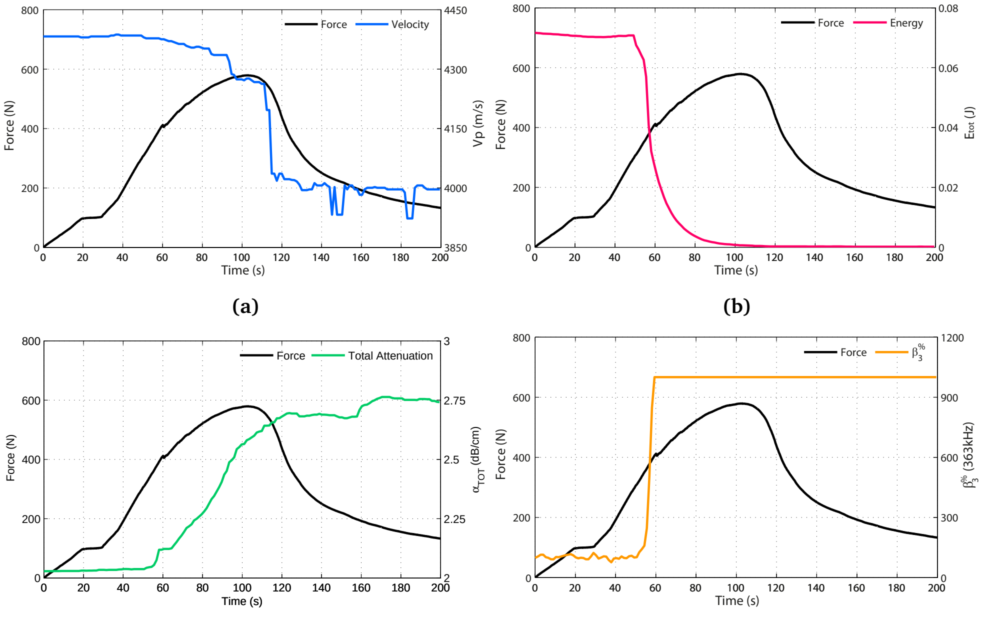

(a) **(b)** **(c)** **(d)**

Figure 2.4.3: Comparison between absolute values of time dependent ultrasonic parameters and stress–strain curve of one specimen: (a) velocity of the chirp signal, (b) energy of the received signal, (c) total attenuation and (d) non-linear parameter $\beta_3^{\%}$ measured at 363 KHz.

Figure 2.4.3a shows the evolution of the velocity of the chirp signal during the test. The velocity parameter, $v_p(t)$, stays constant in the initial stage of the test (supports and specimen's surface coupling stabilization) and for most of the elastic step of the stress–strain curve (0–50 s). When the first micro-cracks begin to appear (50–60 s), $v_p(t)$ decays slightly ($\approx$ 10 m/s), and after that, goes down to values around 4000 m/s and becomes unstable due to the low signal-to-noise ratio (SNR) (failure when estimating $\tau_{t,a}$).

Figure 2.4.3b shows the trend of energy of the received wave. Three zones can be clearly identified in the evolution of $E_{tot}(t)$. In the first zone (0–50 s), the parameter stays constant while the specimen deforms. In the second zone (55–100 s), the $E(t)$ curve starts to decay to values close to zero before the cracking process starts (60 s) due to the micro-cracking process previous to the first large crack. After that (100–end of the test), $E(t)$ stays at zero values because the section of the plate is getting progressively smaller.

The attenuation of the material, $\alpha_{tot}(t)$, is plotted in Figure 2.4.3c. There is a trend opposite to that obtained for the previous parameters. In the first zone, $\alpha_{tot}(t)$ stays constant (close to 2 dB/cm), however, before the appearance of the first crack (55 s), it rises to high values (2.7 dB/cm) and stays constant until the end of the test.

As mentioned in Section 2.4.2, $\beta_3^{\%}(t, 363)$ was monitored because it is very sensitive to crack formation. In order to calculate $\beta_3^{\%}(t)$ it is necessary to fix a discrete frequency since the emitted signal contains information on several frequencies. The specific frequency 363 kHz was used to analyse the generation of high-frequency harmonics because the third harmonic appears in the center of the transducer's band ($\approx$ 1 MHz), being more sensitive to its location in the spectrum. Figure 2.4.3d shows the evolution of $\beta_3^{\%}(t)$ as the test progresses. It can be noticed that this parameter dramatically increases (a variation of 1000%) in the critical zone, after the beginning of the cracking process of the plate ($\approx$ 55 s). The fact that $\beta_3^{\%}(t)$ changes quickly in the beginning of the cracking process indicates premature damage in the specimen (in the elastic step of the stress–strain curve) warning of the damage that the specimen has already suffered.

In order to compare the time dependent parameters, their normalized values were calculated (Fig. 2.4.4). As can be observed, $v_p(t)$ does not show relevant information in the stage previous to the first cracks, showing a slow detection of the damage suffered by the plate. However, $E_{tot}(t)$ and $\alpha_{tot}(t)$ are more sensitive, showing significant variations previous to the plastic step of the stress–strain curve. Significantly, $\beta_3^{\%}(t, 363)$ exhibits an interesting behaviour, marking perfectly the instant when the specimen begins to suffer initial damage. This means that the

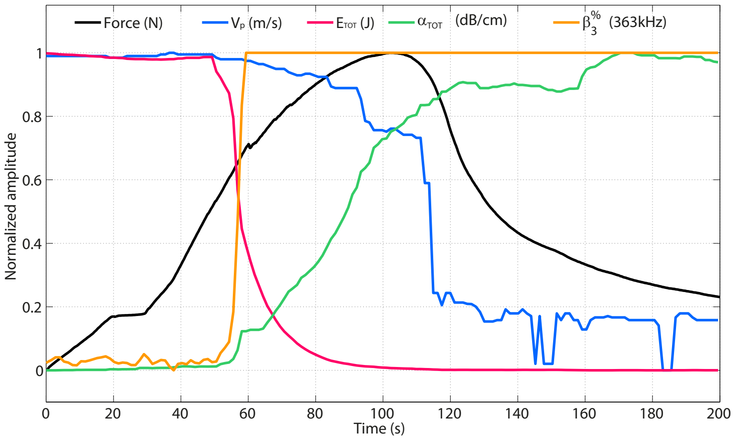

Figure 2.4.4: Comparison of the normalized values of the time dependent ultrasonic parameters and the stress–strain curve of one GRC specimen.

non-linear parameter is the most sensitive way to identify the change from the elastic to plastic zone in GRC.

2.4.3.2 Time and frequency dependent parameters

The results for the parameters depending on both the time and the frequency are shown in Figs. 2.4.5 and 2.4.6. The x-axis indicates the test time, the left y-axis the force (stress–strain curve) and the right y-axis the analysed frequency range. The parameter under study is shown with different colours and its respective gradients.

Figure 2.4.5a shows the evolution of $\alpha_{mat}(t,f)$ as the bending test progresses. In the first instance and for a fixed value of t, the attenuation parameter rises with the increase of the analysed frequency, as suggested in most of the literature and in previous papers [6, 13, 18]. For each frequency, this means, for a fixed frequency f, the parameter of attenuation also rises along the experiment. A similar trend can be observed in Figure 2.4.3c for $\alpha_{tot}(t)$, which only depends on the test time. By means of analysing $\alpha_{mat}(t,f)$, there can be obtained the complete material response to different injected frequencies along the experiment time. The attenuation remains constant during the stabilization stage (0–30 s) and for most of the elastic step (30–60 s). Near the first crack, at the end of the elastic step (50–55 s), the attenuation patterns change and it starts to rise to higher values due the initial phase of the micro-cracking process. Once the plate is in the plastic stage (65–90 s), the attenuation for frequencies under 600 kHz rises. Slightly before the maximum stress point ($\approx$ 90 s) the attenuation for higher frequencies (over 600 kHz) also increases, to reach its maximum attenuation value. From the maximum stress point (≈ 110 s) on, the attenuation patterns keep constant until the end of the test, where the effective cross section of the plate is low. The time–frequency diagrams for the rest of the tested plates are shown in Section Figures.

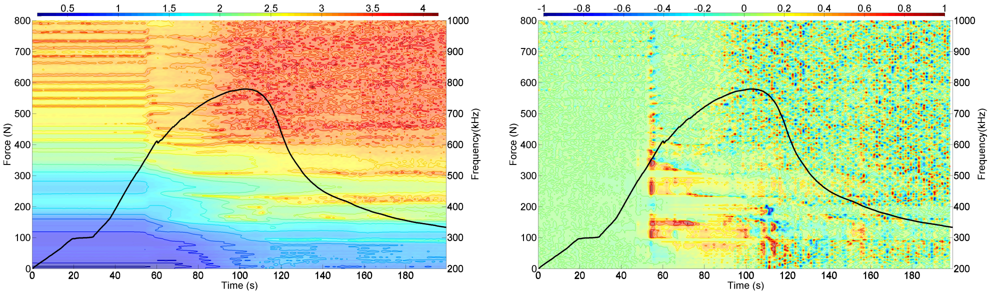

(a) **(b)**

Figure 2.4.5: Time–frequency diagrams of the parameters related to the attenuation. The x-axis indicates the test time, the left y-axis the force (stress–strain curve) and the right y-axis the analysed frequency range. The parameter under study is shown with different colours and its respective gradients. a) Time–frequency diagram of the $\alpha_{mat}(t,f)[dB/cm]$. b) Time–frequency diagram of the normalized $\Delta_t \alpha_{mat}(t,f)$.

The interest of this study lies in finding and highlighting the changes in the ultrasonic parameters with the progress of the bending test and in correlating these changes with the events produced in the specimen. As has been observed, $\alpha_{mat}(t,f)$ seems to be sensitive to any change in the mechanical properties of the material under study. Nonetheless, the representation of the absolute values of $\alpha_{mat}(t,f)$ may hide some notable changes. Thus, a further analysis of the attenuation, considering the sensitivity of each frequency, is proposed. Figure 2.4.5b plots the variation of the attenuation with respect to time, normalized over the maximum value for each frequency, $\Delta_t \alpha_{mat}(t,f)$. This graph allows identifying the main events happening during the bending test: the first crack (≈ 55 s) and the maximum stress point of the specimen (≈ 110), even by a certain time in advance of the mechanical curve. Note that this normalized representation allows comparing the attenuation levels regardless of the working frequency. Changes in $\Delta_t \alpha_{mat}(t,f)$ for the first crack are observed for all studied frequencies, although frequencies under 600 kHz are more sensitive. Additionally, for the maximum stress point, the most sensitive frequencies are lower than 400 kHz. In Section Figures, time–frequency diagrams for the rest of the tested plates are shown. As can be observed, those attenuation results present similar patterns by overcoming the differences between specimens and experiences.

Figure 2.4.6 shows the corresponding graph for $\beta_3^{\%}(t,f)$. As could be observed in the previous figures (Fig. 2.4.3d), $\beta_3^{\%}(t,363)$ was very sensitive to the crack formation, varying its value drastically when the specimen is damaged by the formation of the first crack. In this figure, this behaviour can be seen for all frequencies contained in the frequency range chosen according to the location of the third harmonic and the transducer response as mentioned before (300–500 kHz). This non-linear parameter remains constant during the stabilization stage for all frequencies, as do the rest of the ultrasonic parameters.

When the stress–strain curve approaches the cracking zone, $\beta_3^{\%}(t,f)$ increases rapidly for several frequencies, reaching higher values before the cracks promoted by the deformation of the specimen appear. Since each stress–strain curve is unique, each time–frequency diagram varies (see Section Figures), depending on the specimen but always following the same pattern (a rapid increase before the beginning of the plastic step).

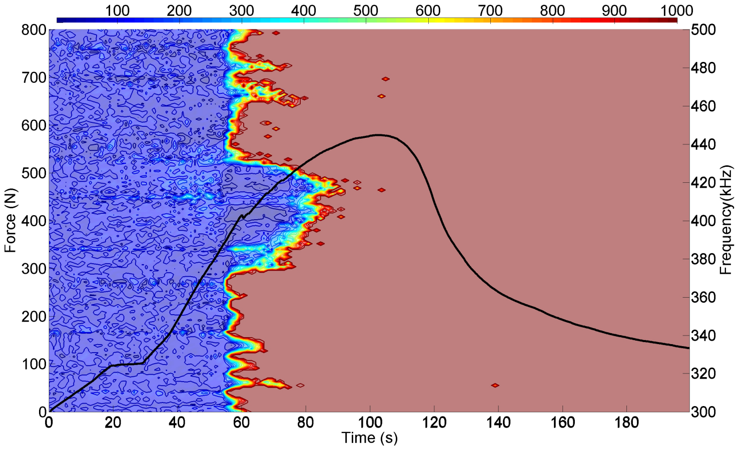

Figure 2.4.6: Time–frequency diagram of the non-linear parameter $\beta_3^{\%}(t,f)$. The x-axis indicates the test time, the left y-axis the force (stress–strain curve) and the right y-axis the analysed frequency range. The parameter under study is shown with different colours and its respective gradients.

Regarding the obtained results, it can be concluded that the attenuation time–frequency diagram gives information about the continuous changes between the different steps of the test. However, the non-linear parameter seems to be the best for an analysis that will robustly characterize the cracking instant.

The sensitivity to inhomogeneities (pores, cracks...) of each frequency depends not only on the dimension of the discontinuity but also the direction, disposition, separation between faces, etc. For this reason, it is very important to have the proposed $\alpha_{mat}(t,f)$ and $\beta_{3f}^{\%}(t,f)$ time–frequency diagrams to accurately detect when the element under test is being critically damaged.

2.4.4 Conclusions

In this paper, a complete ultrasonic monitoring of GRC plates under bending tests was addressed. A recently proposed procedure based on broadband signals (chirp) was used in order to measure different ultrasonic parameters in a wide range of frequencies. This new method of monitoring bending tests provides a wealth of information about the material behaviour in terms of the attenuation, energy, velocity, and generation of non-linear harmonics in the signal. In order to support the previous results and provide new information, the analysis has been divided into two parts: those parameters dependant only on time, and those dependent on both time and frequency. In the first group, the evolution of the velocity roughly characterizes the main two events happening during the test: the first large crack and the maximum stress point. However, the energy and attenuation of the chirp signal were more sensitive, showing a significant variation previous to the plastic step of the stress–strain curve, attenuation being more appropriate for comparing different materials and tests. It was conspicuous that the non-linearity in the generation of high harmonics exhibited an interesting behaviour, marking perfectly the instant when the specimen was suffering damage. In the second part, the attenuation and non-linearity were analysed in terms of time and frequency, giving more information about the material properties during the progress of the test. The study of this variation of the attenuation along time for each fixed frequency has been proposed. This new normalized approach has allowed comparing the trends between different working frequencies, as well as significantly detecting both the first large crack and the maximum stress point. The non-linearity had a sudden change as the micro-cracking began, pointing perfectly to the time instant when the specimen is being critically damaged.

This paper has demonstrated the suitability of ultrasonic broadband signals to characterize fiber-reinforced cementitious composites under bending stress since it allows simultaneously analysing some of the traditional ultrasonic parameters in the frequency domain. This approach might open up a new line of research in any further application where the acquisition time is a critical variable.

Figures

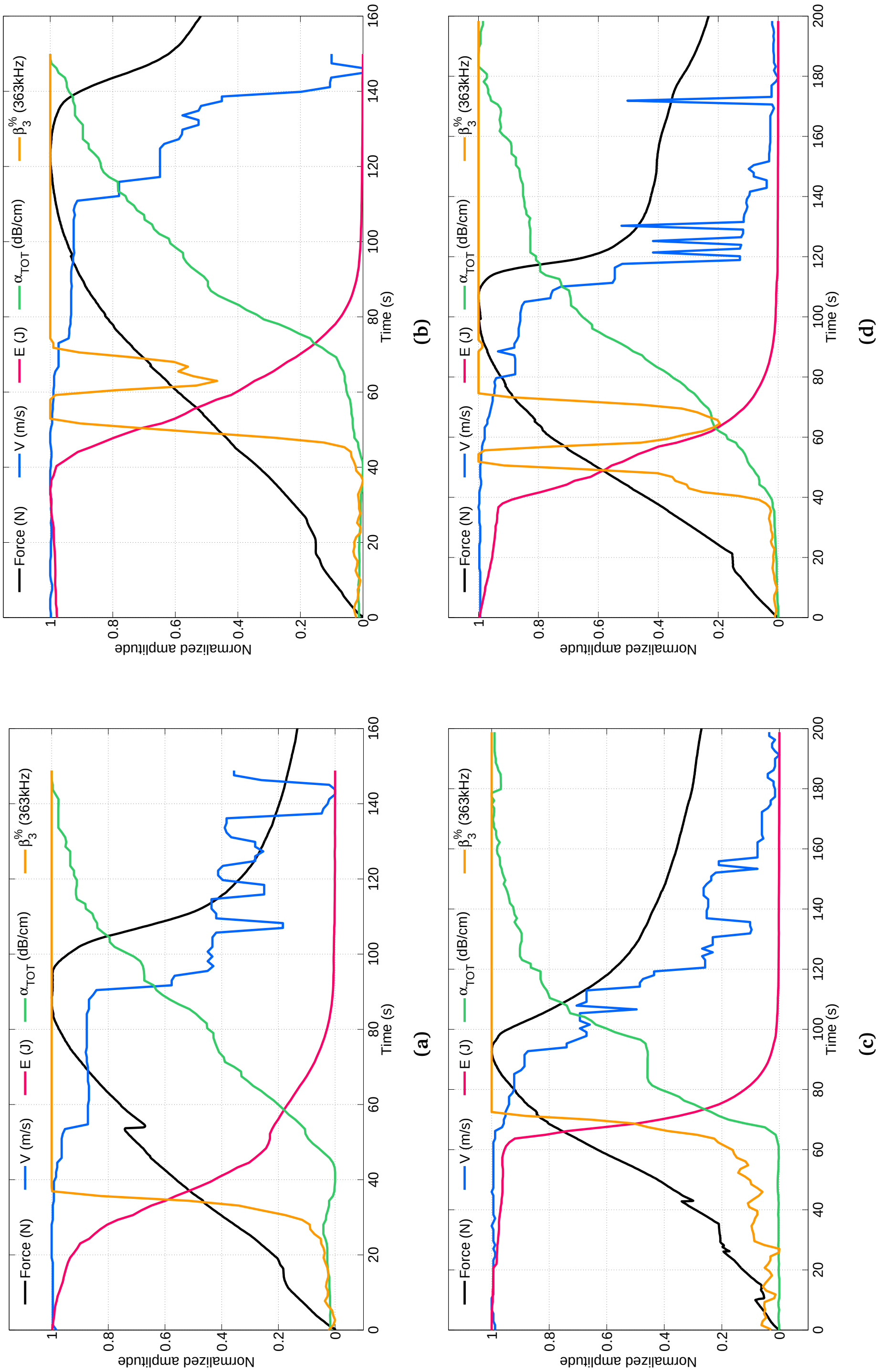

(a)

(b)

(c)

(d)

Figure 2.4.7: Normalized time-dependent parameters for the rest of the tested specimens.

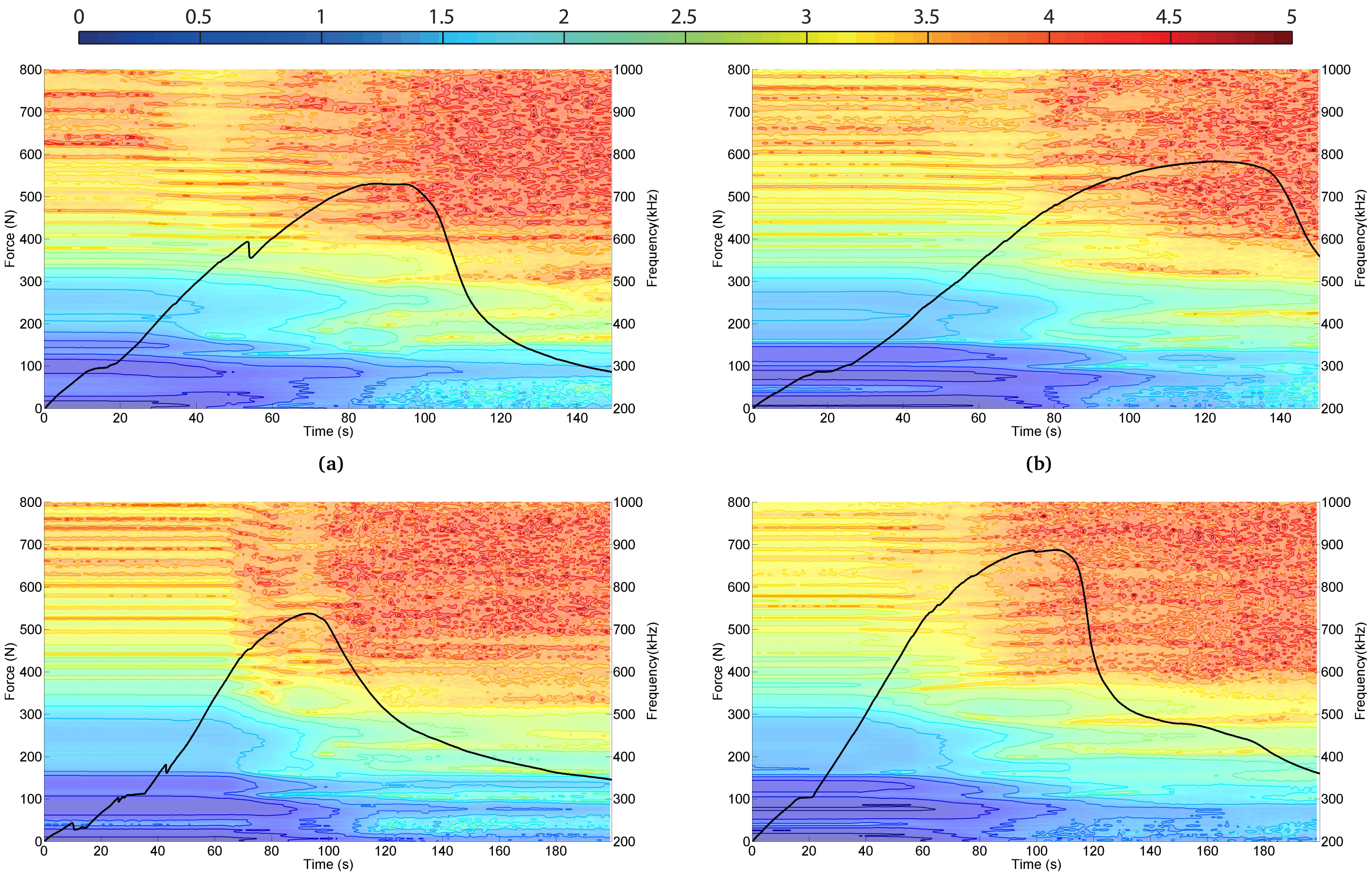

(a) (b)

(c) (d)

Figure 2.4.8: Time–frequency diagrams of the attenuation, $\alpha_{mat}(t, f)$. The x-axis indicates the time, the left y-axis the force (stress–strain curve), and the right y-axis the analysed frequency range. The parameter under study is shown with different colours and its respective gradients for the rest of the analyzed probes.

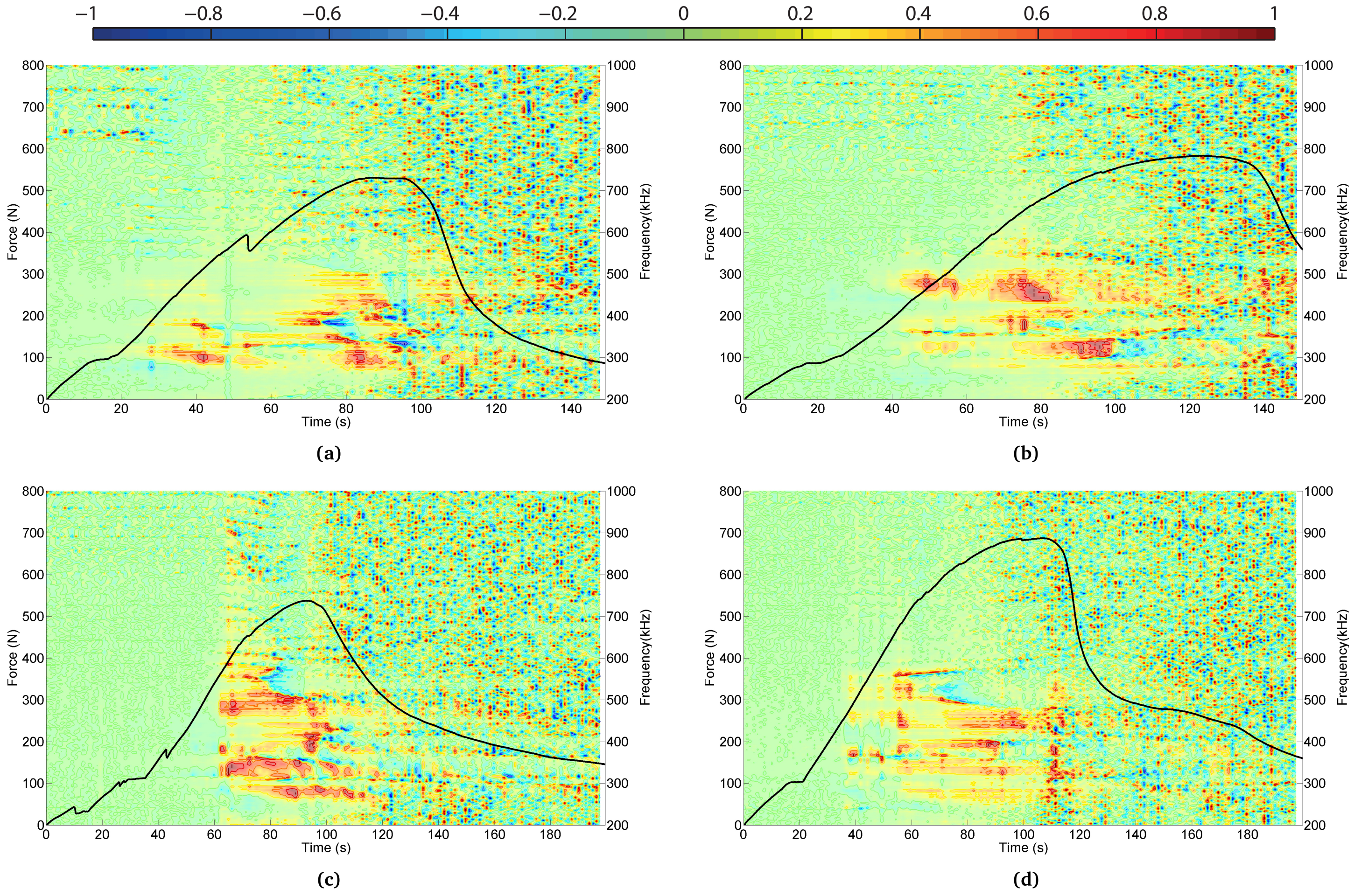

(a) (b) (c) (d)

Figure 2.4.9: Time–frequency diagrams of variation of the attenuation, $\Delta_t \alpha_{mat}(t,f)$. The x-axis indicates the time, the left y-axis the force (stress–strain curve), and the right y-axis the analysed frequency range. The parameter under study is shown with different colours and its respective gradients for the rest of the analyzed probes.

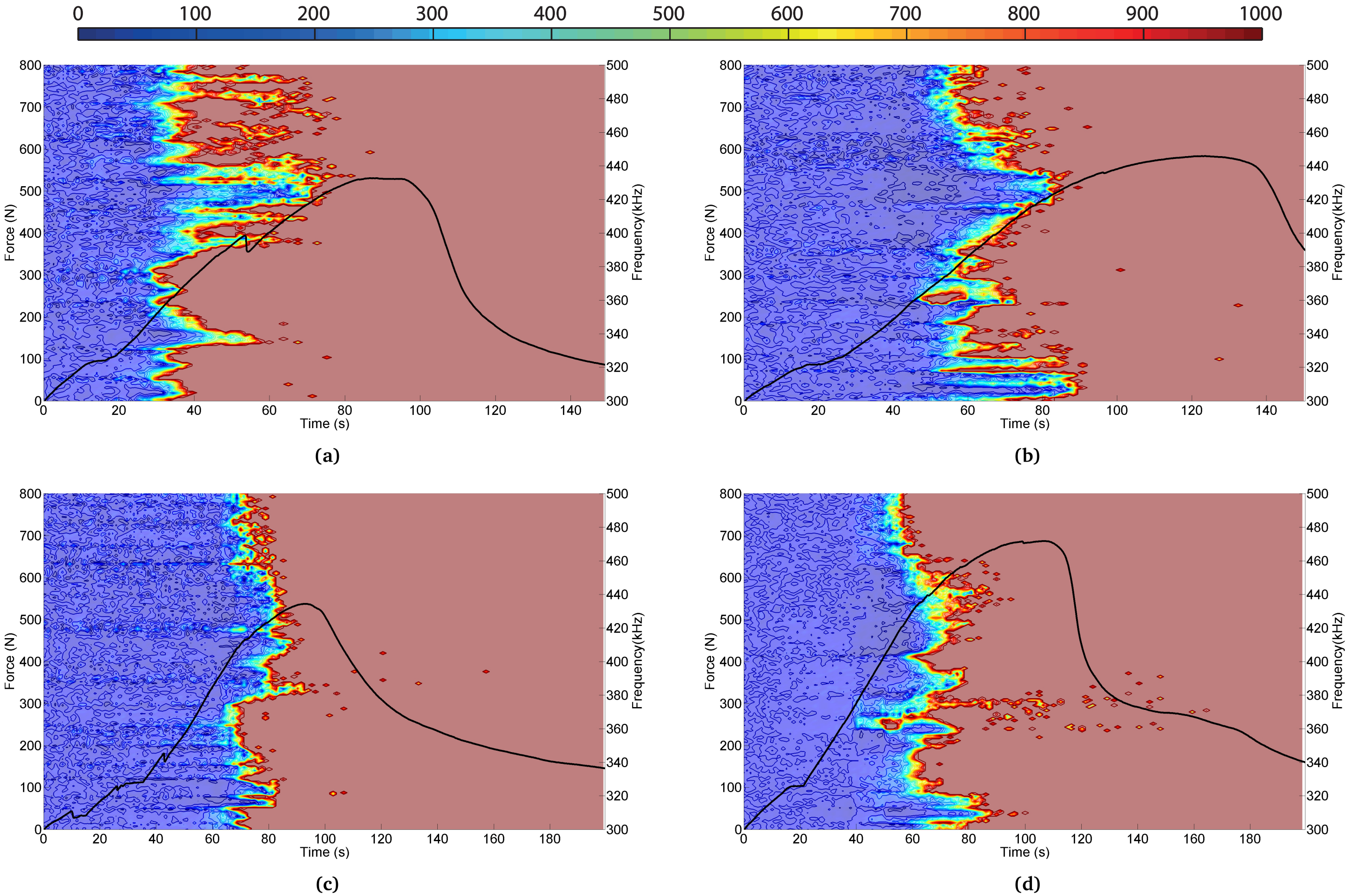

(a)

(b)

(c)

(d)

Figure 2.4.10: Time–frequency diagrams of non-linear parameter, $\beta_3^{\%}(t,f)$. The x-axis indicates the time, the left y-axis the force (stress–strain curve), and the right y-axis the analysed frequency range. The parameter under study is shown with different colours and its respective gradients for the rest of the analyzed probes.

References

[1] A. J. Majumdar, J. Ryder, and B. R. Station, *Glass fibre reinforcement of cement products*. Garston, England: Building Research Station, 1968.

[2] A. Bentur, *Fibre reinforced cementitious composites*. Taylor & Francis, 1990.

[3] V. M. Maholtra and N. J. Carino, Eds., *Handbook on Non destructive Testing on Concrete*. CRC Press, 2004, vol. 1.

[4] J. A. Bogas, M. G. Gomes, and A. Gomes, "Compressive strength evaluation of structural lightweight concrete by non-destructive ultrasonic pulse velocity method," *Ultrasonics*, vol. 53, no. 5, pp. 962–972, 2013.

[5] A. Jain, A. Kathuria, A. Kumar, Y. Verma, and K. Murari, "Combined use of non-destructive tests for assessment of strength of concrete in structure," *Procedia Engineering*, vol. 54, pp. 241–251, 2013.

[6] T. P. Philippidis and D. G. Aggelis, "Experimental study of wave dispersion and attenuation in concrete," *Ultrasonics*, vol. 43, no. 7, pp. 584–595, 2005.

[7] S. Popovics, J. L. Rose, and J. S. Popovics, "The behaviour of ultrasonic pulses in concrete," *Cement and Concrete Research*, vol. 20, no. 2, pp. 259–270, 1990.

[8] L. Vergara, J. Gosálbez, J. V. Fuente, R. Miralles, and I. Bosch, "Measurement of cement porosity by centroid frequency profiles of ultrasonic grain noise," *Signal Processing*, vol. 84, no. 12, pp. 2315–2324, 2004.

[9] L. Vergara, R. Miralles, J. Gosálbez, F. J. Juanes, L. G. Ullate, J. J. Anaya, M. G. Hernández, and M. A. G. Izquierdo, "NDE ultrasonic methods to characterise the porosity of mortar," *NDT & E International*, vol. 34, no. 8, pp. 557–562, 2001.

[10] D. G. Aggelis and T. P. Philippidis, "Ultrasonic wave dispersion and attenuation in fresh mortar," *NDT & E International*, vol. 37, no. 8, pp. 617–631, 2004.

[11] F. Moradi-Marani, P. Rivard, C. Lamarche, and S. Kodjo, "Evaluating the damage in reinforced concrete slabs under bending test with the energy of ultrasonic waves," *Construction and Building Materials*, vol. 73, pp. 663–673, 2014.

[12] H. Ogi, T. Hamaguchi, and M. Hirao, "In-situ monitoring of ultrasonic attenuation during rotating bending fatigue of carbon steel with electromagnetic acoustic resonance," *Journal of Alloys and Compounds*, vol. 310, no. 1-2, pp. 436–439, 2000.

[13] V. Genovés, J. Gosálbez, R. Miralles, L. Soriano, and J. Payá, "Ultrasonic monitoring on glass fiber reinforced cement (GRC) bending test," *Materials Characterization*, vol. 90, pp. 149–158, 2015.

[14] V. Genovés, J. Gosálbez, A. Carrión, R. Miralles, and J. Payá, "Optimized ultrasonic attenuation measures for non-homogeneous materials," *Ultrasonics*, vol. 65, pp. 345–352, 2016.

[15] B. Standard, *Precast concrete products - Test method for glass-fibre reinforced cement - Part 5. Measuring bending strength, 'Complete bending test' method.* 1998.

[16] J. Krautkrämer and H. Krautkrämer, *Ultrasonic testing of materials*. Springer-Verlag, 1983.

[17] P. A. Gaydecki and F. M. Burdekin, "The propagation and attenuation of medium-frequency ultrasonic waves in concrete: a signal analytical approach," *Measurement Science and Technology*, vol. 3, p. 126, 1992.

[18] M. Molero, I. Segura, S. Aparicio, M. G. Hernández, and M. A. G. Izquierdo, "On the measurement of frequency-dependent ultrasonic attenuation in strongly heterogeneous materials," *Ultrasonics*, vol. 50, no. 8, pp. 824–828, 2010.

[19] A. Shah and Y. Ribakov, "Non-linear ultrasonic evaluation of damaged concrete based on higher order harmonic generation," *Materials & Design*, vol. 30, no. 10, pp. 4095–4102, 2009.

[20] A. Shah and Y. Ribakov, "Non-destructive evaluation of concrete in damaged and undamaged states," *Materials & Design*, vol. 30, no. 9, pp. 3504–3511, 2009.

Chapter 3

Non-linear acoustic spectroscopy: Cases on chemical and thermal damages in mortar

Linear and non-linear reverberation parameters are used in this chapter to monitor chemical and thermal damaging mechanisms. The set of Non-linear Elastic Waves (NEWS) techniques is a hotspot in science communities at this moment due to its sensitivity to cracks in a non-homogeneous medium. The lack of information about how dynamic anomalies interact with each other in a heterogeneous media is also an important point to consider and investigate. The purpose of this chapter is to detect and monitor different kinds of damage but also to understand the underlying phenomenon of non-linear reverberation and to contribute with a new technique that extracts non-linear parameters from a single excitation event respect to classical multiple excitation events (NIRAS).

In the first section a multimodal analysis of GRC samples under an ageing damaging process was carried out. The purpose of this study was to analyse the evolution of the mechanical performance of GRC using a non-linear impact technique. In addition, a comparison among the different resonant modes was carried out in terms of linear and non-linear parameters (Section 3.1). In the second section, an exhaustive internal sulphate attack in mortar was monitored. In this case, linear reverberation and ultrasonic parameters were used to follow the expansion behaviour of mortar samples with different degrees of damage. The usage of broadband signals to extract attenuation parameters in a wide range of frequencies gave an interesting overview of the expansion mechanism (Section 3.2). In the Section 3.4 a complete thermal damage study was addressed. Two main mechanisms of damage coexist in the same situation. Parameters related with the stiffness of the material revealed important information about the main changes in the cement matrix. Nevertheless, contact and interface changes in the material were perfectly captured by attenuation and non-linear ones (Section 3.3). A new algorithm to extract non-linear parameters from one single impact event was developed and compared with the traditional one. This new procedure uses an accumulating windowing system instead of the traditional sliding window of the Short Fast Fourier Transform. The new algorithm was tested on mortar subjected to thermal damage in order to have different levels of non-linearity in the analysed samples (Section 3.4).

Different NDT parameters has been analysed in the described sections of this chapter. The scope was to contribute with a new procedure to extract non-linear information from non-homogeneous materials and to try to understand the effect on the different layouts, geometry and types of damage. Moreover, the analysis of a complex damage mechanism taught us that the correct way to analyse these spoiling processes is to examine both linear and non-linear parameters.

3.1 Multimodal analysis of GRC ageing process using Non-linear Impact Resonance Acoustic Spectroscopy[5]

[5] *V. Genovés, C. Riestra, M.V. Borrachero, J. Eiras, T. Kundu, and J. Payá. "Multimodal analysis of GRC ageing process using Non-linear Impact Resonance Acoustic Spectroscopy," Composites Part B: Engineering, vol. 76, pp. 105–111, 2015.*

Abstract

Glass-fiber Reinforced Cement (GRC) is a composite material composed of Portland cement mortar with low w/c (water/cement) ratio and high proportion of glass-fibers. This material suffers from the ageing process by losing its strength with time because of its exposure to severe weather conditions. Ageing process damages the fibre surface and decreases the mechanical properties of the structural components made of this material. It reduces the elastic modulus and toughness of GRC. Fracture toughness is traditionally measured by four point bending tests. In a previous study by the authors it was observed that ageing related deterioration or damage of GRC could be monitored by Non-Destructive Testing (NDT) techniques such as Non-linear Impact Resonance Acoustic Spectroscopy (NIRAS) and other ultrasonic techniques. The scope of this paper is to corroborate previous investigations and offer early damage detection capability by generating more experimental data points by optimizing location of the point of strike and thus generating more resonance vibration modes in NIRAS tests.

3.1.1 Introduction

Glass-fibre reinforce cement (GRC) is a composite material formed with Portland cement mortar with glass-fibre inclusion. The matrix of this material is made from low w/c (water/cement) ratio and high paste proportion relative to the aggregate quantity. Adding a high proportion of glass-fibers to the mortar matrix improves the mechanical properties of the structural components made by this material, especially, the toughness and ductility properties. This composite plays an important role in construction of some concrete structures such as sheets, panels and other slim shapes used usually in building engineering and architecture where steel-reinforced concrete cannot be used [1].

However, due to glass composition and the nature of the Portland cement matrix, a chemical reaction occurs between cement and glass provoking the deterioration of the fibres, creating holes and coating degradation followed by a toughness decrease of the composite [1–3]. For this reason researchers have been developing new less aggressive matrices that improve the performance of the fibres and enhance the durability of the GRC system. Enfedaque, Cendón, Gálvez, and Sánchez-Gálvez have suggested matrix modification with silica fume and metakaolin substitution, Purnell, Short, Page, and Majumdar studied observing the microstructure of the material using scanning electron microscopy after subjecting it to mechanical loading test [2, 4, 5].

Behaviour of a material as it ages is generally tested by first placing specimens made of this material at high temperatures and under high humidity [6] and then performing mechanical tests to obtain its stiffness, toughness and strength.

In order to improve the material characterization and damage detection methods, researchers have been developing different Non-Destructive Testing (NDT) techniques. It is known that NDT have the capability of obtaining a number of physical properties of cementitious materials such as their dynamic Young's modulus, porosity and compressive strength [7–10]. New, NDT techniques based on non-linear acoustics have been recently developed by researchers in order to detect early stage of damage in different materials [11]. Chen, Jayapalan, Kim, Kurtis, and Jacobs and Leśnicki, Kim, Kurtis, and Jacobs were using non-linear impact resonance acoustic spectroscopy (NIRAS) technique in order to detect alkali-silica reaction (ASR) damage in concrete using different types of aggregates [12, 13].

In an earlier study by the authors it was demonstrated that ageing process could be detected by acoustic resonance techniques like NIRAS more efficiently than traditional tests [14] .

The scope of this paper is to analyse the ageing process, optimizing NIRAS test method for GRC specimens to obtain more experimental data points and to evaluate the suitability of the method for monitoring ageing related degradation.

3.1.2 Experiment

3.1.2.1 Materials

GRC specimens were made according to the BS EN 1170-5 [15]. For this experiment the specimen dimension was chosen as 275 × 50 × 10 mm^3. The specimens were cut from 350 × 350 × 10 mm^3 mother plates.

Four such mother plates were fabricated. From every mother plate 7 specimens were cut, thus 28 specimens in total were prepared.

Table 3.1.1: Tests performed on different plate.

Plate	0 h	4 h	8 h	12 h	20 h	24 h	33 h	40 h	48 h	63 h	90 h
I	N/B/S	-	-	-	-	-	-	-	-	-	-
II	N		N/B	-	-	-	-	-	-	-	-
III	N	-	-	-	-	N/B	-	-	-	-	-
IV	N	N	N	N	N	N	N	N	N	N	N/B/S

N = NIRAS test, B = Bending test, S = SEM

Table 3.1.1 shows different tests performed on the four plates. NIRAS tests were performed for different extents of ageing, SEM observations were made for undamaged and totally damaged specimens in order to see the fibre degradation, and mechanical tests were performed after 0h, 8h, 24h and 90h of ageing. Table 3.1.2 shows the proportions and information about the raw materials used to fabricate the GRC plates.

Table 3.1.2: Used dosage for one GRC plate specimen.

Material	Type	Weight [g]
Cement	CEM I 52.5 R	3630
Water	-	1270.5
Sand	Silica sand 0/2	2432
Superplastizicer	Policarboxilate ether	7
Fibre	Glass AR 12 mm	147

After characterizing all specimens (from SEM, bending test and NIRAS) and identifying all resonance vibration modes the rest of the specimens were immersed in a controlled water tank at 65 °C to age them. The tests were performed at different stages of ageing as shown in Table 3.1.1.

3.1.2.2 Modal analysis

Because of the importance of identifying the vibration modes and obtain as many modes as possible with high amplitude, a modal extraction analysis was performed with a finite element method (FEM) software (ANSYS).

During the theoretical analysis study the specimen size influence was investigated considering four sizes of the plate: 225 × 50 × 10, 275 × 50 × 10, 325 × 50 × 20, 325 × 50 × 30 mm^3 geometries. Modal analysis results were used to optimize the point of impact and receiving sensor locations on the specimen in order to obtain as many modes as possible on the experimental spectrum response.

Table 3.1.3: FEM calculation parameters.

Ec [MPa]	ν	δ [kg/m^3]	Range [Hz]
28000	0.18	2300	0 - 5000

Table 3.1.3 shows values used for the FEM analysis. Mechanical properties were taken from references [16] and adjusted to match the experimental results.

3.1.2.3 NIRAS technique

NIRAS method is a relatively new NDT technique which can detect changes in materials from the resonance frequency shifts of the vibrational modes of a specimen made from this material as the impact energy increases [17]. This change is simply due to the non-linearity of the material. This technique has been shown to be highly high sensitivity to material defects, specifically to the micro-cracks of the material. It is well-known that defects in a material can be detected from the vibrational frequency resonance values of a specimen made of that material. Distributed cracks reduce the stiffness of the specimen, and therefore, the natural frequency of the structural element made of that material. Besides this linear effect ($f = \sqrt{k/m}$, where k is the stiffness and m the mass of the specimen) cracks also change non-linear properties of the material: Those cracks form imperfect matrix and non-homogeneity zones and thus creates, for instance, pores or voids, micro pores, paste-aggregate interface and other mesoscopic effects [13, 17].

This kind of imperfections trigger non-linear effects such as change of the frequency when the impact energy is increased, non-linear modulation of two waves and scalability loss. This distortion of the elastic waves is responsible for the change in the observed resonance frequency in NIRAS tests, which can be described as a non-linear hysteretic macroscopic behavior of the material itself [13].

According to the phenomenological model for hysteresis and classical non-linear constitutive relations proposed by Van Den Abeele, Johnson, and Sutin[18], the elastic modulus for a material with non-linear effects can be represented as Eq. 3.1.1:

$$E = E_0[1 + \beta\epsilon + \delta\epsilon^2 + \alpha(\Delta\epsilon + \epsilon \cdot sgn(\dot{\epsilon}))] \tag{3.1.1}$$

where E_0 is the linear elastic modulus, β and δ are the coefficients of cubic and quartic anharmonicities, $\Delta\epsilon$ is the strain amplitude variation, ϵ and $\dot{\epsilon}$ are the strain and strain rate, α is the measure of hysteresis, and $sgn(\cdot)$ is the sign function [18]. Specimens made with these materials that follow Eq. 3.1.1 change their natural vibration frequencies with the variation of the excitation energy. This non-linearity could be defined as follows (Eq. 3.1.2)

$$\frac{f_0 - f}{f_0} = \alpha\Delta\epsilon \tag{3.1.2}$$

where f_0 is the frequency for the low impact energy, f the frequency for the high impact energy, α the measure of non-linearity and ϵ the deformation suffered by the specimen. In this experiment, 10 impacts were given for every NIRAS test. After collecting ten signals with different impact energies and identifying the peaks in the frequency domain a first order polynomial was fitted to obtain the R^2 of the line as a measure of the reliability of the hysteretic parameter.

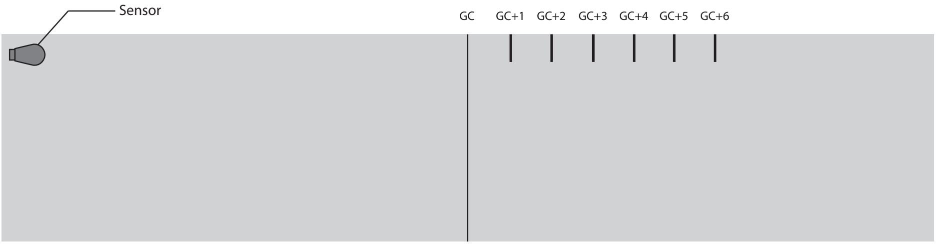

Figure 3.1.1: Point of impact layout.

3.1.2.4 Test disposition

In order to optimize the location of the hammer impact point, multiple points of the specimen were hit by the hammer and corresponding response spectra were recorded. Figure 3.1.1 shows different impact point locations on the specimen and the sensor location. Figure 3.1.2 shows the test configuration. It is composed of one hammer support attached to a rigid base and both sides of the support are linked by a metallic axis that makes the impact hammer to rotate, for hitting the specimen with different levels of impact energy. There are also two additional supports for placing the specimen in the required position when it is struck by the hammer. The specimen support frame is attached to the same rigid base where the hammer support frame is attached. The test disposition permits the specimen vibrates without constraints (a case of free vibration).

After location of the hammer strike point had been optimized, the study of ageing process with this configuration began.

3.1.3 Results and discussion

3.1.3.1 Modal analysis results

As mentioned in previous sections, modal analysis was performed to see frequency response of different specimen geometries and select the best option.

More than four geometries were simulated for the modal analysis, but only the most interesting ones are plotted in Figure 3.1.3. Colour code used in this

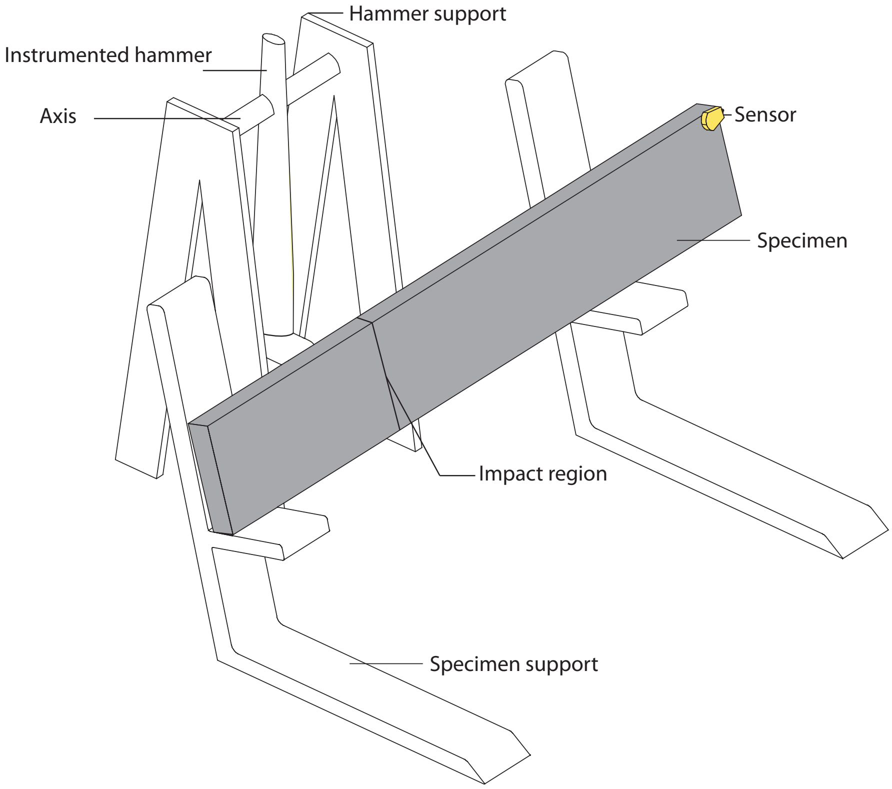

Figure 3.1.2: Tests disposition: Specimen and apparatus.

figure indicates specimen's vibrational modes. Blue color is for flexural xy modes, red color is for torsional modes and green color is for flexural xz modes. Figure 3.1.3a shows bad spectrum distribution: some modes (2^{nd} flexural xy and 1^{st} torsional, 3^{rd} flexural xy and 2^{nd} torsional) appear too close to one another in the spectrum, leaving some wide empty frequency bands. When two modes appear too close to each other then it is a problem because then two close peaks having finite width. Figures 3.1.3b and 3.1.3c have a good number of well-separated peaks in the spectrum, however 3.1.3b, have more modes to analyse and therefore is a better distribution choice. In addition, 275 × 50 × 10 mm^3 specimens require relatively less amount of material to make. Figure 3.1.3d shows only six modes in the frequency range of analysis and this specimen also needs more material and was discarded for that reason.

A complete analysis was then performed for the selected specimen geometry 275 × 50 × 10 mm^3. Figure 3.1.4 shows the mode shapes for displacement variations for the extracted modes. From these diagrams a fixed location for the

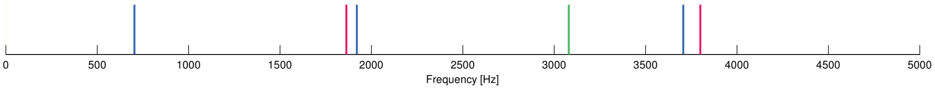

(a) 225 × 50 × 10 mm^3 specimen.

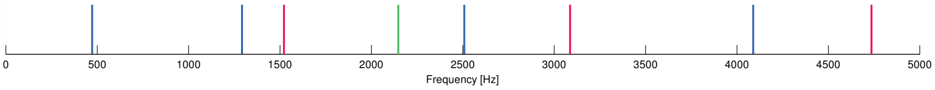

(b) 275 × 50 × 10 mm^3 specimen.

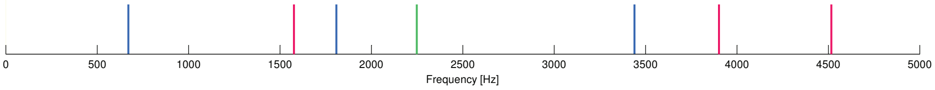

(c) 325 × 50 × 20 mm^3 specimen.

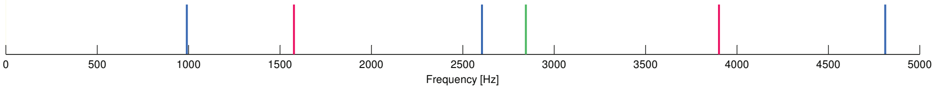

(d) 325 × 50 × 30 mm^3 specimen.

Figure 3.1.3: Modal analysis simulations done with FEM software for different specimen geometries.

accelerometer at the corner of the specimen where the deformation is maximum was selected. This mode shape analysis gave important information about how to choose the point of impact location. Hitting at a high deformation location made the specimen capable of exciting the desired number of modes. For instance, 1st flex xz (Fig. 3.1.4d) mode could not be excited due to the specimen disposition on the testing support (the impact direction is normal to the plane of displacement).

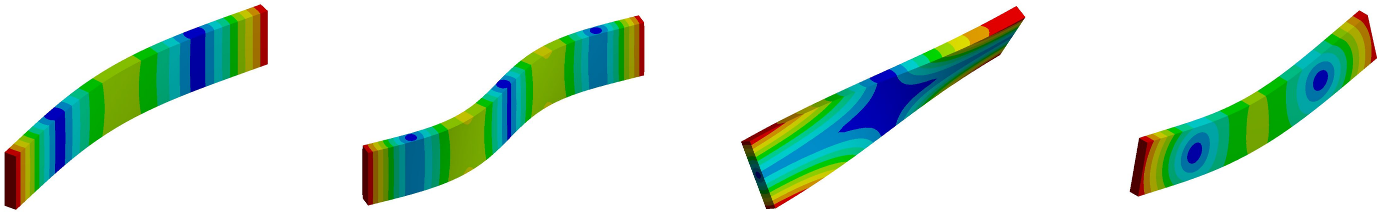

(a) 1stflex xy:472.3 Hz. **(b)** 2ndflex xy:1292.9 Hz. **(c)** 1sttor:1522.1 Hz. **(d)** 1stflex xz:2147.2 Hz.

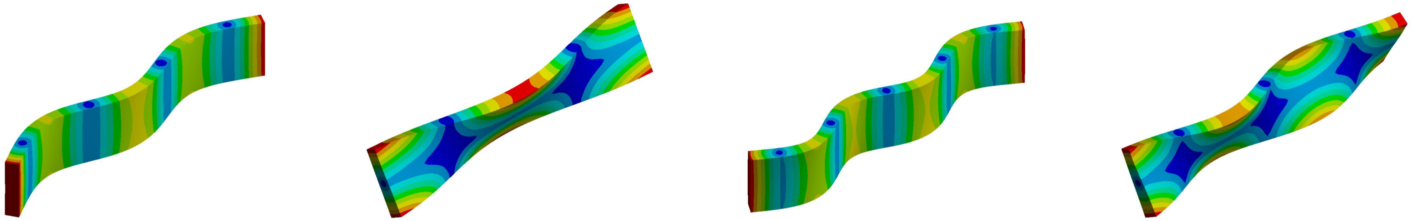

(e) 3rdflex xy:2508.4 Hz. **(f)** 2ndtor:3087.8 Hz. **(g)** 4thflex xy:4089.2 Hz. **(h)** 3rdtor:4736.2 Hz.

Figure 3.1.4: FEM total deformation modal analysis.

3.1.3.2 Point of impact results

In order to optimize the test method and obtain more modal experimental spectrum response, an investigation to determine the point of impact experiment was performed. It was done by varying the impact point by one centimetre from the geometric centre towards one end of the specimen. Response spectra for the same impact energy level for different impact locations plotted in Figure 3.1.5. Impact at the geometric center of the specimen generated only a few modes. This observation can be justified from the fact that for many modes geometric center is a node position and hitting at the node position cannot generate that specific mode.

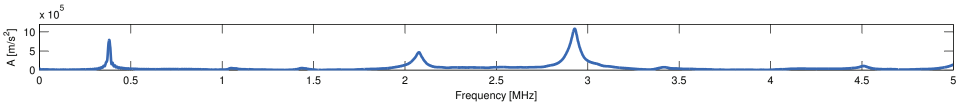

(a) Geometric center.

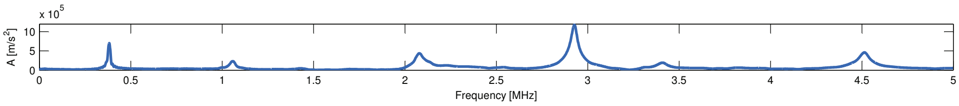

(b) +1 cm offset.

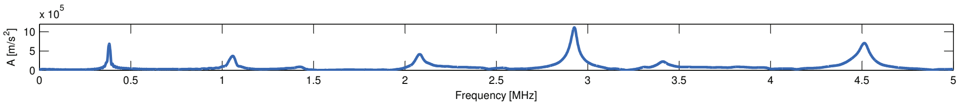

(c) +2 cm offset.

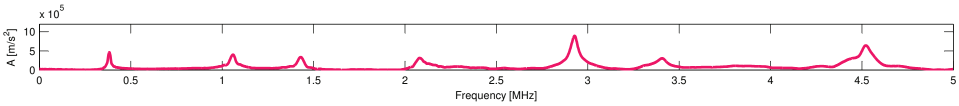

(d) +3 cm offset.

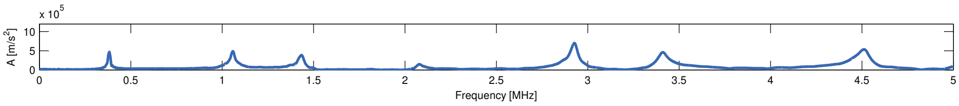

(e) +4 cm offset.

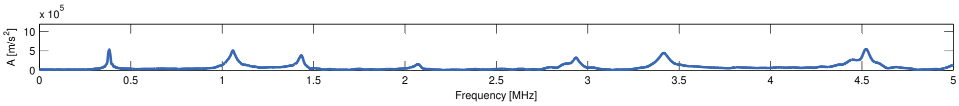

(f) +5 cm offset.

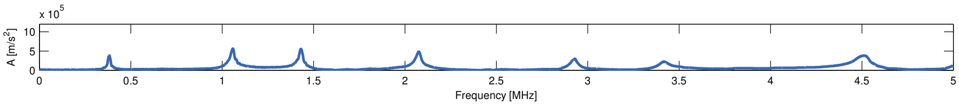

(g) +6 cm offset.

Figure 3.1.5: Frequency response of the same specimen for different impact locations as shown in Figure 3.1.2.

Thus, impacting on geometric centre of the specimen (Fig. 3.1.5a) activates only three modes (first flexural, third flexural and second torsional, Figures 3.1.4a,3.1.4e and 3.1.4f) because second flexural and first torsional (Figs. 3.1.4b and 3.1.4c) have a node (zero displacement) at that impact point. As the impact point is moved from the geometric center, other modes start to appear. One and two centimetres offsets from the geometric centre (Figs. 3.1.5b and 3.1.5c) show low amplitude modes near 1000 to 1500 Hz frequencies. Three centimetres offset from the geometric centre (Fig. 3.1.5d) seems to be the most appropriate position since the modes are stable and have relatively high amplitudes. Other positions also have interesting spectral response (Figs. 3.1.5e,3.1.5f and 3.1.5g) but were discarded because the specimen became unstable on the test support for those cases. First flexural xz (Fig. 3.1.4d) mode could not be excited for obvious reasons (no peaks at 2147 Hz).

3.1.3.3 Linear and non-linear results

Table 3.1.4 shows the variations of toughness, elastic modulus and flexural strength at different stages of ageing or degradation. As can be observed, there is a remarkable decay for some of these parameters due to the fibre degradation. Note that toughness increases at the early stage of ageing because of a late hydration process due to the thermal treatment. However, during later stages of ageing, toughness decreases due to the fibres degradation. σ_{max} did not have any noticeable change.

Table 3.1.4: Mean values and standard deviation of mechanic parameters extracted from four points bending test.

Hours	Toughness [Nmm]	Ec_{flex} [GPa]	σ_{max} [MPa]
0	142.45 ± 37.1	4428 ± 534.0	11.31 ± 2.0
8	167.528 ± 29.3	2745.52 ± 821.7	11.08 ± 1.3
24	123.77 ± 13.7	3151.85 ± 320.5	10.02 ± 1.0
90	113.77 ± 49.4	3333.42 ± 604.7	10.93 ± 1.9

The experimental and the theoretical resonance frequencies are plotted in Figure 3.1.6a. The slight difference between these two series on the graph is due to the plate cutting and manufacturing. The experimental data correspond to 28 specimens after being cured at 20 °C in wet chamber for 28 days, before any ageing or fibre degradation. As commented before, NIRAS tests were performed in order to evaluate the frequency and non-linearity parameter changes due to the material degradation.

After computing the frequency values for every mode, the experimental data points were plotted in Figure 3.1.6b. Frequency and alpha variation (Δ frequency and $\Delta\alpha$) was computed using Eq. 3.1.3:

$$\frac{P_t - P_0}{P_0} \cdot 100 \tag{3.1.3}$$

where P_t is the parameter at t time and P_0 is the parameter for the undamaged specimen at the beginning of the experiment (after 28 days of curing in the wet chamber). Table 3.1.5 shows mean values of α and frequency for all modes and ages.

Table 3.1.5: Mean values of frequency [Hz] and alpha for all ages [h] and modes. Standard deviations are given under each value.

	1^{st} Flex		2^{nd} Flex		1^{st} Tor		3^{rd} Flex		2^{nd} Tor		4^{th} Flex		3^{rd} Tor	
Age	α	Freq	α	Freq	α	Freq	α	Freq	α	Freq	α	Freq	α	Freq
0	$9.4\cdot10^{-8}$	426	$6.6\cdot10^{-8}$	1189	$5.5\cdot10^{-8}$	1405	$8.4\cdot10^{-8}$	2348	$2.8\cdot10^{-8}$	2910	$7.1\cdot10^{-8}$	3867	$2.4\cdot10^{-8}$	4515
	$3.8\cdot10^{-8}$	39	$5.5\cdot10^{-8}$	83	$5.1\cdot10^{-8}$	115	$1.5\cdot10^{-8}$	151	$2.6\cdot10^{-8}$	167	$1.5\cdot10^{-8}$	217	$1.6\cdot10^{-8}$	234
4	$9.9\cdot10^{-8}$	424	$7.1\cdot10^{-8}$	1182	$5.4\cdot10^{-8}$	1393	$6.7\cdot10^{-8}$	2334	$1.7\cdot10^{-8}$	2884	$5.9\cdot10^{-8}$	3847	$1.9\cdot10^{-8}$	4473
	$4.8\cdot10^{-8}$	34	$4.9\cdot10^{-8}$	77	$1.5\cdot10^{-8}$	107	$2.1\cdot10^{-8}$	137	$4.6\cdot10^{-8}$	154	$2.3\cdot10^{-8}$	218	$3.6\cdot10^{-8}$	2.16
8	$1.1\cdot10^{-7}$	429	$6.3\cdot10^{-8}$	1190	$2.9\cdot10^{-8}$	1401	$5.3\cdot10^{-8}$	2344	$1.3\cdot10^{-8}$	2895	$8.3\cdot10^{-8}$	3857	$1.8\cdot10^{-8}$	4487
	$6.4\cdot10^{-8}$	35	$3.0\cdot10^{-8}$	77	$1.2\cdot10^{-8}$	109	$3.1\cdot10^{-8}$	140	$5.0\cdot10^{-8}$	157	$2.0\cdot10^{-8}$	211	$2.5\cdot10^{-8}$	221
12	$1.2\cdot10^{-7}$	428	$5.9\cdot10^{-8}$	1191	$2.9\cdot10^{-8}$	1401	$5.7\cdot10^{-8}$	2349	$1.5\cdot10^{-8}$	2898	$3.6\cdot10^{-8}$	3862	$1.1\cdot10^{-8}$	4497
	$6.2\cdot10^{-8}$	34	$3.0\cdot10^{-8}$	79	$1.2\cdot10^{-8}$	110	$2.0\cdot10^{-8}$	205	$2.5\cdot10^{-8}$	157	-	201	-	215
20	$8.7\cdot10^{-8}$	435	$3.8\cdot10^{-8}$	1207	$1.2\cdot10^{-8}$	1420	$3.7\cdot10^{-8}$	2372	$8.8\cdot10^{-9}$	2921	-	3881	-	4530
	$4.6\cdot10^{-8}$	35	$1.1\cdot10^{-8}$	78	$4.3\cdot10^{-8}$	107	$1.9\cdot10^{-8}$	135	$2.5\cdot10^{-9}$	157	-	201	-	215
24	$7.8\cdot10^{-8}$	437	$3.6\cdot10^{-8}$	1210	$1.6\cdot10^{-8}$	1424	$3.1\cdot10^{-8}$	2380	$7.9\cdot10^{-9}$	2931	-	3917	-	4549
	$4.3\cdot10^{-8}$	37	$1.6\cdot10^{-8}$	76	$1.6\cdot10^{-8}$	109	$8\cdot10^{-9}$	139	$2.5\cdot10^{-9}$	155	-	201	-	216
33	$7.2\cdot10^{-8}$	439	$3.5\cdot10^{-8}$	1213	$1.4\cdot10^{-8}$	1428	$2.7\cdot10^{-8}$	2385	$7.7\cdot10^{-9}$	2939	-	3922	-	4556
	$3.5\cdot10^{-8}$	35	$1.9\cdot10^{-8}$	77	$6.2\cdot10^{-8}$	135	$2.1\cdot10^{-9}$	153	$2.5\cdot10^{-9}$	202	-	214		
40	$5.1\cdot10^{-8}$	441	$3.6\cdot10^{-8}$	1220	$1.5\cdot10^{-8}$	1435	$2.8\cdot10^{-8}$	2397	$5.8\cdot10^{-9}$	2952	-	3951	-	4581
	$3.1\cdot10^{-8}$	36	$1.7\cdot10^{-8}$	77	$2.4\cdot10^{-8}$	102	$8.7\cdot10^{-9}$	136	$9.0\cdot10^{-9}$	1542	-	197	-	209
48	$6.2\cdot10^{-8}$	443	$2.3\cdot10^{-8}$	1226	$1.3\cdot10^{-8}$	1443	$2.7\cdot10^{-8}$	2408	$4.5\cdot10^{-9}$	2965	-	3963	-	4596
	$4.4\cdot10^{-8}$	34	$1.4\cdot10^{-8}$	78	$1.0\cdot10^{-8}$	110	$8.6\cdot10^{-9}$	134	$2.1\cdot10^{-8}$	151	-	196	-	210
63	$4.1\cdot10^{-8}$	446	$2.4\cdot10^{-8}$	1231	$1.2\cdot10^{-8}$	1450	$1.3\cdot10^{-8}$	2419	$5.4\cdot10^{-9}$	2981	-	3978	-	4619
	$1.9\cdot10^{-8}$	34	$9.2\cdot10^{-9}$	76	$1.5\cdot10^{-9}$	103	$1.4\cdot10^{-8}$	134	$7.9\cdot10^{-9}$	151	-	169	-	208
90	$1.4\cdot10^{-7}$	446	$2.3\cdot10^{-8}$	1233	$1.2\cdot10^{-8}$	1451	$1.9\cdot10^{-8}$	2420	$6.1\cdot10^{-9}$	2982	-	3980	-	4620
	$3.2\cdot10^{-8}$	38	$7.35\cdot10^{-9}$	75	$8.5\cdot10^{-9}$	102	$7.7\cdot10^{-9}$	134	$1.8\cdot10^{-9}$	149	-	194	-	206

Figure 3.1.6b shows frequency increase for all modes. It is important to note that the low frequency modes show more relative variation than the high frequency modes. It is also noted that all modes in the range of our study have the same tendency or behaviour.

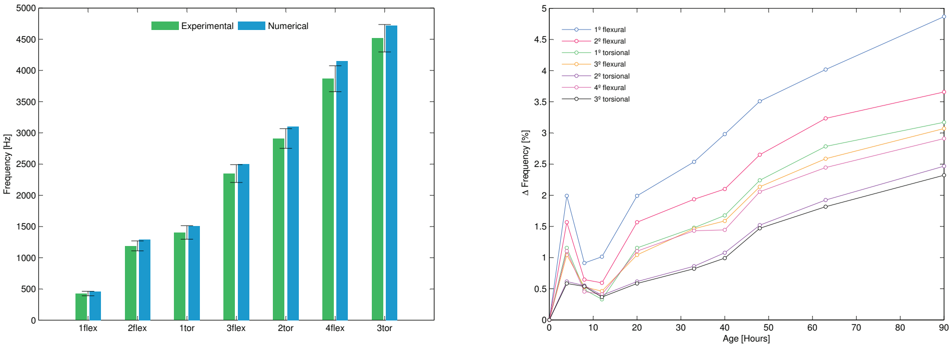

(a) **(b)**

Figure 3.1.6: Figure 3.1.6a represents theoretical and experimental frequency comparisons. Figure 3.1.6b plots the frequency variation with ageing process.

During the early stages of ageing there is a slight decrease of the frequency variation which coincides with that shown in the Table 3.1.4 which then stabilizes over time. Then it shows monotonic increase. After monitoring all resonance frequency modes, it is concluded that monitoring one mode is sufficient for defining the frequency variation during the ageing process.

Non-linearity parameter α was computed using Eq. 3.1.2. Figure 3.1.7 shows the α variation as the specimen ages. With ageing the percentage change of this parameter is much higher than the linear parameter. Clearly hysteretic parameter is more sensitive to ageing than the linear parameters. One can note that when the age of degradation increases, for most modes the variation of the hysteretic parameter monotonically increases.

2^{nd} flexural, 1^{st} torsional, 3^{rd} flexural and 2^{nd} torsional modes show similar behaviour. Generally, when the vibrational mode is at relatively high frequencies, the non-linearity parameter derived from that mode is more sensitive to ageing. However signal strengths for 4^{th} flexural and 3^{rd} torsional modes were too weak to generate consistent and reliable results.

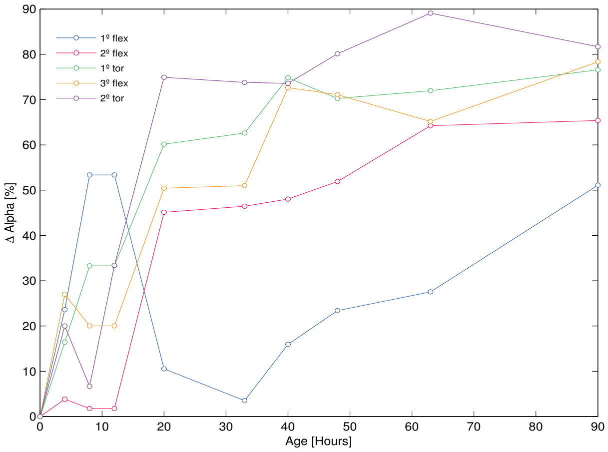

Figure 3.1.7: Non-linearity parameter variation with ageing.

3.1.3.4 SEM observations

In order to see the physical condition of the fibres, scanning electron microscopy images were taken at different magnifications (Fig. 3.1.8).

The images were taken for two different states as mentioned in Table 3.1.1, at the beginning of the ageing process and at the end (90 hours under wet and warm conditions of ageing).

Figure 3.1.8a is a 200× magnification of the fibres embedded in the cement matrix 28 days after setting. The fibres were clean and their surfaces were smooth. After 90 hours of ageing similar specimen was analysed under SEM (Fig. 3.1.8b) and a new layer of new products over the fibres were noticed. In 6000× magnification images the smooth surface condition can be clearly seen. Figure 3.1.8c shows the initial state of the fibre with the intact surface and Figure 3.1.8d shows a deteriorated fibre with small voids and damaged surface.

3.1.4 Conclusions

In this study, it has been corroborated that NIRAS is a suitable technique to evaluate ageing process for GRC specimens. Different vibrational modes have been evaluated over a frequency range in order to compare the variations of linear and non-linear parameters with ageing. It is observed that non-linear parameters are more sensitive to ageing than linear parameters. Scanning electron microscopy and four point bending tests corroborated NDE observations.

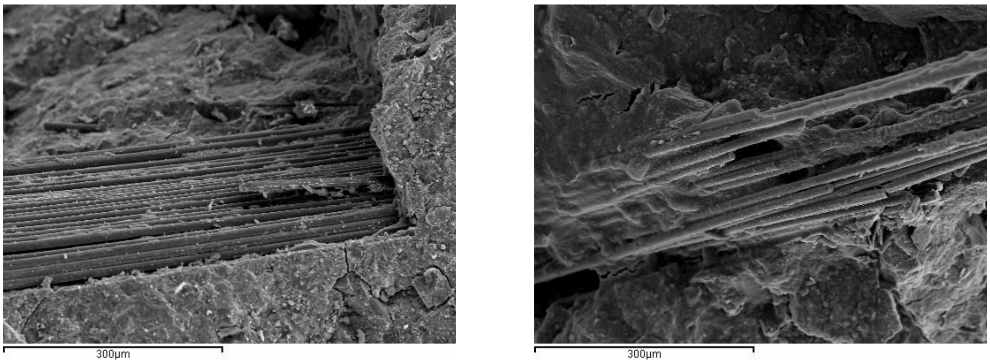

(a) Unaged fibre 200× magnification. **(b)** 90 hours aged fibre 200× magnification.

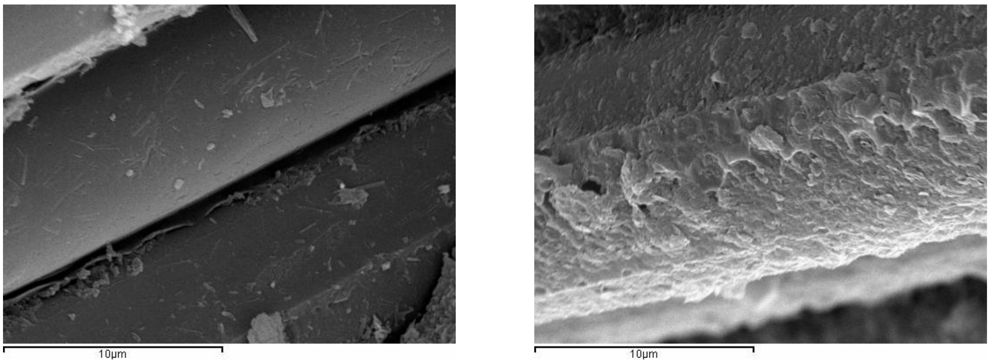

(c) Unaged fibre 6000× magnification. **(d)** 90 hours aged fibre 6000× magnification.

Figure 3.1.8: SEM images of unaged and aged specimens.

Acknowledgments

The authors acknowledge the financial support of the Ministerio de Ciencia e Innovación MICINN, Spain, and FEDER funding (Ondacem Project: BIA 2010-19933).

References

[1] A. Bentur and S. Mindess, *Fibre Reinforced Cementitious Composites, Second Edition*, ser. Modern Concrete Technology. Taylor & Francis, 2006.

[2] P. Purnell, N. R. Short, C. L. Page, A. J. Majumdar, and P. L. Walton, "Accelerated ageing characteristics of glass-fibre reinforced cement made with new cementitious matrices," *Composites Part A: Applied Science and Manufacturing*, vol. 30, no. 9, pp. 1073–1080, 1999.

[3] K. Kopecskó, “Durability of glass fibres,” in *6th RILEM Symposium on Fibre Reinforced Concrete*, RILEM publications, 2004, pp. 585–594.

[4] A. Enfedaque, D. Cendón, F. Gálvez, and V. Sánchez-Gálvez, “Analysis of glass fiber reinforced cement (GRC) fracture surfaces,” *Construction and Building Materials*, vol. 24, no. 7, pp. 1302–1308, 2010.

[5] P. Purnell, N. R. Short, C. L. Page, and A. J. Majumdar, “Microstructural observations in new matrix glass fibre reinforced cement,” *Cement & Concrete Research*, vol. 30, pp. 1747–1753, 2000.

[6] A. Enfedaque, L. Sánchez-Paradela, and V. Sánchez-Gálvez, “An alternative methodology to predict aging effects on the mechanical properties of glass fiber reinforced cements (GRC),” *Construction and Building Materials*, vol. 27, no. 1, pp. 425–431, 2012.

[7] J. A. Bogas, M. G. Gomes, and A. Gomes, “Compressive strength evaluation of structural lightweight concrete by non-destructive ultrasonic pulse velocity method,” *Ultrasonics*, vol. 53, no. 5, pp. 962–972, 2013.

[8] V. M. Malhotra and N. J. Carino, *Handbook on Nondestructive Testing of Concrete Second Edition*. Taylor & Francis, 2003.

[9] D. Breysse, G. Klysz, X. Dérobert, C. Sirieix, and J. Lataste, “How to combine several non-destructive techniques for a better assessment of concrete structures,” *Cement and Concrete Research*, vol. 38, no. 6, pp. 783–793, 2008.

[10] Y. Ito and T. Uomoto, “Nondestructive testing method of concrete using impact acoustics,” *NDT & E International*, vol. 30, no. 4, pp. 217–222, 1997.

[11] K. Y. Jhang, “Nonlinear ultrasonic techniques for non- destructive assessment of micro damage in material : A review,” *International Journal of Precision Engineering and Manufacturing*, vol. 10, no. 1, pp. 123–135, 2009.

[12] J. Chen, A. R. Jayapalan, J. Y. Kim, K. E. Kurtis, and L. J. Jacobs, “Rapid evaluation of alkali-silica reactivity of aggregates using a nonlinear resonance spectroscopy technique,” *Cement and Concrete Research*, vol. 40, no. 6, pp. 914–923, 2010.

[13] K. J. Leśnicki, J. Y. Kim, K. E. Kurtis, and L. J. Jacobs, “Characterization of ASR damage in concrete using Nonlinear Impact Resonance Scoustic Spectroscopy technique,” *NDT & E International*, vol. 44, no. 8, pp. 721–727, 2011.

[14] J. N. Eiras, T. Kundu, M. Bonilla, and J. Payá, “Nondestructive monitoring of ageing of alkali resistant glass fiber reinforced cement (GRC),” *Journal of Nondestructive Evaluation*, vol. 32, no. 3, pp. 300–314, 2013.

[15] B. Standard, *Precast concrete products - Test method for glass-fibre reinforced cement - Part 5. Measuring bending strength, 'Complete bending test' method.* 1998.

[16] F. de Larrard, *Concrete Mixture Proportioning: A Scientific Approach*, ser. Modern Concrete Technology. Taylor & Francis, 2005.

[17] J. Chen, J. Y. Kim, K. E. Kurtis, and L. J. Jacobs, “Theoretical and experimental study of the nonlinear resonance vibration of cementitious materials with an application to damage characterization,” *The Journal of the Acoustical Society of America*, vol. 130, no. 5, pp. 2728–2737, 2011.

[18] K. E. A. Van Den Abeele, P. A. Johnson, and A. Sutin, “Nonlinear elastic wave spectroscopy (NEWS) techniques to discern material damage, Part II,” *Research in Nondestructive Evaluation*, vol. 12, pp. 17–30, 2000.

3.2 Ultrasonic and impact spectroscopy monitoring on internal sulphate attack of cement-based materials[6]

[6] *V. Genovés, F. Vargas, J. Gosálbez, A. Carrión, M.V. Borrachero, and J. Payá. "Ultrasonic and impact spectroscopy monitoring on internal sulphate attack of cement-based materials," Materials & Design, vol. 125, pp. 46–54, 2017.*

Abstract

An exhaustive monitoring of an internal sulphate attack of Portland cement-based materials is addressed. Four series of Portland cement mortars with different amounts of gypsum (0%-2% SO_3 respect to the cement by mass) were monitored by means of physical, microstructural and non-destructive tests, studying specimens with a low expansion rate to examine the sensitivity of the applied techniques. The expansion analysis has shown the suitability of a fitting model, allowing the examination of two characteristic parameters: the characteristic time of the expansion reaction and the maximum amplitude of the expansion. In the mechanical analysis, higher values of R_c and R_f were attained as the gypsum content decreased. A microstructural analysis (thermogravimetry and FESEM) supported ettringite formation and expansion process. These results have been correlated with non-destructive tests: impact resonance acoustic spectroscopy and ultrasonic measures. The dynamic modulus and ultrasonic pulse velocity have closely predicted the stiffness of the specimens. The total material attenuation (absorbed energy of the chirp signal ultrasonic wave) presented different trends, showing clear differences for the most damaged series (2% SO_3). Attenuation supplied interesting information about the hardening process and the microcracking effect due to a mortar expansion higher than 0.04%. The novelties of this study are the exhaustive monitoring of an internal sulfate attack, as well as the examination of the sensitivity of brand new NDT techniques when this damage process overlaps with the curing process.

3.2.1 Introduction

Sulphate attack is considered one of the most aggresive causes of concrete degradation. Ettringite triggers expansion mechanisms that have harmful effects on the Portland cement matrix, causing micro-cracking and, consequently, a reduction in the stiffness and strength. Primary ettringite has no negative effect because the expansions produced by the reaction between C_3A and the sulphate anions are absorbed by fresh concrete. Secondary ettringite is formed for months, or even years after the concrete has been hardened [1]. The stresses that appear when an external or internal source of sulphate salts reacts with calcium aluminates hydrates (C-A-H) can spoil the matrix, causing micro-cracks, expansion and spalling. Additionally, gypsum is also formed by the reaction of sulphate ions and portlandite [2, 3]. Moreover, delayed ettringite formation (DEF) happens when concrete products are cured at high temperatures, and the transformation of the monosulphoaluminate (Afm) phase to the trisulphoaluminate (Aft) phase also produces internal stress after thermal curing.

There are two types of sulphate attack in concrete. The main difference between them is the location of the sulphate source: an external sulphate attack (ESA) and an internal sulphate attack (ISA). In an ESA process, sulphates present in the ground, water or air (like gypsum soils, rich sulphate-mineral waters, or SO_3 polluted air) penetrate into the capillary network of the concrete and react with the C-A-H compounds, forming ettringite [4]. The stresses produce a damage gradient from the surfaces to the core of the element. In contrast, ISA yields damage in the Portland cement matrix through the sulphates contained in the original mix (a high SO_3 percentage in the cement used, aggregates with sulphate or sulphide minerals, mixing water with high sulphate concentration), releasing them over time. If the sulphates contained in the mix are free initially, the setting process of the concrete could be delayed, and also promote a loss of the early-age strength gain over time. In the ISA case, the damage homogeneously spreads throughout the concrete matrix. Also an homogeneous deterioration process can be achieved when sulfide containing aggregates are oxidized by molecular oxygen in the air, and the sulfide is transformed to sulphate, which reacts towards C-A-H [5].

These degradation processes have become a worldwide problem responsible for the premature deterioration and development of pathologies in countless structures. It can be observed in certain circumstances if specific parameters are met simultaneously, including the concrete formula, the temperature at which the concrete has been exposed, and the presence of water. The conditions under which the degradation takes place, the impact of secondary ettringite formation on the properties of the concrete, and the techniques of diagnosis, are still subjects of intense debate [6]. Several authors have worked hard on understanding the large number of factors that play a role in ISA: sulfates and aluminates in the cement [6], drying and wetting cycles [7], temperature, etc. Some other studies have investigated the role of different additives and mineral additions to improve the behaviour of cement-based composites under sulphate attack [8–11]. All the aforementioned studies quantitatively characterize the mechanical damage to the concrete due to sulfate attack using different physical/mechanical parameters, such as the flexural strength, compressive strength, and long term linear strains (expansion). The microstructure of cement mortars are usually characterized by scanning electron microscope (SEM) equipped with energy dispersive X-ray spectroscopy (EDS). Moreover, recent studies have monitored the sulphate attack process with XRD [12] and combined methods with micro-tomography, obtaining significant additional information [13].

During recent years, Non-Destructive Testing (NDT) technique applied to concrete have been investigated, especially ultrasonics and impact resonance acoustic spectroscopy, in order to obtain new measures of the physical and mechanical properties of the materials without damaging the specimen under testing [14]. Studies using acoustic spectroscopy have shown remarkable results monitoring sulphate attack in cementitious composites by means of linear and non-linear parameter determination [15, 16]. In ultrasonic-based NDT, one of the most widely used parameters, due to its robustness, is the ultrasonic pulse velocity (UPV). Some experimental studies have demonstrated that the UPV of P-waves is suitable for estimating the changes in the dynamic modulus of concrete depending on the sulphate attack damage [8, 9]. Other studies based on ultrasound propagation have indicated that ultrasonic wave attenuation can be used to define different cementitious materials, distinguishing the microstructure, permeability or porosity, and other characteristics in both hardened [17–20] and fresh states [21].

The main aim of the present paper is to develop an exhaustive temporal monitoring of the evolution of mortars which have suffered an ISA with different degrees of damage by measuring different parameters, as well as correlating the results obtained using traditional techniques with other more new techniques based on NDT. The novelty of this study is not only the exhaustive monitoring of a damage process on a Portland cement composite with NDT techniques, but also the examination of the sensitivity of brand new NDT techniques when the damage process overlaps with the curing process (and the consequent stiffness and strength developments). This paper is structured as follows. Section 3.2.2 presents the materials studied as well as the different tests and measures used in this study to monitor the ISA process. Section 3.2.3 describes the results obtained from the application of the different tests to the specimens. Lastly, the conclusions are summarized in Section 3.2.4.

3.2.2 Experimental

Several tests and measures were carried out in this study in order to monitor the ISA process in Portland cement based systems (mortar and pastes). The tests were divided into three categories: physical, microstructural, and non-destructive tests. The expansion (Exp), compressive strength (R_c), and flexural strength (R_f) were determined by means of physical tests. For the microstructural tests, a high resolution thermogravimetry (HRTG) and field emission scanning electron microscopy (FESEM) were performed. Lastly, in the category of non-destructive tests (NDT), the dynamic modulus (E_{dyn}), ultrasonic pulse velocity (v_p), and ultrasonic wave attenuation (α_{mat}) were determined. All tests performed for each series are summarized in Table 3.2.1.

Table 3.2.1: Chronogram of the tests performed for all mortar/paste series at different ages (days).

Tests	Days	3	7	10	14	17	21	24	28	35	42	50	56	64	70	77	84	90	120	150	180
Physical	Exp	●	●	●	●	●	●	●	●	●	●	●	●	●	●	●	●	●	●	●	●
	R_c		●		●				●				●					●			●
	R_f		●		●				●				●					●			●
μstructural	HRTG																	●			●
	FESEM																	●			
NDT	E_{dyn}	●	●	●	●	●	●	●	●	●	●	●	●	●	●	●	●	●	●	●	●
	v_p	●	●	●	●	●	●	●	●	●	●	●	●	●	●	●	●	●	●	●	●
	α_{mat}	●	●	●	●	●	●	●	●	●	●	●	●	●	●	●	●	●	●	●	●

3.2.2.1 Materials and specimens

A 40 × 40 × 160 mm^3 geometry was chosen for the mortar specimens, using various dosages to obtain four series with different rates of ISA damage varying the total SO_3 content. In Table 3.2.2, the dosages for the four performed series are summarized. Twenty-four mortar mixes were prepared according to the Spanish standard UNE-EN 196 to obtain three specimens per batch, which were used for physical and non-destructive tests. Additionally, four pastes were made to perform micro-structural tests following the proportions in Table 3.2.2. After the iron moulds were filled with the fresh mortar, they were stored in a wet chamber (20°C and 100% RH) for 24 hours. After that, the specimens were removed from the moulds and cured under water at 20°C for the whole duration of the experiment.

The cement used in this experiment was a Spanish CEM BL II/A-L 42,5-R with 5.95% tricalcium aluminate (C_3A) and 4.63% SO_3 by weight. The rest of main components were 19.27% SiO_2, 2.45% Al_2O_3, 65.85% CaO, 0.1% Na_2O, 0.74% K_2O, 0.4% MgO, 6.48% LOI by weight.

The sulphate source was pure $CaSO_4 \cdot 2H_2O$ (gypsum) and the aggregate was a normalized silica sand (NORMSAND). The ratio of water to binder (cement+gypsum) was maintained constant for all dosages in this experiment (0.5). Four mortar series were prepared, in which the added gypsum produced an increasing SO_3 content: in 0%, 1%, 1.5%, and 2%.

Table 3.2.2: Dosages for mortar mix series by weight [g].

Series	Sand	Cement	Water	Gypsum	added SO_3 [%]
0%	1350.0	450.0	225.0	0	0
1%	1350.0	440.3	225.0	9.7	1
1.5%	1350.0	435.5	225.0	14.5	1.5
2%	1350.0	430.6	225.0	19.4	2

3.2.2.2 Physical tests

Physical tests were performed in order to monitor the ISA process and correlate the destructive and conventional parameters with the non-destructive ones. As mentioned earlier, 24 mixes (6 for each dosage) were prepared for the physical and NDT, 4 of them (one per dosage) for expansion and NDT (and also for the last destructive test), and the remaining 20 (5 per dosage) for the intermediate destructive tests (determining flexural and compressive strength) at different ages.

In order to monitor the expansion undergone by the specimens, the Demec extensometry (mechanical strain gauge) method was used instead of that proposed by the ASTM standard [22]. The equipment was a Mituyoto ID-C112MB ($\pm 1\mu$m) extensometer, and metal disks were attached centred on the two adjacent faces (excluding the rough face) with 10 cm separation between them. Thus, 6 measurements (2 measurements for each specimen, 3 specimens per series) per series and expansion test age were carried out.

For the mechanical tests (determining the compressive and flexural strengths) an universal testing machine was used (INSTRON model 3382) following the Spanish standard UNE-EN-196. For each curing age and series, three specimens were tested by means of three-point bending tests (R_f) and the six obtained semi-prisms were used to determine the compressive strength (R_c).

3.2.2.3 Microstructural tests

For the purpose of determining the internal changes of the hydrated Portland cement matrix, a microstructural analysis was carried out by means of HRTG and FESEM. These analyses were carried out on the pastes, which had the same dosage as the mortars, excluding the sand.

The HRTG tests were performed in order to support the formation of ettringite formed for all pastes. In order to carry out this analysis, portions of the paste samples were taken and pulverized with an agate mortar, adding a small amount of acetone. The solid was filtered and dried at 60°C for 15 min. The equipment used was an ultrabalance Mettler TGA 850. Sealed aluminium crucibles of 100 ml were used, each with a lid with a micro-hole to create a water vapour self-generated atmosphere [23]. The analysis was carried out in a dry nitrogen atmosphere with a gas flow of 75 mL/min and a temperature interval of 35°C–300°C. For high resolution thermogravimetric analysis (Max-Res, Stare software), the lowest heating rate was 0.1°C/min and the highest one 10°C/min. The heating rate was changed according to the mass loss rate. The highest heating rate was achieved for mass loss rates lower than 1 μg s^{-1}, and the lowest heating rate was achieved for mass loss rates higher than 3 μg s^{-1}. This analysis was carried out to be more sensitive in detecting peaks on thermogravimetric derivative curves (DTG) when the various decomposition processes are very close in their temperature range (the case of decomposition of calcium silicate hydrates and ettringite). The main decomposition DTG peak related to the calcium silicate hydrates is recorded in 110°C–130°C, that for the ettringite within the 140°C–150°C range, and those for the calcium aluminosilicate and calcium aluminate hydrates within the 210°C–220°C range [16].

For the FESEM observations, portions of the paste samples were taken, drying at 60°C and coating them with a carbon layer. A ZEISS (ULTRA 55) electron microscope was used, setting it to voltages of 2–3 kV and to distances between 3.9 mm and 6.0 mm.

3.2.2.4 Non-Destructive tests

Impact resonance acoustic spectroscopy

The dynamic modulus (E_{dyn}) is a mechanical parameter highly correlated with the Young modulus in concrete [14]. Some studies have demonstrated the quasi-equivalence between both parameters [15], with E_{dyn} being an accurate indication of the stiffness of the concrete, without the need for destroying the specimen during the test. To determine E_{dyn} (transverse mode), an ASTM standardized method was used [24]. Specimens were placed in an acoustic foam absorber surface and were struck ten times with a known mass sphere in the centre of the larger faces of the prismatic specimens. The signal was collected with a piezoelectric accelerometer sensor. The frequency was extracted from the frequency domain signal and mean values were calculated. After that, the corresponding ASTM equation was used to obtain E_{dyn}. Details about the layout can be seen in Figure 3.2.1.

Ultrasonic measurements

Different layouts can be used to make an ultrasonic inspection. In this study, a through-transmission setup was selected, since it offers good penetration and good accuracy for estimating the velocity and attenuation[17, 25–27]. The transducers (transmitter and receiver) used were the K1SC from General Electric. Both are broadband transducers with a bandwidth centred at 1 MHz. The transmitter transducer was excited directly by a programmable signal generator (Agilent 33120A) and the reception transducer was connected to a 40 dB preamplifier (Panametrics 5600B). The received and amplified ultrasonic signal was captured by a digital oscilloscope (Tektronix DPO3014) with a sampling frequency of 12.5 MHz. Finally, a laptop was used to control the signal generator and to acquire and store the digitized signals. The ultrasonic transducers were placed facing the longitudinal axis of the prismatic specimen, and they were fixed by two plastic clamps: a movable one to adjust to the specimen, and a fixed one. Pure vaseline at the transducer–specimen interfaces was used as an impedance coupling medium. Further details about the layout can be seen in Figure 3.2.2.

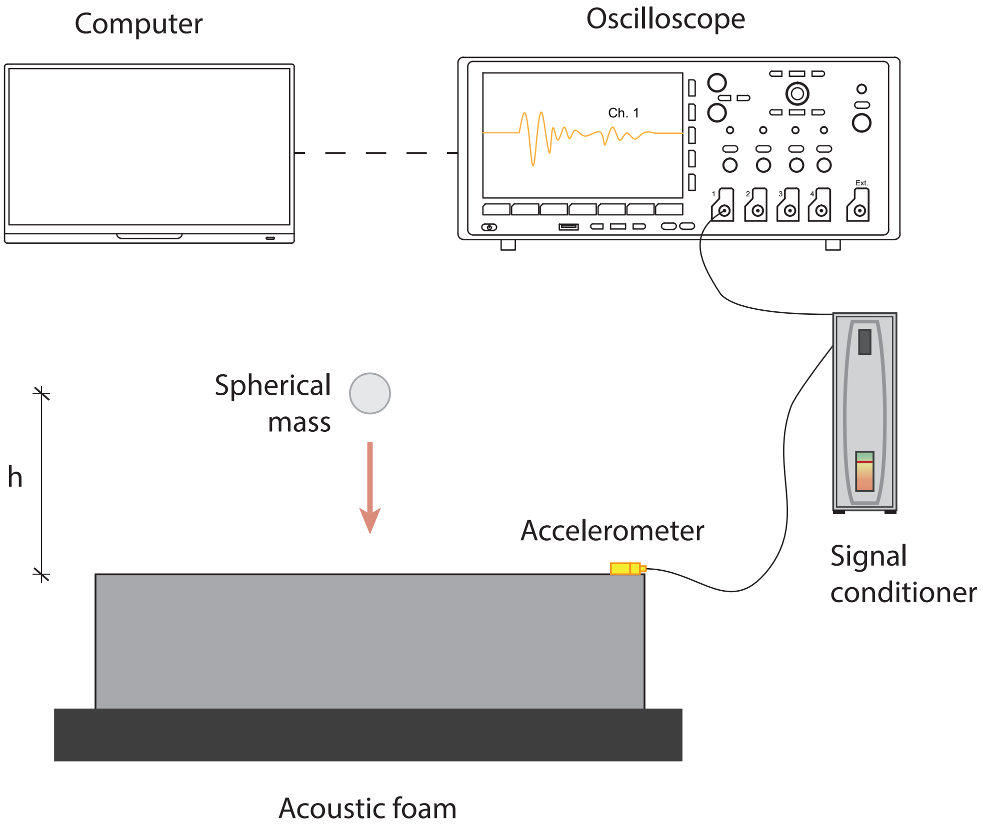

Figure 3.2.1: Scheme of equipment used in the resonant frequency test.

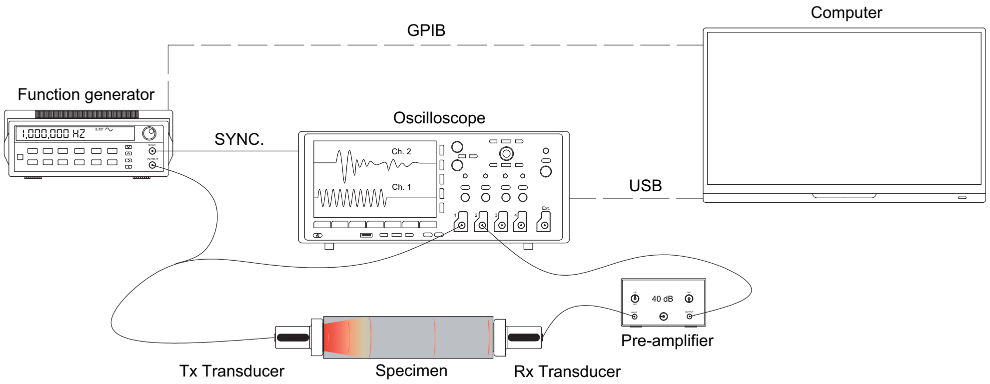

Figure 3.2.2: Scheme of equipment used in a typical ultrasonic inspection.

The transmitted signal s_{tx} was a swept-frequency signal (chirp). The mathematical expression of a linear chirp signal is

$$s_{tx}(t) = A_{tx}\cos\left(2\pi f_0 t + \pi\Delta_{f_{max}} t^2\right) \cdot rect\left(\frac{t-\frac{T}{2}}{T}\right) \tag{3.2.1}$$

$$\Delta_{f_{max}} = \frac{f_{max} - f_0}{T} \tag{3.2.2}$$

where A_{tx} is the amplitude of the signal, t is the time, f_0 is the fundamental frequency, T is the active time of the signal, and $\Delta_{f_{max}}$ controls the maximum frequency ($f_{max} = f_0 + T\Delta_{f_{max}}$) which is reached at T seconds (Eq. 3.2.2). The selected parameters were $A_{tx} = 10$ V, $f_0 = 100$ kHz, $f_{max} = 1$ MHz and $T = 200\,\mu$s.

The estimated ultrasound parameters from the received ultrasonic signal are the wave velocity and the total attenuation of the material. With $s_{rx}(t)$ the amplitude of the received signal, the propagation velocity (or UPV), v_p, is obtained as the ratio between the length of the specimen, d_{mat}, and the signal time arrival, τ_a (Eq. 3.2.3). The signal time arrival, t$_a$, was taken to be when x_{rx} exceeded 50% of the noise level of the received signal.

$$v_p[m/s] = \frac{d_{mat}}{t_a} \tag{3.2.3}$$

The ultrasonic wave attenuation due to the material, α_{mat}, can be calculated from the transmitted and received energies, taking into consideration the effect of the equipment and the distance travelled. Given the analytical expression and the specific parameters of the transmitted signal (Eq. 3.2.1), the transmitted energy E_{tx} can be obtained theoretically using Eq.3.2.4. In this paper, E_{tx} equals 10 mJ and is constant throughout the test.

$$E_{tx}\,[J] = \int_0^\infty |s_{tx}(t)|^2 dt = \frac{A_{tx}^2 T}{2} + \frac{A_{tx}^2}{2}\int_0^T \cos(2\pi(2f_0)t + \pi(2\Delta f_{max})t^2)dt \approx \frac{A_{tx}^2 T}{2} \tag{3.2.4}$$

The total received energy, $E_{rx}(t)$, is the energy of the received signal acquired by the oscilloscope, obtained according to Eq. 3.2.5.

$$E_{rx}[\mathrm{J}] = \int_0^\infty s_{rx}^2(t)dt \tag{3.2.5}$$

The global attenuation associated to the measurement equipment (transducers, amplifier, wires, acquisition module, …), α_{equip}, is independent of the tested material and is constant over the test. In this paper, $\alpha_{equip} = -5$dB. The value of the preamplifier must also be subtracted ($\alpha_{preamp} = 40$ dB).

Considering all the aforementioned terms, the total attenuation of the material, α_{mat}, is obtained according to Eq. 3.2.6.

$$\alpha_{mat}[\mathrm{dB/cm}] = \frac{10 \cdot \log(E_{tx}[\mathrm{J}]) - 10 \cdot \log(E_{rx}(t)[\mathrm{J}]) - \alpha_{equip}[\mathrm{dB}] - \alpha_{preamp}[\mathrm{dB}]}{d_{mat}[\mathrm{cm}]} \tag{3.2.6}$$

3.2.3 Results and discussion

3.2.3.1 Physical tests

The prismatic mortars were stored under water after demoulding. In the samples with SO_3 added (in the chemical form of gypsum), the reaction between the calcium aluminates and the sulfate anions becomes very rapid, because of the high solubility of gypsum (ca. 2 g/L at 20°C) in water. In these conditions, the formation of secondary ettringite is achieved according to the following chemical equation:

$$3\,\mathrm{CaO} \cdot \mathrm{Al_2O_3} + 3\,(\mathrm{CaSO_4} \cdot 2\,\mathrm{H_2O}) + 26\mathrm{H_2O} \longrightarrow 3\mathrm{CaSO_4} \cdot 3\,\mathrm{CaO} \cdot \mathrm{Al_2O_3} \cdot 32\,\mathrm{H_2O} \tag{3.2.7}$$

The great molar volume of ettringite (710.32 cm^3/mol) promotes internal stress in the cementing matrix, and this yields an expansion. The expansion values ($\epsilon(t)$) of specimens with different amounts of added SO_3 were measured at different ages, and the expansion curves are given in Figure 3.2.3a. The control series, 0%, showed a small axial deformation due to the SO_3 content in the cement and hydrothermal changes (the temperature and humidity during the testing process). The rest of the series experienced significant expansion values at short and long curing times. It is noticeable that the maximum expansion value, 0.072% (produced for the 2% sample after 180 days of curing), is lower than the maximum allowed value (0.1%) established by the ASTM C 1157 for non-expansive cements after 15 weeks. Thus, the different characterization techniques need to have a high level of sensitivity in order to characterize well the different degrees of damage studied in this work.

On the basis of these results, we were able to evaluate the effect of the presence of additional gypsum in comparison with the control series (0%). For this, two characteristic parameters (ϵ^{∞} and τ_{char}) were determined to describe the expansion curves (solid line in Fig. 3.2.3a) and to predict future trends (dashed line in Fig. 3.2.3a) for each series, using the equation proposed by Larive [28] and given below.

$$\epsilon(t) = \frac{\sigma}{K} + \epsilon^{\infty} \cdot \left(1 - e^{-\frac{t}{\tau_{char}}}\right) \tag{3.2.8}$$

Here, σ is the external force applied to the concrete element, K is the elastic modulus of the concrete, ϵ^{∞} is the maximum amplitude of the expansion, and τ_{char} is the characteristic time of the expansion reaction (influencing the slope of the curve). In this case, σ is 0 due to the non-existence of any force applied to the specimens, making null the first term of Eq. 3.2.8.

The fitted parameters according to Eq. 3.2.8 are summarized in Table 3.2.3. It is apparent that adding extra amounts of gypsum increases the characteristic time of the expansion reaction (τ_{char}) as well as increasing the amplitude of the expansion (ϵ^{∞}). From these results it is obvious that the percentages (of added SO_3) were very low, suggesting that the formation of ettringite is reduced. The value of ϵ^{∞} for the 1% series is only 0.025%, whereas it increased three times (0.072%) for the 2% series. This behaviour is due to the increase in the stress when the amount of ettringite formed surpasses the available pore volume for ettringite crystallization. Thus, a non-linear behaviour of the expansion with the added SO_3 has been obtained.

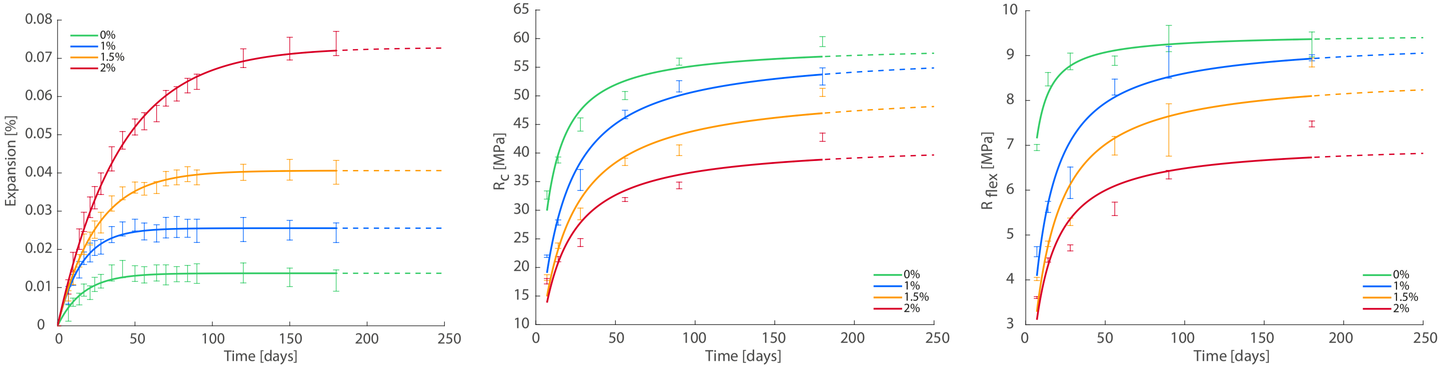

(a) **(b)** **(c)**

Figure 3.2.3: Results of physical tests for all series. Figure 3.2.3a shows the expansion undergone by the specimens. Each errorbar represents 6 measurements. Figure 3.2.3b shows the evolution over time of the compressive strength. Each errorbar represents 6 measurements. Figure 3.2.3c shows the evolution over time of the flexural strength. Each errorbar represents 3 measurements.

Figures 3.2.3b and 3.2.3c show the evolution of the compressive and flexural strengths. As the percentage of gypsum increases, not only does the cement hydration process slow down, but also different maximum values of the mechanical strength are achieved. After 180 days, in the case of the compressive strength, the 1%, 1.5% and 2% series reached values of 10%, 15%, and 20% less than the 0% series, respectively. However, in the case of the flexural strengths, the 1% and 1.5% series reach strengths only 3% and 4% lower. This indicates that the presence of sulphates generated a delay in the evolution of the strength, but without provoking significant structural damage. However, in the case of the 2% series, the compressive strength is 28% lower and the flexural strength is 20% lower than for the 0% series. In the ISA, the available sulphate is limited to that present in the cement and the added one. Consequently, as the reaction progress, the sulphate is consumed, and the concentration of sulphate into the pore solution decreases. This delays the evolution of the strength and conditions its maximum value but a great expansion is not achieved because sulphate is consumed, no further strength decrease is produced along the time. On the contrary, for ESA the available sulphate is not limited and consequently a continuous decrease in mechanical properties is observed during the attacking process [29].

Apart from the experimental results, the fitted models according to ACI [30] are represented. This standard establishes the curves of the evolution of the compressive strength versus the curing time for non-damaged series (Eq. 3.2.9).

$$R_c(t) = \frac{t}{\gamma + t} \cdot R_c^{\infty} \tag{3.2.9}$$

Here, R_c^{∞} is the ultimate compressive strength and γ is the age of concrete at which one-half of the ultimate compressive strength of concrete is reached. In this paper, we have employed the expression for both the compressive and flexural strength in order to model the curves. Note that the fit (measured by means of R^2 value) decreases in the case of the flexural strengths and for highest values of SO_3 (Table 3.2.3). Adding extra gypsum produces less compressive/flexural strength and an older age to reach that ultimate strength.

Table 3.2.3: Fitting parameters for expansion (according to Eq. 3.2.8) and for compressive and flexural strengths (according to Eq. 3.2.9) of mortars of the 0% (control), 1%, 1.5% and 2% SO_3 series.

	Expansion			Compressive strength			Flexural strength		
Series	ϵ^{∞} [%]	τ_{char} [days]	R^2	R_c^{∞} [MPa]	γ_c [days]	R^2	R_f^{∞} [MPa]	γ_f [days]	R^2
0%	0.013	16.00	0.939	59.00	6.79	0.944	9.48	2.27	0.940
1%	0.025	15.29	0.984	58.01	14.31	0.974	9.38	9.061	0.923
1.5%	0.040	24.76	0.994	51.42	17.11	0.944	8.60	11.32	0.883
2%	0.072	39.87	0.998	41.90	14.17	0.890	7.06	8.89	0.847

3.2.3.2 Microstructural tests

In order to estimate the ettringite formed in mortar specimens, an HRTG analysis and FESEM observations were performed. Thermogravimetric analysis is an instrumental technique that allows us to correlate mass change and temperature. In particular, due to the mass losses related to the thermal decompositions of the C-S-H (110°C–130°C) and ettringite (130°C–150°C) would overlap in the temperature domain using the traditional thermogravimetry test: in this research, a high-resolution thermogravimetric analysis was done. HRTG is based on a dynamic process which progressively changes the heating rate depending on the mass loss rate, allowing to separate the thermal decomposition events corresponding to the hydrated products from the Portland cement. It allows properly quantifying the mass loss related to the content of C-S-H and ettringite, as was done in previous studies [16, 31].

The results of the mass loss for the C-S-H and ettringite at 90 and 180 curing days for each series are set out in Table 3.2.4. In general, there can be seen an increase in the ettringite and a decrease in the mass loss associated to the C-S-H content with time (90 to 180 days) for all series: the more SO_3 content is added, the more the ettringite formation increases with time. The decrease in the C-S-H with the SO_3 supports the mechanical results: as the C-S-H content increases, better mechanical behaviour ensues. In the case of the 2% series, the C-S-H formation at 180 days breaks up the general trend of all series: it did not decrease as the SO_3 content rose, maybe caused by the fact that the rate of the chemical reactions of the matrix through time are different when the gypsum content in the initial mix is relatively high.

The FESEM observations were taken after 90 days of curing for all series. Representative micrographs are shown in Figure 3.2.4. Figure 3.2.4a shows the C-S-H and portlandite phases, without noticeable ettringite crystals in the 0%

Table 3.2.4: Mass loss (in percent) related to C-S-H and ettrigite decomposition peaks in the HRTG analysis for each series.

	C-S-H		Ettringite	
Series	90 days	180 days	90 days	180 days
0%	4.68	4.60	3.22	3.41
1%	4.42	4.10	3.79	4.08
1.5%	4.41	4.07	3.81	4.17
2%	4.25	4.24	4.00	4.45

series. In Figures 3.2.4b and 3.2.4c (1% and 1.5% series, respectively), needles of ettringite are identified together with portlandite crystals and C-S-H gel. Lastly, a micrograph of the 2% series is shown in Figure 3.2.4d. In this image, a large amount of ettringite needles surrounding the C-S-H gel and portlandite can be seen. The observations from these micrographs support the ettringite content found in the HRTG.

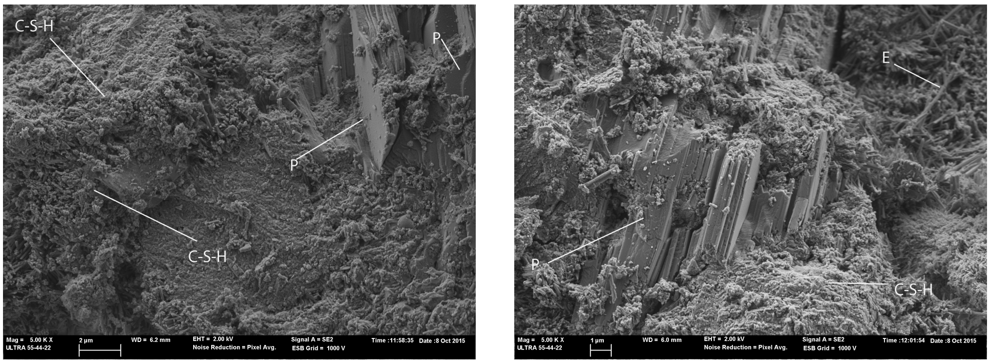

(a) 0% series **(b)** 1% series

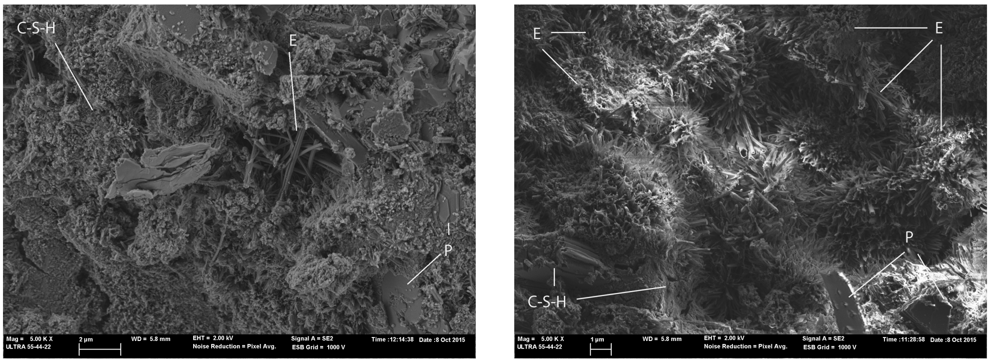

(c) 1.5% series **(d)** 2% series

Figure 3.2.4: FESEM images for the ISA series taken after 90 days of curing: 3.2.4a 0% series, 3.2.4b 1% series, 3.2.4c 1.5% series, 3.2.4d 2% SO_3 series. Note that all of them were taken with the same magnification (5000×). (key: C-S-H: calcium silicate hydrate, E: ettringite, P: portlandite).

3.2.3.3 Non-Destructive tests

Impact resonance acoustic spectroscopy

The dynamic modulus (E_{dyn}) was calculated from the fundamental transverse frequency obtained from the impact resonance acoustic test (ASTM C215 - 14 [24]). This parameter was monitored in order to follow the evolution of the stiffness for all series (Fig. 3.2.5a). The 0% series presented a normal stiffness evolution due to the lack of additional gypsum in the initial mix. This allows the matrix to evolve quickly, as the mechanical results suggested in the previous section (Section 3.2.3.1). The 1% and 1.5% series experience a slowdown process in the evolution of the E_{dyn} parameter due to the delay effect in the hydration process of the cement matrix caused by the addition of gypsum. However, the values of E_{dyn} for these two series converged after 180 days to the value obtained for the 0% series. This behaviour means that an expansion under 0.04% has no significant effect on E_{dyn}. Interestingly, the 2% series showed a similar trend, with E_{dyn} increasing with the curing time. However, in contrast to the findings for the other series, the maximum value of E_{dyn} was significantly lower. Figure 3.2.5b shows the relation between the normalized dynamic modulus and the expansion experienced by the specimens. The derivative of each expansion curve has been calculated, in order to remove points with no increase in the expansion from the linear fit plot (the expansion process stopped; removed experimental points are marked as filled symbols). In this graph, the change in the slope of the different series can be clearly observed, showing a clear relation between the gain in stiffness of the series as the ISA progresses.

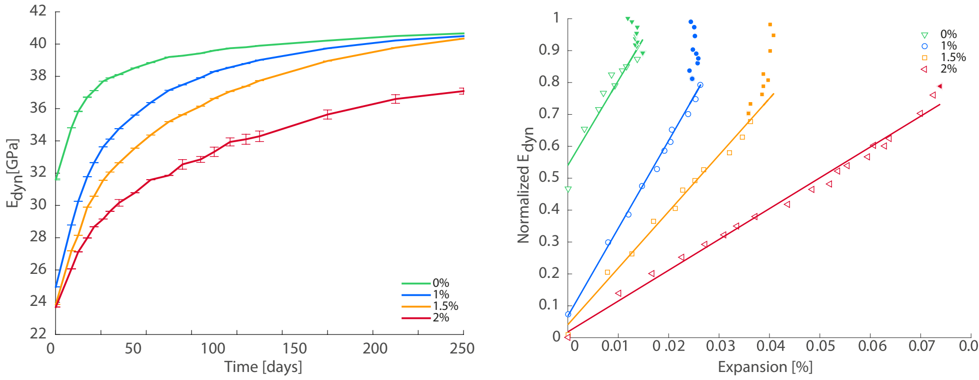

(a) **(b)**

Figure 3.2.5: Results of impact resonance acoustic spectroscopy tests for all series. Figure 3.2.5a: the evolution of the dynamic modulus. Each errorbar represents 30 measurements. Figure 3.2.5b: the relation between the normalized dynamic modulus (calculated by means of the ratio between the dynamic modulus for a given test time and the dynamic modulus value reached after 180 days) and the expansion experienced by the specimens. The derivative of each expansion curve has been calculated in order to remove from the linear fit plot those experimental points for which there was no increase in the expansion (filled scatters).

In the case of the 0% and 1% series, the slope of the linear fit is equal, but the regression for the 0% series starts at higher values due to the quick gain in stiffness. However, the 1.5% and 2% series decrease their slopes, indicating a loss of speed in the curing process. A normalization with respect to the maxima of all values of E_{dyn} was necessary in order to make an accurate analysis of the geometry of the fitting for all series.

This behaviour demonstrates that there is no relation between the evolution of the dynamic modulus and the expansion of the material due to the internal sulphate attack. Probably a low level of a microcracking process is not easily identified by means of the impact resonant acoustic technique, due to the non-activation of micro-cracking process typical of high stage damaging process in ISA. Nonetheless, the 2% series did not reach the same values of E_{dyn}, due to the large amount of gypsum added in the initial mix and, consequently, the large amount of ettringite formed in the hydrated cement matrix. For high levels of damage, the impact resonant acoustic technique is suitable.

Ultrasonic measurements

The computation of the ultrasonic velocity v_p, proportional to the mechanical constants of the material, basically consists in the estimation of the time arrival t_a. Figure 3.2.6a shows the initial part of the signals, taken at 90 days. It can be observed that the time of flights for different series are different, producing a systematical phase difference in the time domain signals. This change in t_a makes the propagation velocity decrease when the SO_3 content in the original mix increases. Figure 3.2.6b shows the average values of the ultrasonic wave velocity for each series at different testing times. The trend of the resulting curves is closely correlated with the evolution of the stiffness of the materials due to the setting and curing process of the concrete plus the addition of an extra amount of gypsum. Therefore, this measure is able to characterize each series both in terms of the rate of reaching a stable value, and the maximum ultrasonic wave velocity.

During the hydration of Portland cement, different hydrates are formed. C-S-H gel is the most important hydrate in terms of the strength development.

The gel particles formed connect to other gel particles, or to other hydrates, or to aggregate particles, reducing the porosity and increasing the solid network. This behaviour is confirmed through the ultrasonic attenuation measurements. Figure 3.2.7a shows the time-domain signals for the 0% and 2% series at 90 days. In this plot, the differences in the amplitudes of the signals of both series can be observed, making more evident the contrast in the intensity of the wave at higher frequencies, where the 0% series has more cohesive elements in its structure than the 2% one.

The received signals were analysed in terms of their energy according to Eq.3.2.4. Attenuation of the signals were calculated according to Eq. 3.3.5. The total material attenuation values, α_{mat}, observed for the different mortars are depicted in Figure 3.2.7b. The general trend of the attenuation values is a decay

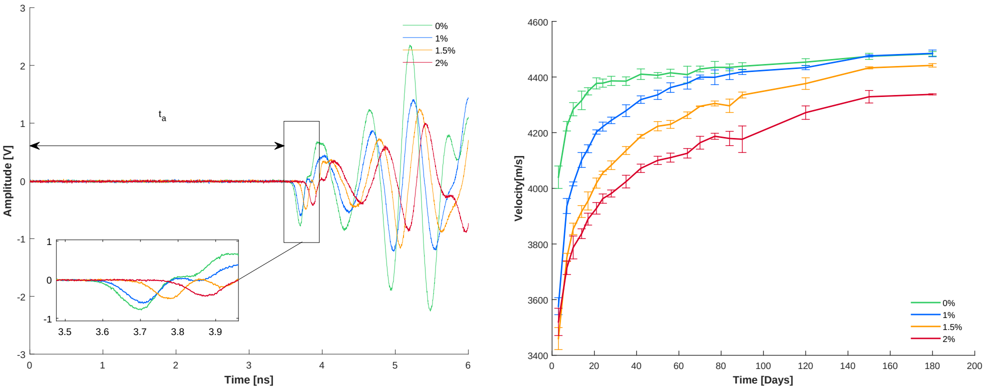

(a) **(b)**

Figure 3.2.6: Results of ultrasonic pulse velocity test for all series. Figure 3.2.6a: the beginning of time-domain signals at 90 days and time of flight (t_a) concept. Figure 3.2.6b: the results of the ultrasonic pulse velocity. Each data point represents the mean of three measurements.

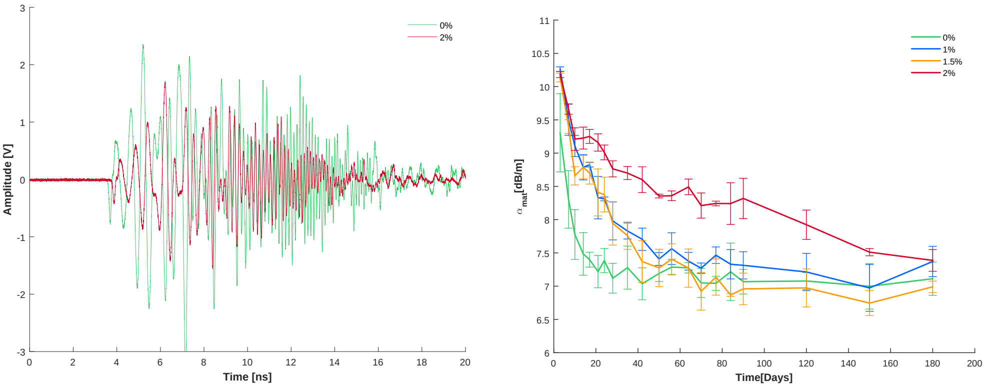

(a) **(b)**

Figure 3.2.7: Results of ultrasonic attenuation test for all series. Figure 3.2.7a: the time-domain signals for the 0% and 2% series at 90 days. Figure 3.2.7b: the total material attenuation obtained by means of a linear chirp signal. Each data point represents the mean of three measurements.

as the hydration process of the Portland cement matrix progresses. The reference series (0%) can only be distinguished from the 1% and 1.5% series in the initial steps of the process. The decrease in attenuation for 0% series is due to the densification of the matrix and the increasing in the number of contact points and contact surface area. This attenuation decrease is produced in the first 28 days, from 5.5 dB/cm to 4.1 dB/cm, suggesting that the ultrasonic wave transmission is achieved by means of the contact area among the gel and the different types of particles (other hydrates, unhydrated particles, or sand particles). The effect in the 1% and

1.5% series of the addition of SO_3 as gypsum produces a delay in the development of the solid network: the initial attenuation is 6 and 6.5 dB/cm, and after 28 days, this was reduced to 4.5 dB/cm, both reaching the same value. After this curing age, the evolution of the attenuation for both materials is similar to those found for 0% series. Nevertheless, the 2% series presents huge differences from the other series, remaining higher along the whole process. Thus, attenuation values after 28 days higher than 5 dB/cm and 5.5 dB/cm are reached after 60 days, oscillating until 80 days. After 90 days, the attenuation begins to decay until reaching values near those from the 1% and 1.5% series at 180 days, when the expansion process seems to stop (at 0.08% expansion, Fig. 3.2.3a).

The attenuation showed similar trends to the rest of the monitored parameters for all series, but it seems to be more sensitive to the mesoscale elements in the mortar structure rather their elastic constants, constituting an interesting way to evaluate damage processes in non-homogeneous materials like concrete.

3.2.4 Conclusions

In this paper, there were presented the results of monitoring an internal sulphate attack (ISA), which was exhaustive in terms of the number of measurements taken along the the experiment (180 days) as well as the number of methods used in order to characterize the process. Four types of mortar with different amounts of gypsum have been monitored by means of physical, microstructural and non-destructive tests. The experiment had been designed to reach low expansion rates ($\leq 0.1\%$ of expansion) in order to examine the sensitivity of the applied techniques.

The physical tests were to determine the expansion and mechanical strength parameters. The expansion analysis has shown the suitability of the fitting model proposed in the bibliography, increasing the slope of the expansion process (τ_{char}) and maximum expansion rate (ϵ^{∞}) as the SO_3 content of the series rises. In the mechanical analysis, the series reached lower values of R_c and R_f as the gypsum content increases.

HRTG allowed qualitatively identifying the amount of expansive products formed during the whole process: the ettringite formed in the series rises as the initial amount of gypsum increases and the curing time advances. FESEM micrographs showed the needles of ettringite surrounding the C-S-H and portlandite phases for the high gypsum content series.

Impact acoustic resonance spectroscopy and ultrasonic measures have shown the accuracy of these non-destructive techniques applied to detect and characterize an ISA process. The dynamic modulus and ultrasonic pulse velocity have closely predicted the stiffness of the specimens, according to the aforementioned trends. However, the total material attenuation presented different trends, showing clear differences between the 2% SO_3 series and the rest of the series, reaching similar values at the end of the experiment. The attenuation monitoring is an interesting procedure for the assessment of low-level expansion processes in mortars which have suffered an internal sulphate attack.

Acknowledgements

This work has been supported by the Spanish Administration under grants TEC2011-23403, BIA2014-55311-C2-1-P and BIA2014-55311-C2-2-P.

References

[1] M. Katsioti, N. Patsikas, P. Pipilikaki, N. Katsiotis, K. Mikedi, and M. Chaniotakis, "Delayed ettringite formation (DEF) in mortars of white cement," *Construction and Building Materials*, vol. 25, no. 2, pp. 900–905, Feb. 2011.

[2] J. Skalny and J. Marchand, *Sulphate attack on concrete*. Spon Press, 2002.

[3] H. Taylor, *Cement Chemistry*. Thomas Telford, 1997.

[4] M. Collepardi, "A state-of-the-art review on delayed ettringite attack on concrete," *Cement and Concrete Composites*, vol. 25, pp. 401–407, 2003.

[5] I. Casanova, L. Agulló, and A. Aguado, "Aggregate expansivity due to sulfide oxidation - I. reaction system and rate model," *Cement and Concrete Research*, vol. 26, pp. 993–998, 1996.

[6] A. Pavoine, X. Brunetaud, and L. Divet, "The impact of cement parameters on delayed ettringite formation," *Cement and Concrete Composites*, vol. 34, no. 4, pp. 521–528, 2012.

[7] A. Pavoine, L. Divet, and S. Fenouillet, "A concrete performance test for delayed ettringite formation: Part I optimisation," *Cement and Concrete Research*, vol. 36, no. 12, pp. 2138–2143, 2006.

[8] Y. Zhou, M. Li, L. Sui, and F. Xing, "Effect of sulfate attack on the stress-strain relationship of FRP-confined concrete," *Construction and Building Materials*, vol. 110, pp. 235–250, 2016.

[9] H. Nuri-Atahan and K. Mehmet-Arslan, "Improved durability of cement mortars exposed to external sulfate attack: The role of nano & micro additives," *Sustainable Cities and Society*, vol. 22, pp. 40–48, 2016.

[10] J. Małolepszy and E. Grabowska, "Sulphate attack resistance of cement with zeolite additive," *Procedia Engineering*, vol. 108, pp. 170–176, 2015.

[11] W. Piasta, J. Marczewska, and M. Jaworska, “Durability of air entrained cement mortars under combined sulphate and freeze-thaw attack,” *Procedia Engineering*, vol. 108, pp. 55–62, 2015.

[12] J. Stroh, B. Meng, and F. Emmerling, “Monitoring of sulphate attack on hardened cement paste studied by synchrotron (XRD),” *Solid State Sciences*, vol. 48, pp. 278–285, 2015.

[13] J. Yuan, Y. Liu, Z. Tan, and B. Zhang, “Investigating the failure process of concrete under the coupled actions between sulfate attack and drying-wetting cycles by using X-ray (CT),” *Construction and Building Materials*, vol. 108, pp. 129–138, 2016.

[14] V. M. Maholtra and N. J. Carino, Eds., *Handbook on Non destructive Testing on Concrete*. CRC Press, 2004, vol. 1.

[15] Y. Zhou, J. Gao, Z. Sun, and W. Qu, “A fundamental study on compressive strength, static and dynamic elastic moduli of young concrete,” *Construction and Building Materials*, vol. 98, pp. 137–145, 2015.

[16] V. Genovés, L. Soriano, M. Borrachero, J. Eiras, and J. Payá, “Preliminary study on short-term sulphate attack evaluation by non-linear impact resonance acoustic spectroscopy technique,” *Construction and Building Materials*, vol. 78, pp. 295–302, 2015.

[17] T. P. Philippidis and D. G. Aggelis, “Experimental study of wave dispersion and attenuation in concrete,” *Ultrasonics*, vol. 43, no. 7, pp. 584–595, 2005.

[18] S. Popovics, J. L. Rose, and J. S. Popovics, “The behaviour of ultrasonic pulses in concrete,” *Cement and Concrete Research*, vol. 20, no. 2, pp. 259–270, 1990.

[19] L. Vergara, J. Gosálbez, J. V. Fuente, R. Miralles, and I. Bosch, “Measurement of cement porosity by centroid frequency profiles of ultrasonic grain noise,” *Signal Processing*, vol. 84, no. 12, pp. 2315–2324, 2004.

[20] L. Vergara, R. Miralles, J. Gosálbez, F. J. Juanes, L. G. Ullate, J. J. Anaya, M. G. Hernández, and M. A. G. Izquierdo, “NDE ultrasonic methods to characterise the porosity of mortar,” *NDT & E International*, vol. 34, no. 8, pp. 557–562, 2001.

[21] D. G. Aggelis and T. P. Philippidis, “Ultrasonic wave dispersion and attenuation in fresh mortar,” *NDT & E International*, vol. 37, no. 8, pp. 617–631, 2004.

[22] ASTM, “Standard test method for length change of hydraulic-cement mortars exposed to a sulfate solution,” ASTM C 1012-04, 2004.

[23] M. V. Borrachero, J. Payá, M. Bonilla, and J. Monzó, "The use of thermogravimetric analysis technique for the characterization of construction materials," *Journal of Thermal Analysis and Calorimetry*, pp. 503–509, 2008.

[24] ASTM, "Standard test method for fundamental transverse, longitudinal, and torsional resonant frequencies of concrete specimens," American Society for Testing Materials, ASTM C 215-14, 2014.

[25] J. Krautkrämer and H. Krautkrämer, *Ultrasonic testing of materials*. Springer-Verlag, 1983.

[26] P. A. Gaydecki and F. M. Burdekin, "The propagation and attenuation of medium-frequency ultrasonic waves in concrete: a signal analytical approach," *Measurement Science and Technology*, vol. 3, p. 126, 1992.

[27] M. Molero, I. Segura, S. Aparicio, M. G. Hernández, and M. A. G. Izquierdo, "On the measurement of frequency-dependent ultrasonic attenuation in strongly heterogeneous materials," *Ultrasonics*, vol. 50, no. 8, pp. 824–828, 2010.

[28] C. Larive, *Apports combinés de l'expérimentation et de la modélisation à la compréhension de l'alcali-réaction et de ses effets mécaniques*. Etudes etrecherches des LPC., 1998.

[29] M. Zhang, M. Jiang, and J. Chen, "Variation of flexural strength of cement mortar attacked by sulfate ions," *Engineering Fracture Mechanics*, vol. 75, no. 17, pp. 4948–4957, 2008.

[30] ACI-Committee-209, "Prediction of creep, shrinkage, and temperature effects in concrete structures," *American Concrete Institute Especial publication*, vol. 76, pp. 193–300, 1982.

[31] M. V. Borrachero, J. Payá, and J. Monzó, "The use of maxres for the investigation of partially hydrated portland cement systems," *Usercom*, pp. 6–15, 2000.

3.3 Non-linear acoustic spectroscopy and frequency sweep ultrasonics: Case on thermal damage assessment in concrete[7]

---

[7] *V. Genovés, A. Carrión, D. Escobar, J. Gosálbez, J. Monzó, M.V. Borrachero, and J. Payá. "Non-linear acoustic spectroscopy and frequency sweep ultrasonics: Case on thermal damage assessment in concrete," Journal of Nondestructive Testing (Submitted).*

Abstract

An exhaustive thermal damage of Portland cement-based materials is addressed. Different temperatures between 40 °C and 525 °C were monitored by means of microstructural, physical and non-destructive tests. Microstructural analysis (Thermogravimetry and Scanning Electron Miscroscopy) showed the principal changes of the Portland cement hydrated products for the different analysed temperatures. Compressive and flexural strength results remained constant or even increased at a low temperatures meanwhile the mass loss increases. Dilatometry results revealed important information about deformation incompatibilities between the paste and the aggregate. These results have been correlated with non-destructive tests: non-linear impact resonance acoustic spectroscopy and ultrasonic measures. The dynamic modulus and ultrasonic pulse velocity have closely predicted the linear stiffness decay of the specimens. However, non-linear parameter exhibited different trend from stiffness-related parameters, keeping constant until 250 °C and performing a huge increasing for 400 and 525 °C. Ultrasonic attenuation computed with a broadband ultrasonic signal (chirp) unveiled true information about scattering components inside the material, being sensitive to interfacial transition zone between aggregate and paste in a large range of frequencies. The correlation between microstructural, mechanical and non-destructive techniques were carry out successfully, being non-linear vibration and ultrasonic attenuation a non-conventional parameters that gave a lot of information about a complex damage process like thermal attack in highly heterogeneous materials like Portland cement composites.

3.3.1 Introduction

Owing to the good performance against high temperatures, concrete is the most used material in fire-resistant structures in civil and building engineering. Because of its great thermal inertia and insulating properties, concrete protects steel bars from fire and keeps its mechanical properties in relatively good condition [1].

Despite the goodness of this material, the cement paste that assembles the sand particles and coarse aggregates losses stiffness gradually and adhesion capacity when the temperature is significantly high. Several studies were performed in the past evaluating mechanical properties and general behaviour of concrete under high temperatures, assessing compressive and flexural strength, modulus of elasticity, stress-strain relationship and physical and chemical changes mainly. There are several factors that influence the aforementioned parameters of concrete affected by high temperatures. Water evaporation is the first mechanism of change due to the cementing matrix lose their free water from capillary network and physically absorbed water from surface of cementing C-S-H gel completely. At higher temperatures (105 °C), it start to lose the chemically bonded water from hydrated compounds. Most of the capillary water is lost at 400 °C. The hydration products plays an important role in cement paste degradation. From 105 °C to 300 °C a continuous mass loss due to the ettringite, C-S-H and C-A-H decomposition occurs, bringing a stiffness decay of the material but keeping the compressive strength almost intact. From 400 °C to 525 °C decomposition of Portlandite occurs (yielding lime CaO), decreasing stiffness without affecting directly to compressive strength of the cement paste. However, if cement paste is water cooled after exposure to high temperature, the rehydration of lime will cause a great reduction of strength due to a considerable expansion owing to such hydration reaction [2, 3].

Nevertheless, not only the loss of water plays an important role in thermal damage in concrete. According to some studies, the incompatibility of deformations between the cement paste and the aggregates is essential to understand the decay of performance of elements made by concrete at high temperatures [4]. Limestone and quartz aggregates expands until 573 °C in a linear way. After that, quartz experiments a great expansion due to the the transformation from α-quartz to β-quartz [5]. Limestone aggregates performs less expansion than quartz ones and maintain the same phase until its decomposition at 700 °C. However, cement paste expands slightly until 200 °C, but, beyond these threshold, starts to shrink rapidly due to the loss of combined water. Such difference in strain behaviour develop an aggressive microcracking stage, damaging the interfacial transition zone between the cement paste and aggregates, even reaching to completely disconnect the aggregate from the paste. It is evident that the general behaviour of a structural element will be conditioned to the design of the concrete and its boundary conditions: Water/binder ratio, moisture, type of aggregates, cement type and fiber inclusion are the most influencing variables in concrete durability against high temperature [2, 3].

Because of the multiple causes that can affect the integrity of concrete under thermal damage situation (and other kind of physical and chemical damages), scientific communities are focused in the development of Non-Destructive Testing (NDT) techniques due to its robustness and non-invasive nature. NDT can help to determinate the internal state of concrete structures *in-situ* or from extracted cores from pillars, walls or beams among others. These techniques are classified according to the method for measuring the target scope of the structure. Beggining from mechanical waves, there are techniques for the purpose of overall inspection (ultrasonic, impact echo) and techniques for the purpose of surface evaluation (Schmidt rebound hammer, Windsor probe, and spectral analysis of surface acoustic waves) [6]. Other techniques focus on the response of specific points by obtaining concrete samples from different locations (small-scale mechanical testing, differential thermal analysis, thermogravimetric analysis, scanning electron microscopy or thermoluminescence analysis among others). Some of these techniques are appropriate for *in-situ* test, but it is hard to use these (e.g., ultrasonic pulse velocity, Schmidt rebound hammer, Windsor prove, or impact echo) to characterize mesoscopic defects in global damage case. Others (e.g., differential thermal analysis, thermogravimetric analysis, scanning electron microscopy) can sensitively evaluate contact-type defects, but involve either time-consuming processes or limited potential for laboratory experiments due to their location.

Non-linear Elastic Waves Spectroscopy (NEWS) [7, 8] techniques such as Non-linear Resonant Ultrasound Spectroscopy (NRUS) [9] or Non-linear Impact Resonance Acoustic Spectroscopy (NIRAS) [10] can evaluate the non-linearity and hysteresis by analysing the relationship between the amplitude of excitation and the frequency response of a granular material. They offers an interesting information about the mesoscopic defects in complex global damage cases like thermal damage, where a different degradation mechanisms take place at the same time (stiffness loss, incompatibility of deformations...) with an accessible and common equipment [11, 12]. Besides resonant techniques, ultrasonic attenuation and pulse velocity measurements can also be performed in the field with a relatively simplicity and gives a lot of information about the stiffness of the material and the scattering components. Such variables becomes essential to evaluate thermal damage on concrete, giving information about multiple processes inside the concrete elements [13–17] .

The scope of this paper is to evaluate thermal damage by means of NDT and destructive tests on normalized mortar specimens at different temperatures in order to distinguish the different degradation mechanisms. Besides, a correlation between NDT results and microstructural and physical tests will be carried out. The demonstration of the suitability of NIRAS and broadband frequency ultrasonic analysis as a non-invasive techniques will bring the opportunity to accurately analyse thermal damage in heterogeneous materials without compromising its integrity.

The remainder of the paper is organized as follows: In Section 3.3.1 thermal damage in concrete, used NDT techniques and the scope of the paper had been described. Description of the materials, layout and the explanation of the techniques are addressed in Section 3.3.2. The results and correlation between the exposed techniques are founded in Section 3.3.3. Finally, in Section 3.3.4 the conclusions of the study are presented.

3.3.2 Experimental

3.3.2.1 Materials and specimens

Six mixes of standardized (UNE EN 196-1:2005) Portland cement mortar (water/cement = 0.5) made of 450 g of Spanish cement CEM I-52.5-R, 1350 g of 0/2 mm crushed quartz sand and 225 g of water were carried out in order to obtain eighteen 40 × 40 × 160 mm^3 specimens to perform the present study. Each mix of three specimens was used to reach the different temperatures of thermal damage. After the mixing process, iron moulds were stored in the wet chamber (20 °C and 100 % H.R.) for 24 hours, then, the mortar pieces were released and stored in the wet chamber again for 60 days in order to reach elastic properties stabilization stage. Afterwards, specimens were dried to constant mass at 40 °C for 7 days and wrapped with plastic film until reached room temperature again in order to characterise them in its pristine state. Thermal damage protocol was designed according to mass loss due to the decomposition of bonded water. A previous thermogravimetric (TG) analysis was undertaken in order to fix the analysis temperatures.

Figure 3.3.1 shows the derivative TG curve for a 0.5 w/c cement paste. Analysed temperatures were established according to the beginning and ending of principal mass loss from the hydration products in the thermogram, thus, 90 ,150, 250, 400, 525 °C were selected. The analysis stopped in 525 °C due the phase change in silica sand to β-phase that brings the aggressive expansion of quartz. A programmable oven was used to damage the mortar bars, increasing the temperature at 3 °C /min rate until the desired temperature was reached. After that, the temperature was maintained during 3 hours, then, the oven was switched off and cooled slowly during 24 hours.

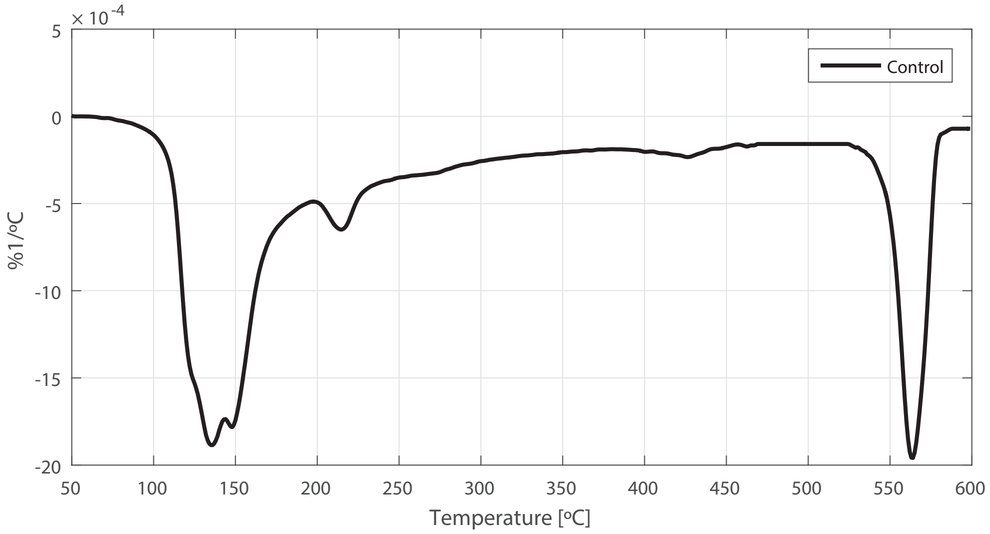

Figure 3.3.1: DTG curve of a cured of 0.5 water to cement paste used select the analysed temperatures.

3.3.2.2 Microstructural tests

These analyses were carried out on the pastes, which had the same dosage as the mortars, excluding the sand. The thermogravimetry tests were performed in order to support the chemical decomposition of hydrated products for all analyzed temperatures. In order to carry out this analysis, portions of the paste samples were taken and pulverized with an agate mortar, adding a small amount of acetone. The solid was filtered and dried at 60°C for 15 min. The equipment used was an ultra-balance Mettler TGA 850. Sealed aluminium crucibles of 100 ml were used, each with a micro-holed lid to create a water vapour self-generated atmosphere [18]. The analysis was carried out in a dry nitrogen atmosphere with a gas flow of 75 mL/min and a temperature interval of 35°C–600°C. For conventional thermogravimetric analysis with 10°C/min heating rate was selected. The main decomposition DTG peak related to the calcium silicate hydrates is recorded in 110°C–130°C, that for the ettringite within the 140°C–150°C range, and those for the calcium aluminosilicate and calcium aluminate hydrates within the 210°C–220°C range [19]. Portlandite decomposition occurs between 500°C–600°C.

For the FESEM observations, portions of the paste and mortar submitted to 40 °C and 525 °C samples were taken, drying at 60°C and coating them with a carbon layer. A ZEISS (ULTRA 55) electron microscope was used, setting it to voltages of 2–3 kV and to distances between 3.9 mm and 6.0 mm.

3.3.2.3 Mechanical tests

Mechanical tests were performed in order to monitor the thermal damage process and correlate the destructive and conventional parameters with the non-destructive ones. For the mechanical tests (determining the compressive and flexural strengths) an universal testing machine was used (INSTRON model 3382) following the Spanish standard UNE-EN-196. For each analyzed temperature, three specimens were tested by means of three-point bending tests, and the six obtained semi-prisms were used to determine the compressive strength.

3.3.2.4 Dilatometry tests

A test to obtain the linear deformation of the pastes and mortar were performed. The equipment used for this experiment was an absolute dilatometer NETZSCH model 402-C, which was calibrated with a sapphire pattern. Special samples of mortar and paste of $10 \times 10 \times 60$ mm^3 were used for this test. After the curing process, the samples were polished to the appropriate geometry for the dilatometer equipment ($5 \times 5 \times 30$ mm^3) and then dried during four days at 45 °C. The thermal increment rate was 5 °C /min.

3.3.2.5 Non-destructive tests measurements

Non-linear spectroscopy

NIRAS method is a relatively new NDT technique which can detect changes in materials from the resonance frequency shifts of the vibrational modes of a specimen as the impact energy increases. This change is simply due to the non-linearity of the material. This technique has been shown to be highly high sensitivity to material defects, specifically to the microcracks of the material [10, 11]. It is well-known that defects in a material can be detected from the vibrational frequency resonance values of a specimen made of that material. Distributed cracks reduce the stiffness of the specimen, and therefore, the natural frequency of the structural element made of that material. Besides this linear effect, cracks also change non-linear properties of the material making an imperfect matrix and non-homogeneity zones that increment some mesoscopic effects. This kind of imperfections trigger non-linear effects such as change of the frequency when the impact energy is increased, non-linear modulation of two waves and scalability loss. This distortion of the elastic waves is responsible for the change in the observed resonance frequency in NIRAS tests, which can be described as a non-linear hysteretic macroscopic behaviour of the material itself.

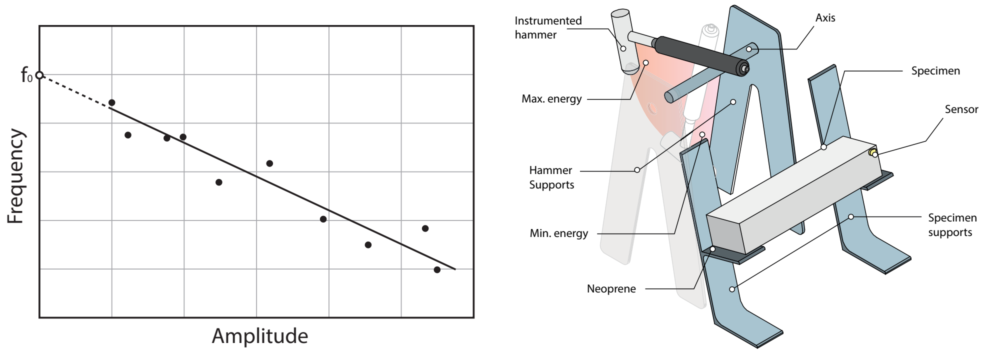

(a) (b)

Figure 3.3.2: Graphic information about vibrational setup and non-linear parameter calculation. Figure 3.3.2a Amplitude versus Frequency scheme for α calculation. Figure 3.3.2b Vibrational layout.

Two parameters were obtained with this layout. Dynamic moduli (E_{dyn}) calculated following the expressions in the ASTM C215-14 with the linear frequency, and non-linear parameter α related to frequency shift with the increase of the amplitude excitation. To calculate the non-linearity of a single specimen, ten impacts in an increasing amplitude were applied. From each vibrational signal, fundamental frequency, f_i and its resonant amplitude, A_i were extracted (Fig. 3.3.2a). The linear frequency, f_0, is obtained from the intersection with the y-axis at a virtual 0 amplitude of a linear regression on a A_i versus f_i plot of the ten impacts [11]. Once the f_0 is determined, frequencies for each impact were normalized by the linear frequency and the linear regression of the normalized frequency versus amplitude is recomputed in order to obtain the slope as α value (Eq. 3.3.1).

$$\frac{f_0 - f_i}{f_0} = \alpha \cdot A_i \tag{3.3.1}$$

Acoustic resonance tests were performed with the setup presented in Figure 3.3.2b. An impact hammer (Brüel & Kjær 8206-003) was attached to an axis, located in a metallic structure. This axis, supported on two ball bearings, yields a free rotational motion in one plane with minimum friction. The specimen was located in the metallic supports, slightly sloping, positioned for impact in the center of the face and perpendicular to the axis of greater inertia of its cross section. In the opposite top-left corner, a piezoelectric accelerometer sensor (PCB 352A21, 0.956 mV/m/s^2 sensitivity) was attached in order to obtain the vibrational motion of the test probe. The electric signal of the instrumented hammer and the accelerometer go through a signal conditioner (PCB 482A18) polarizing it and transmitting it to the oscilloscope (Tektronics MDO3014). The oscilloscope was configured to optimize the signal acquisition and processing with f_s equals to 250 kHz, N equals 10000 samples (40 ms acquisition time), trigger voltage equals to 120 mV and pre-trigger time equals to 4 ms. Finally, the information was transmitted via USB to a computer with a control software developed by the authors.

Ultrasonics

Ultrasonic techniques have been use widely for materials characterization and defects detection. A detailed analysis of the velocity and attenuation of the injected wave has been carried out in this study by means of broadband signals. Velocity is a well studied ultrasonic parameter that is directly related with the stiffness of the material. However, attenuation phenomenon is close related to the scattering media, being proportional to the injected frequency and the quantity and size of the elements of the specimen that may cause reflection, absorption and dissipation of the energy of the wave travelling through the media. The development of defects during a damage process in the material as debonding elements, micro-cracks or voids will distort noticeably the geometry of the wave, and consequently, its energy.

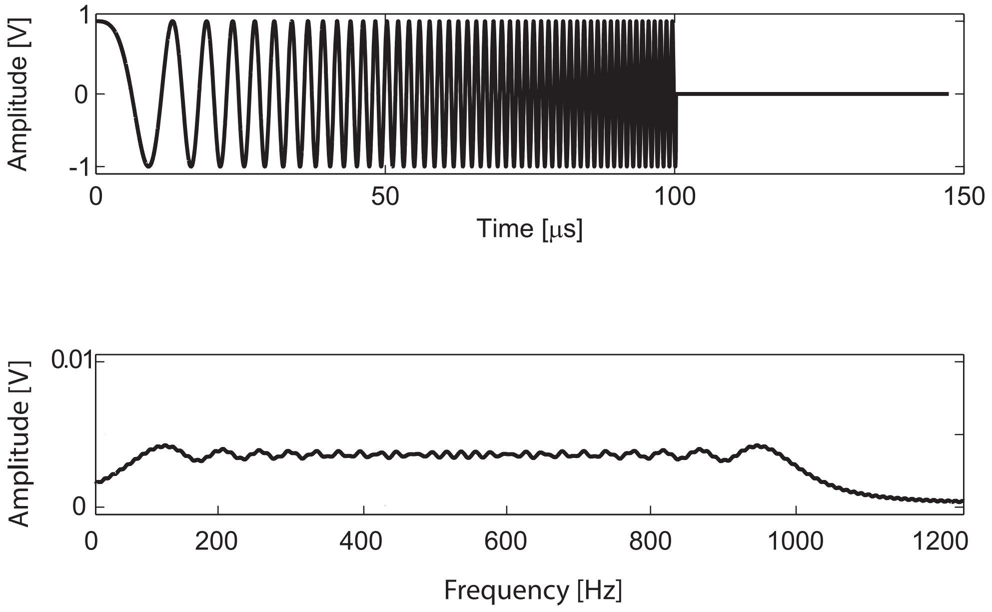

Figure 3.3.3: Emitted signal in time and frequency domain.

In Figure 3.3.3, the transmitted swept-frequency signal (chirp) $s_{tx}(t)$ can be observed. The mathematical expression of a linear chirp signal is

$$s_{tx}(t) = A_{tx} \sin\left(2\pi f_{min} t + \pi \Delta f_{max} t^2\right) \cdot rect\left(\frac{t - \frac{T}{2}}{T}\right) \tag{3.3.2}$$

$$\Delta f_{max} = \frac{f_{max} - f_{min}}{T} \tag{3.3.3}$$

where A_{tx} is the amplitude of the signal, t is the time, f_{min} is the fundamental frequency, T is the active time of the signal, and Δf_{max} controls the maximum frequency ($f_{max} = f_0 + T\Delta f_{max}$) which is reached at T seconds (Eq. 3.3.3). For this work and for the selected parameters are $A_{tx} = 1$ V, $f_0 = 100$ kHz, $f_{max} = 1$ MHz and $T = 100\mu s$.

The estimated ultrasound parameters are the wave velocity and the total attenuation of the material. The propagation velocity (or UPV), v_p, is obtained as the ratio between the length of the specimen, d_{mat}, and the signal time arrival, t_a (Eq. 3.3.4). The signal time arrival, t_a, was taken when the level of received signal exceeded 50% of the noise level.

$$v_p[m/s] = \frac{d_{mat}}{t_a} \tag{3.3.4}$$

The ultrasonic wave attenuation due to the material, $\alpha_{mat}(f)$, is calculated as the difference between the transmitted and received energies, taking into consideration the effect of the equipment and the distance travelled (Eq. 3.3.5).

The mathematical expression of the spectrum of the transmitted chirp signal attends to Eq. 3.3.6, and allows estimating $\alpha_{mat}(f)$ by applying Eq. 3.3.5 directly.

$$\alpha_{mat}(f) = \frac{10 \cdot log\left(S_{tx}(f)\right) - 10 \cdot log\left(S_{rx}(f)\right) - \alpha_{equip}(f)}{d_{mat}} \tag{3.3.5}$$

$$\begin{aligned} S_{tx}(f) = \Bigg| \frac{A_{tx}}{\sqrt{2\Delta_{f_{max}}}} e^{-j\pi(f-f_0)^2} \Bigg[C\left(\sqrt{2}\frac{f-f_0}{\sqrt{\Delta_{f_{max}}}}\right) + jS\left(\sqrt{2}\frac{f-f_0}{\sqrt{\Delta_{f_{max}}}}\right) \\ - C\left(\sqrt{2}\frac{\Delta_{f_{max}}T + f - f_0}{\sqrt{\Delta_{f_{max}}}}\right) - jS\left(\sqrt{2}\frac{\Delta_{f_{max}}T + f - f_0}{\sqrt{\Delta_{f_{max}}}}\right)\Bigg]\Bigg|^2 \end{aligned} \tag{3.3.6}$$

where $C(x)$ and $S(x)$ are the Fresnel integrals (Section 2.3.3.3). The received energy spectral density is computed as Eq. 3.3.7, where $X(f)$ (Eq. 3.3.8) is the

Fourier Transform of signal $s_{rx}(t)$. As shown in Figure 3.3.3, the spectrum of the transmitted pulse is distributed along a frequency bandwidth. At the expense of decreasing the Signal to Noise Ratio (SNR), broadband signals excite several frequencies simultaneously. A single acquisition allows computing the $\alpha_{mat}(f)$ curve from the theoretical transmitted and received spectra. Additionally, a pseudo-continuous attenuation curve is obtained instead of a discretization of $\alpha_{mat}(f)$.

$$S_{rx}(f) = |X(f)|^2 \tag{3.3.7}$$

$$X(f) = \int_{t_0}^{t_1} x(t)e^{-i2\pi f t} dt \tag{3.3.8}$$

The global attenuation associated to the measurement equipment (transducers, amplifier, wires, acquisition module, ...), $\alpha_{equip}(f)$, is independent of the tested material and is constant over the test. The calibration process of the system was assessed with the same configuration but without the specimen under study, being the transducers surface facing each other. For further details about the calibration process see [14](Section 2.3).

Different layouts can be used to make an ultrasonic inspection. In this study, a through-transmission setup was selected, since it offers good penetration and good accuracy for estimating the velocity and attenuation [20, 21]. Figure 3.3.4 shows the ultrasonic setup for this experiment. The transducers (transmitter and receiver) used were the K05SC from General Electric. Both are broadband transducers with a bandwidth centred at 0.5 MHz. The transmitter transducer was excited directly by a programmable signal generator (Handyscope HS3) and the reception transducer was connected to a 40 dB preamplifier (Panametrics 5600B).

The received and amplified ultrasonic signal was captured by a digital oscilloscope (Handyscope HS3) with a sampling frequency of 50 MHz. Both oscilloscope and signal generator are the same device in the real experiment. Finally, a laptop was used to control the signal generator and to acquire and store the digitized signals. The ultrasonic transducers were placed facing the longitudinal axis of the prismatic specimen, and they were fixed by a clamp. Pure vaseline at the transducer–specimen interfaces was used as an impedance coupling medium.

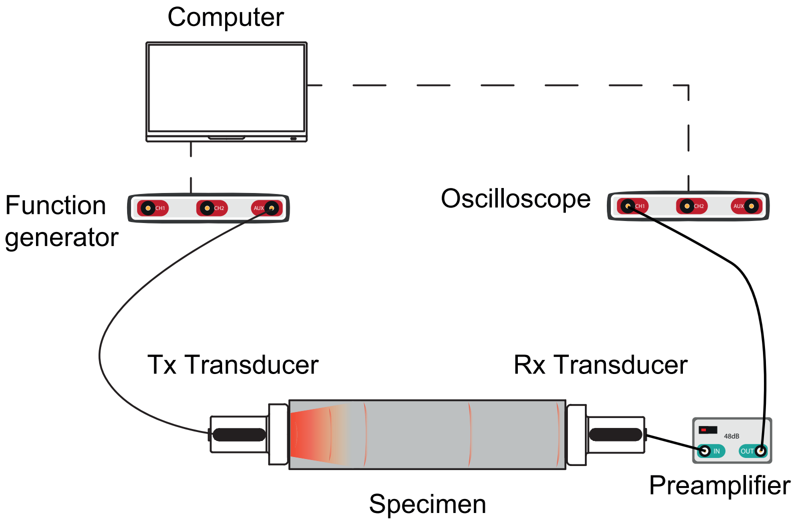

Figure 3.3.4: Ultrasonic layout.

3.3.3 Results

3.3.3.1 Microstructural tests

Thermogravimetry

In thermogravimetry analysis, the decomposition of different hydration products of Portland cement paste can be observed. In Figure 3.3.5, the derivative of mass loss curve shows the typical decomposition peaks of this kind of material for all analyzed temperatures.

At 90 °C a premature decomposition of de C-S-H can be noticed respect to 40 °C series. At 150 °C, C-S-H and ettringite peaks partially disappeared. At 250 °C and 400 °C no important changes happen in terms of thermal decomposition. At 525 °C a displacement and decrement of the Portlandite peak occurs.

Table 3.3.1 shows the percentages of mass loss (relatives to the anhydrous mass) of the total water, portlandite and hydrates for all tested temperatures. As the temperature increases, the total mass loss decreases due to the previous thermal treatment. Water associated to portlandite remains constant or slightly increased due to the free portlandite generated from the S-C-H and A-C-H decomposition for temperatures under 400 °C. However, water loss associated to portlandite experiments huge decrease when 525 °C is reached due to its partial decomposition. The percentage of H_2O loss respect to the water content for sam-

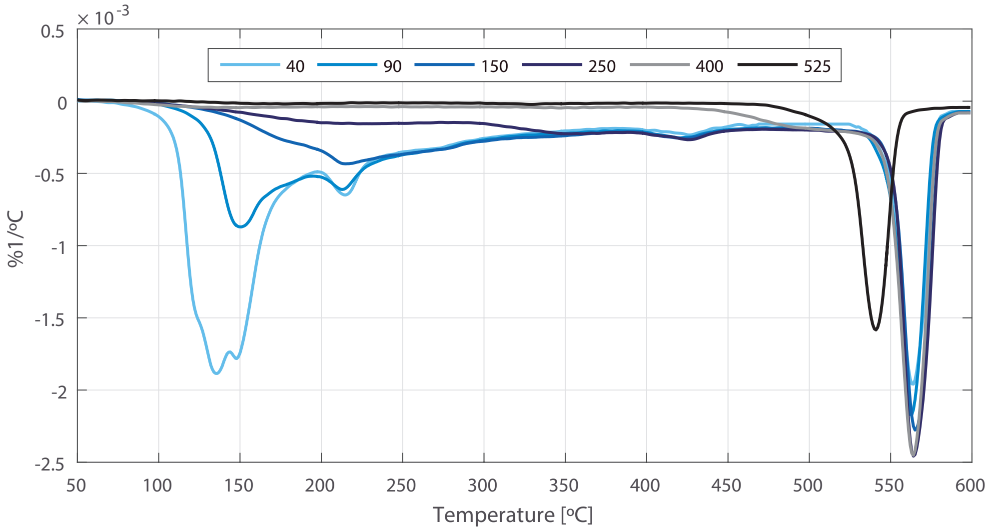

Figure 3.3.5: DTG curves for all analysed temperatures [°C].

ple treated at 40 °C showed a continuous increase, reaching to 81.07 % for 525 °C treatment.

Table 3.3.1: TG results based on anhydrous mass.

Temperature [°C]	Combined water [%]	H_2O from $Ca(OH)_2$ [%]	Portlandite [%]	H_2O lost [%]*
40	30.01	4.76	19.56	0.00
90	22.22	4.68	19.24	21.23
150	17.97	4.75	19.54	34.01
250	14.32	5.05	20.77	45.71
400	8.81	6.10	25.10	64.90
525	4.57	3.66	15.05	81.07

* Respect to 40 °C sample

Scanning Electron Microscopy

Microscopy images were acquired with the aim of analize differences between pristine and damaged samples in a micro and nanoscopic scale. To see differences in the Portland cement matrix, pastes with 0.5 water to cement ratio were prepared and cured 90 days before exposing them to 40 and 525 °C. Figures 3.3.6a, 3.3.6b and 3.3.6c show pristine paste samples under SEM. In Figure 3.3.6a, amorphous particles of C-S-H and A-C-H can be observed. This type of hydration products are the most common components in the Portland cement matrices. Ettringite needles and Portlandite formation can be distinguish in Figures 3.3.6b and 3.3.6c surrounded by C-S-H and A-C-H respectively. At the same magnifications, Figures 3.3.6d, 3.3.6e and 3.3.6f show paste specimens exposed to 525 °C. In this series, mainly C-S-H and A-C-H products can be observed. Ettringite and Portlandite, easily detectable in 40 °C samples, completely disappeared as shown in the thermogravimetic analysis. Apparently, the morphology of the attacked C-S-H and A-C-H products can not be distinguished from the pristine ones at a naked eye in SEM.

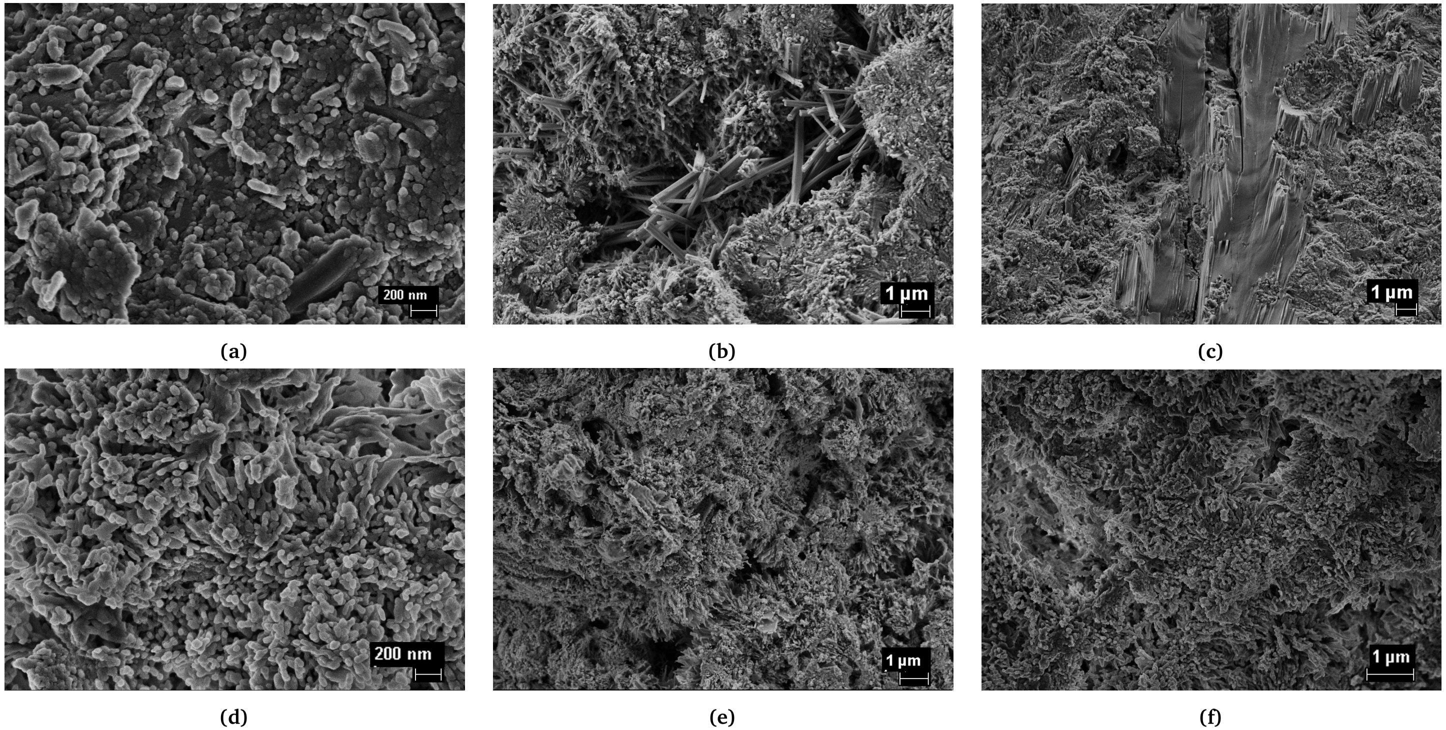

(a) (b) (c)

(d) (e) (f)

Figure 3.3.6: FESEM micrographs of Portland cement pastes. Figures 3.3.6a, 3.3.6b and 3.3.6c treated at 40 °C. Figures 3.3.6d,3.3.6e and3.3.6f treated at 525 °C.

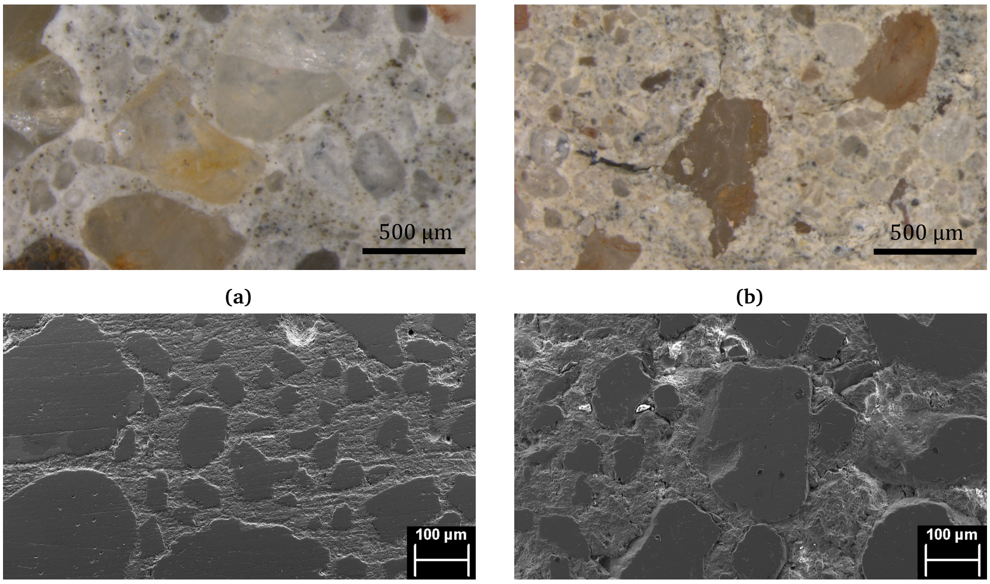

(a) **(b)**

(c) **(d)**

Figure 3.3.7: Microscopy images of polished mortar sections. Figure 3.3.7a image of a pristine sample of mortar under optic microscope. Figure 3.3.7b image of a thermal damaged (525 °C) sample of mortar under optic microscope. Figure 3.3.7c image of a pristine sample of mortar under SEM. Figure 3.3.7d image of a thermal damaged (525 °C) sample of mortar SEM .

Figures 3.3.6a-3.3.6c and 3.3.6d-3.3.6f shows 40 and 525 °C polished sections of paste specimens respectively. In Figure 3.3.7a (40 °C) it can be observed a highly cohesive material with strong matrix perfectly embracing the aggregates inside observed in optic microscope. On the contrary, Figure 3.3.7b (525 °C) shows remarkable fractures in the matrix in a radial direction surrounding the aggregates. Besides, the disconnection between cement paste an the aggregate becomes noticeable to the naked eye. Same behaviour can be noticed from Figures 3.3.7c and 3.3.7d where the same specimens where analysed in the nanoscale under SEM.

3.3.3.2 Physical and mechanical tests on mortar

In order to distinguish the different mechanisms of degradation in the thermal damage on cementitious materials, different kind of physical tests were performed. Three additional specimens per analyzed temperature were manufactured due to the destructive nature of the compression and flexural strength tests. Figure 3.3.8a shows the mass loss due to the debonded water in hydration products of Portland cement. As can be observed, the mass of specimens decrease in a non-linear trend as the temperature increases. Nonetheless, mechanical performance of the elements increases during this heat treatment as shows Figures 3.3.8b and 3.3.8c until 150° C .

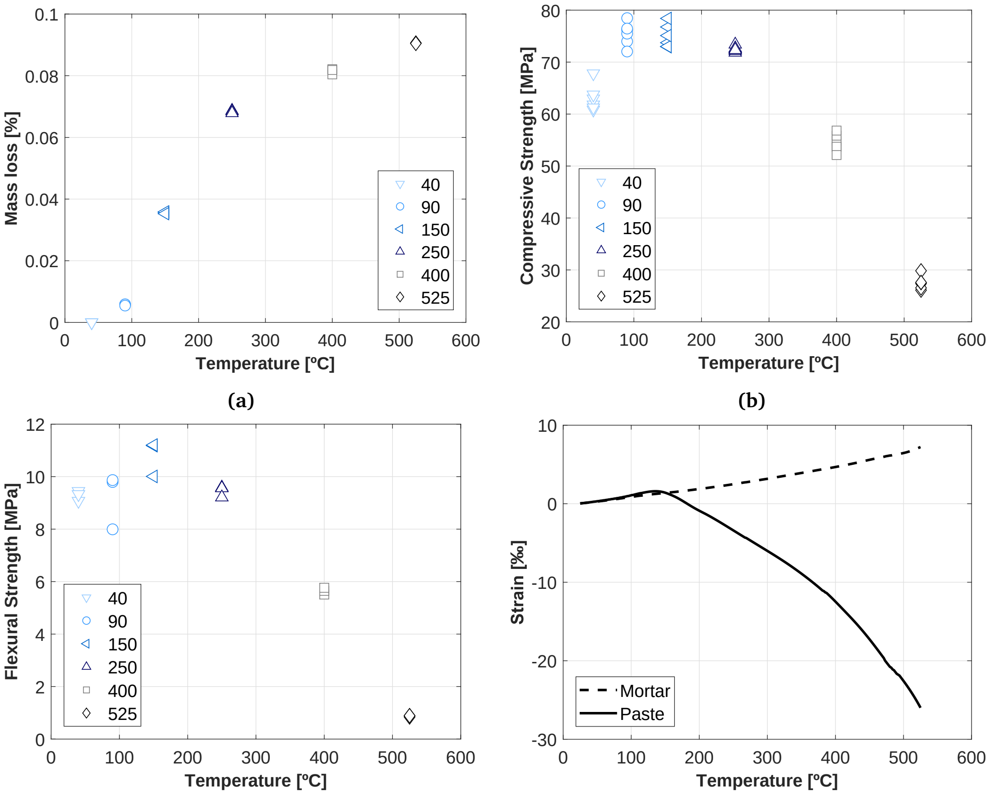

(a)

(b)

(c)

(d)

Figure 3.3.8: Physiscal and mechanical tests performed to the material for all monitored temperatures. Figure 3.3.8a Mass loss. Figure 3.3.8b Compressive strenght. Figure 3.3.8c Flexural strenght. Figure 3.3.8d Dilatometry.

This slight improvement (or conservation) in the strength could be attributed to an increase in curing speed of the element, directly enhancing its mechanical properties. After 150 °C, mechanical strength starts a decay process during the rest of the experiment. To understand the degradation process, Figure 3.3.8d should be analyzed in detail. In this figure, relative longitudinal elongation (strain) was plotted for paste and mortar samples. These specimens were made with the same dosage presented in the previous section. In the first instance, in 20 °C to 150 °C paste and aggregate expands at the same rate, being paste and mortar series quasi-coincident. After this temperature, a bifurcation between mortar and paste occurs due to a trend change until 350 °C. Beyond 350 °C the negative slope of deformation increases while mortar continues expand linearly. This test reveals the incompatibility of thermal deformations between the paste and aggregate, leaving clear evidences about the damage produced by the increment of the temperature, being this a complex mechanism that not only involves the destruction of hydrated products of the cement paste but also the difference in thermal strain of the raw materials that are part of the mortar sample.

3.3.3.3 Non-destructive techniques measurements

Non-linear spectroscopy

Non-linear Impact Resonance Acoustic Spectroscopy (NIRAS) technique can extract non-linear elastic and hysteresis information of mesoscopic materials like mortar or concrete.

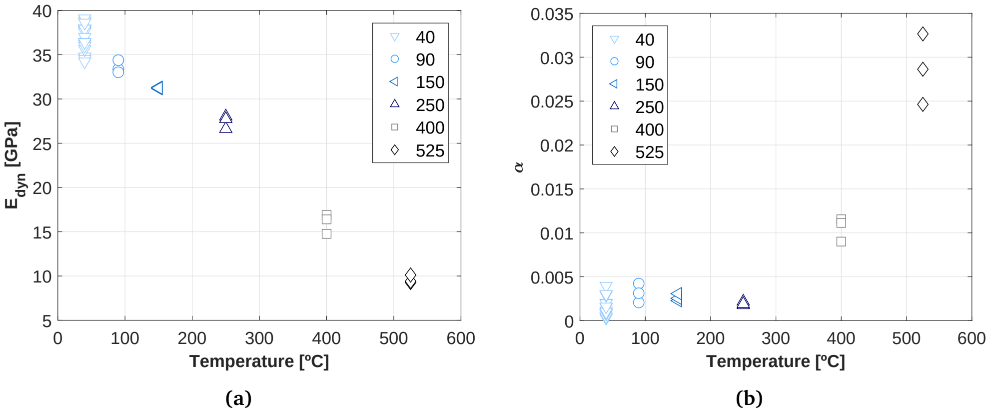

Figure 3.3.9: Vibrational test performed to the material for all monitored temperatures. Figure 3.3.9a Dynamic modulus. Figure 3.3.9b Non-linear parameter.

Figure 3.3.9a represents elastic modulus extracted linear frequency (f_0) from NIRAS test. The plot clearly defines a linear decay of the stiffness on mortar elements due mass loss directly related to debonding water of the hydrated portland cement matrix. Non-linear parameter reveals important information about the internal state of the material. As can be observed, α values remains constant before 250 °C; after this temperature, α values increases to higher values during the experiment. As observed in previously section, in Figure 3.3.8d, the huge differences between the deformation of the aggregate and the paste, force the aggregate to separate from the paste. Such phenomena increases the non-linearity and hysteresis of the system, rising the hertzian contact effect and mesoscopic discontinuities. This process is the only one provoking a real decay in global performance of the material since the mass loss is only affecting to its softening. NIRAS test takes advantage of linear and non-linear analysis of materials allowing to describe complex damage processes, when in the same system different mechanisms of degradation take place at the same time.

Ultrasonics

Ultrasonic tests reveal information about the changes in a mechanical wave travelling through a material unlike vibration tests, where the material resonates in its principal modes after an excitation. Pulse velocity and material attenuation are complementary parameters extracted from the ultrasonic signal, and from they, it can be registered different kind of information from the material. Pulse velocity is more related to the stiffness of the material, being proportional to the dynamic modulus. However, attenuation is more related to the dispersive elements inside the material like aggregates, voids and micro cracks.

Figure 3.3.10a shows the changes in ultrasonic pulse velocity for all specimens. As can be observed, non-linear negative trend can be revealed as the temperature rises. This behavior matches with the trend of E_{dyn} extracted from NIRAS test since velocity is squared in dynamic modulus equation when is extracted from P-wave and S-wave velocity [6]. As commented in vibration tests, the stiffness on mortar elements decays due mass loss directly related to debonding water of the hydrated portland cement matrix. In Figure 3.3.10b, attenuation versus frequency curves are plotted for different temperatures.

Since frequency is proportional to wavelength, the increment of frequency in ultrasonic inspections implies being more sensitive to small defects and discontinuities. That means the attenuation mechanism (absorption and reflection, mainly) reveals the global status of the material, being an interesting phenomena to analyze pores, cracks and defects. As can be observed, 40, 90 and 150 °C presents almost the same attenuation values for all frequency range. From 250 °C to 400 °C, a huge change in attenuation values from 600 to 900 kHz appears, predicting the paste-aggregate separation forced by the incompatibility of deformation between them. 525 °C series exhibited a high attenuation behaviour for all frequency range,

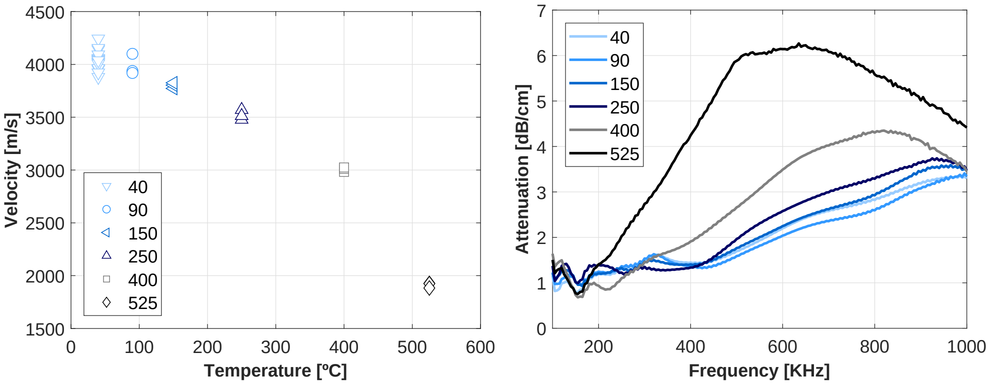

(a) (b)

Figure 3.3.10: Ultrasonic test performed to the material for all monitored temperatures. Figure 3.3.10a Ultrasonic pulse velocity. Figure 3.3.10b Material energy wave attenuation.

rising to higher values with a noticeable slope since 100 kHz provoked by the softening of the portland cement matrix, induced micro cracking and the degradation of interfacial transition zone between the paste and the aggregate.

3.3.4 Conclusions

Thermal attack in concrete is a complex mechanism of damage in Portland cement composites. Temperature do not only affect to the cement matrix, but also to incompatibility of deformation between aggregate and paste. In this study a complete analysis of this kind of damage is addressed, not only with traditional methods but also trying to capture the intricate system with non-destructive tests and also analyse and correlate this data with physical and microstructural tests for different temperatures between 40 °C and 525 °C.

Microstructural analysis (Thermogravimetry and Scanning Electron Microscopy) showed the principal changes of the Portland cement hydrated products for the different analysed temperatures. Compressive and flexural strength results remained constant or even increases at low temperatures (up to 250 °C) meanwhile the mass loss increases. Dilatometry results revealed important information about deformation incompatibilities between the paste and the aggregate. These results have been correlated with non-destructive tests: non-linear impact resonance acoustic spectroscopy and ultrasonic measurements. The dynamic modulus and ultrasonic pulse velocity have closely predicted the linear stiffness decay of the specimens. However, non-linear parameter exhibited different trend from stiffness-related parameters, keeping constant until 250 °C and performing a huge change for 400 and 525 °C. Ultrasonic attenuation computed with a broadband ultrasonic signal (chirp) unveiled true information in one single signal about scattering components inside the material, being sensitive to interfacial transition zone between aggregate and paste in a large range of frequencies. The correlation between microstructural, mechanical and non-destructive techniques were carry out successfully, being non-linear vibration and ultrasonic attenuation a non-conventional parameters that gave crucial of information about a complex damage process like thermal attack in a highly heterogeneous materials (Portland cement composites).

Acknowledgements

This work has been supported by the Spanish Administration under grants, BES2015-071469, under the test coordinated project, BIA2014-55311-C2-1-P and BIA2014-55311-C2-2-P. Thanks are given to FEDER funds for co-funding.

References

[1] P. C. Aïtcin, *Binders for durable and sustainable concrete*. CRC Press, 2014.

[2] U. Schneider, “Concrete at high temperatures - A general review,” *Fire Safety Journal*, vol. 13, no. 1, pp. 55–68, 1988.

[3] Q. Ma, R. Guo, Z. Zhao, Z. Lin, and K. He, “Mechanical properties of concrete at high temperature-A review,” *Construction and Building Materials*, vol. 93, pp. 371–383, 2015.

[4] C. R. Cruz and M. Gilien, “Thermal Expansion of Portland Cement Paste, Mortar and Concrete at High Temperatures,” *Fire and Materials*, vol. 4, no. 2, pp. 66–70, 1980.

[5] A. H. Jay, “The thermal expansion of quartz by X-ray measurements,” *Proceedings of the Royal Society of London. Series A, Containing Papers of a Mathematical and Physical Character*, vol. 142, no. 846, pp. 237–247, 1933.

[6] V. M. Maholtra and N. J. Carino, Eds., *Handbook on Non destructive Testing on Concrete*. CRC Press, 2004, vol. 1.

[7] K. Van Den Abeele, P. A. Johnson, and A. Sutin, “Nonlinear Elastic Wave Spectroscopy (NEWS) Techniques to Discern Material Damage, Part II: Single-Mode Nonlinear Resonance Acoustic Spectroscopy,” *Research in Nondestructive Evaluation*, vol. 12, no. 1, pp. 17–30, 2000.

[8] K. Van Den Abeele, J. Carmeliet, J. A. Ten Cate, and P. Johnson, “Nonlinear ElasticWave Spectroscopy (NEWS) Techniques to Discern Material Damage, Part I: Nonlinear Wave Modula- tion Spectroscopy (NWMS),” *Research in Nondestructive Evaluation*, vol. 12, no. 1, pp. 17–30, 2000.

[9] P. A. Johnson and A. Sutin, “Nonlinear elastic wave NDE I. Nonlinear resonant ultrasound spectroscopy and slow dynamics diagnostics,” in *AIP Conference Proceedings*, 2005, ISBN: 0735402450.

[10] K. J. Leśnicki, J. Y. Kim, K. E. Kurtis, and L. J. Jacobs, “Characterization of ASR damage in concrete using Nonlinear Impact Resonance Scoustic Spectroscopy technique,” *NDT & E International*, vol. 44, no. 8, pp. 721–727, 2011.

[11] S. J. Park, H. J. Yim, and H. G. Kwak, “Nonlinear resonance vibration method to estimate the damage level on heat-exposed concrete,” *Fire Safety Journal*, vol. 69, pp. 36–42, 2014.

[12] U. Dahlen, N. Ryden, and A. Jakobsson, “Damage identification in concrete using impact non-linear reverberation spectroscopy,” *NDT & E International*, vol. 75, pp. 15–25, 2015.

[13] V. Genovés, A. Carrión, J. Gosálbez, I. Bosch, M. V. Borrachero, and J. Payá, “Optimized ultrasonic attenuation measures for internal sulphate attack monitoring in portland cement mortars,” in *Ultrasonics Symposium (IUS), 2017 IEEE International*, IEEE, 2017, pp. 1–4.

[14] V. Genovés, J. Gosálbez, A. Carrión, R. Miralles, and J. Payá, “Optimized ultrasonic attenuation measures for non-homogeneous materials,” *Ultrasonics*, vol. 65, pp. 345–352, 2016.

[15] T. P. Philippidis and D. G. Aggelis, “Experimental study of wave dispersion and attenuation in concrete,” *Ultrasonics*, vol. 43, no. 7, pp. 584–595, 2005.

[16] M. Molero, I. Segura, S. Aparicio, M. G. Hernández, and M. A. G. Izquierdo, “On the measurement of frequency-dependent ultrasonic attenuation in strongly heterogeneous materials,” *Ultrasonics*, vol. 50, no. 8, pp. 824–828, 2010.

[17] V. Genovés, F. Vargas, J. Gosálbez, A. Carrión, M. Borrachero, and J. Payá, “Ultrasonic and impact spectroscopy monitoring on internal sulphate attack of cement-based materials,” *Materials & Design*, vol. 125, pp. 46–54, 2017.

[18] M. V. Borrachero, J. Payá, M. Bonilla, and J. Monzó, “The use of thermogravimetric analysis technique for the characterization of construction materials,” *Journal of Thermal Analysis and Calorimetry*, pp. 503–509, 2008.

[19] V. Genovés, L. Soriano, M. Borrachero, J. Eiras, and J. Payá, “Preliminary study on short-term sulphate attack evaluation by non-linear impact resonance acoustic spectroscopy technique,” *Construction and Building Materials*, vol. 78, pp. 295–302, 2015.

[20] J. Krautkrämer and H. Krautkrämer, *Ultrasonic testing of materials*. Springer-Verlag, 1983.

[21] P. A. Gaydecki and F. M. Burdekin, “The propagation and attenuation of medium-frequency ultrasonic waves in concrete: a signal analytical approach,” *Measurement Science and Technology*, vol. 3, p. 126, 1992.

3.4 Effects of slow dynamics and conditioning on non-linear hysteretic material evaluation[8]

[8] A. Carrión, V. Genovés, G. Pérez, J. Bittner, J. Popovics, J. Payá, and J. Gosálbez. "Effects of slow dynamics and conditioning on non-linear hysteretic materials evaluation: NIRAS and FANSIRAS,". Journal of American Society of Acoustics (Submitted).

Abstract

The microstructural features of heterogeneous and porous materials causes unique non-linear dynamic behavior in such materials. The purpose of this work is to investigate the dynamic response of thermally damaged concrete specimens measured by two different methods: Non-linear Impact Resonance Acoustic Spectroscopy (NIRAS) and new Flipped Accumulative Non-linear Single Impact Acoustic Spectroscopy (FANSIRAS). The specimens have been characterized in two different dynamic condition states of the material: relaxed and conditioned. The relaxed state of the specimen indicates that there is no previous dynamic excitation event while the conditioned state indicates the specimen has been dynamically tested before. NIRAS results show that the non-linear parameter related to the resonance frequency shift, α_f, varies its trend depending on its previous dynamic history. However, the non-linear parameter related to the damping properties, α_Q, shows more stable values since is not affected by the dynamic background of the material. The recently proposed algorithm, FANSIRAS, extracts from a single resonant signal equivalent results to NIRAS when the specimen is conditioned. In this situation, both parameters α_f and α_Q have been shown to be equivalent.

3.4.1 Introduction

Geomaterials, such as rocks, sand, soil or their aggregates, such as concrete, belong to a newly defined class of so-called as Non-linear Mesoscopic Elastic (NME) materials [1]. These materials are characterized by a heterogeneous internal structure, whose non-linear response appears related to its large variety of microstructural features (i.e. micro-cracks, grain contacts, interstices, etc.) and becomes orders of magnitude larger than that shown by the classical atomic elastic materials. The non-linear elastic behavior of NME materials cannot be described by Landau's [2] classical non-linear theory. Its singularity is reflected in the manifestation of a hysteretic behavior and evidence of discrete memory effects in the relaxation processes, which are denominated in the literature Anomalous Non-linear Fast Dynamics (FD) and Slow Dynamics (SD), respectively [3], for both the quasi-static behavior (stress-strain experiments) and for the dynamic (resonant-wave experiments).

The most widely employed Non-Destructive Testing (NDT) methods for monitoring damage processes in concrete and other cement-based materials have focused on the study of the material's non-linear dynamic anomalies due to its greater sensitivity in comparison with linear dynamic anomalies when early detecting global defects [4]. Ostrovsky and Johnson [5] listed a thorough variety of non-linear response manifestations in quasi-static and, especially, in dynamic laboratory experiments. Some of these are the non-linearity and the hysteretic and discrete memory phenomena, both in stress-strain experiments: the appearance of new harmonic frequency components, wave cross-modulation amplitudes, resonance frequency shifts, amplitude-dependent losses and slow dynamics in non-destructive procedures [4, 6]. These NDT, which draw on the non-linear dynamic behavior, are considered as Non-linear Elastic Wave Spectroscopy (NEWS) methods.

Regardless of the source used to excite the specimens under study, all of the NEWS methods share the same baseline concepts for extracting the characteristic non-linear parameters of mesoscopic materials. Due to its easy excitation procedure and remarkable sensitivity when measuring the non-linear behavior, a prominent line of research is focused on impact spectroscopy. In contrast to the multiple increasing impact driving amplitudes needed in the Non-linear Impact Resonance Acoustic Spectroscopy (NIRAS) methodology [7–9] to quantify the non-linear response, recent advances have focused on single impact approaches based on a optimal signal processing procedure [10, 11]. Accordingly, the authors introduced a novel single impact technique, FANSIRAS, with the aim of characterizing the underlying non-linear physical phenomenon within a signal processing perspective [12]. In the present study, the comparison between both techniques, NIRAS and FANSIRAS, is taken a step further. Both approaches are applied on two different motion process moments of the specimens, resting (a rested specimen is excited by impacts whose level consecutively increases) and conditioned (a rested specimen is excited by impacts whose level consecutively decreases) to evaluate the effects of slow dynamics and conditioning over the impact resonance spectroscopy techniques. The joint analysis of both configurations (upward and downward impacts) may describe the hysteretic behavior of non-linear mesoscopic materials, such as concrete.

Damage in concrete has been widely investigated throughout the years from many different points of view. Different degradation mechanisms cause distinct modifications to the material's dynamic response, which implies that a detailed analysis of all physical mechanisms is required to fully understand degradation processes [13–15]. In particular, thermal attack in concrete depends on many variables, the most important of which is the dosage of the composite (aggregate type and proportion, water/cement ratio, cement type...) and the exposed temperature. Due to the complexity of this damage (stiffness matrix loss, incompatibility of deformation between aggregate and paste, expansive products...), several studies have been carried out to distinguish and quantify the damage and physical behavior of the material [16, 17]. NDT evaluation through ultrasonic inspection and vibrational analysis are the most used and developed techniques to assess this degradation process due to their simple implementation and non-invasive nature [9, 18–22]. In this study, the authors continue vibrational analysis with the inclusion of the non-equilibrium dynamics of mortar elements under stepped thermal damage. This analysis permits us to, simultaneously, draw on all the potential of the NEWS techniques and evaluate the robustness of the non-linear parameters extracted with NIRAS and FANSIRAS against the effects of slow dynamics and conditioning at different levels of damage. The overall motivation is to understand the notable dispersion between results of different NEWS experiment layouts in different research groups involved in non-linear dynamics projects.

3.4.2 Mathematical background

3.4.2.1 NIRAS

The NIRAS technique relies on an impulse excitation of the specimen repeated with different impact strengths. The different reverberation signals are denoted by $y_i(n)$, being i the impact number (in this study, $i \in [1, 10]$). The non-linear parameter related to the resonance frequency shift α_f^{NIR} is obtained from a linear regression fit

$$\frac{\tilde{f}_0 - \tilde{f}_i}{\tilde{f}_0} = \alpha_f^{NIR} \cdot A_i \tag{3.4.1}$$

where A_i is the obtained peak amplitude spectrum

$$A_i = max\{|Y_i[f]|\} \tag{3.4.2}$$

and $\tilde{f}_i$ is the peak normalized frequency of one mode

$$\tilde{f}_i = max_f\{|Y_i[f]|\} \tag{3.4.3}$$

from the multiple impacts at different strengths i. Here, $\tilde{f}_0$ denotes the resonance frequency obtained in the linear strain regime. For low excitation amplitudes [23], the frequency shift $(\tilde{f}_0 - \tilde{f}_i)$ is non-existent and the peak frequency is considered to be obtained in the linear strain regime. In this study, $\tilde{f}_0$ is determined as the intersection with the y-axis of the linear relation between the peak amplitudes A_i (x-axis) and the peak frequencies $\tilde{f}_i$ (y-axis). The non-linear parameter related to the shift of the damping properties, α_Q^{NIR}, is assumed to exhibit a linear relationship (Eq. 3.4.4):

$$\frac{1}{Q_i} - \frac{1}{Q_0} = \alpha_Q^{NIR} \cdot A_i \tag{3.4.4}$$

where A_i is the peak amplitude (Eq. 3.4.2), Q_i is the damping factor obtained for each impact i (Eq. 3.4.5)

$$Q_i = \frac{\tilde{f}_i}{\tilde{f}_{i,2} - \tilde{f}_{i,1}} \tag{3.4.5}$$

where $\tilde{f}_{i,2} - \tilde{f}_{i,1}$ is the half-power bandwidth resonance, and Q_0 is the linear regime damping factor determined as the intersection with the y-axis of the linear relationships between the peak amplitudes A_i (x-axis) and the measured damping factors Q_i (y-axis) [19]. One expects to find an increase in both parameters proportional to the hysteresis, α_f^{NIR} and α_Q^{NIR}, when increasing the thermal damage of the specimen.

3.4.2.2 FANSIRAS

The Flipped Accumulative Non-Linear Single Impact Resonance Acoustic Spectroscopy (FANSIRAS) technique only requires a single reverberation signal $y_I(n)$ plus a suitable optimal signal processing to obtain a reliable estimate of the non-linearity. The acronym of the technique corresponds to the underlying signal processing algorithm based on the reconstruction of the signals of the NIRAS technique from a single signal: flipping the signal and windowing cumulatively. To ease the mathematical nomenclature, the method is described as a window of initial length equal to that of the acquired signals, N, which progressively decreases its length to the lower bound, and transforms the time segment of the impact signal within the p-th window, $y_{I,w_p^{L_p}}(n)$, to the frequency domain at each window position:

$$\begin{aligned} & y_{I,w_p^{L_p}}(n) = y_I(n) \cdot w^{L_p}(n - p \cdot M), \\ & n \in \{0, \ldots, N-1\}, p \in \left\{0, \ldots, \left\lfloor \frac{N}{M} \right\rfloor - 1 \right\}. \end{aligned} \tag{3.4.6}$$

Here, $w_p^{L_p}(n)$ represents a rectangular window, which shortens at each step of the algorithm

$$w_p^{L_p}(n) = \begin{cases} 1, & 0 \le n \le L_p - 1 \\ 0, & otherwise \end{cases} \tag{3.4.7}$$

The length of the window varies at each position p, $L_p = N - p \cdot M$, where M represents the number of samples by which the window decreases at each step of the algorithm. The number of points used in the later regression is related to the value of M but it does not significantly affect the estimation of the non-linear parameters. In this work, M equals the number of samples in 2 periods of the signal ($M = 2f_s/\tilde{f}_0$, where f_s is the sampling frequency).

The non-linear parameters $\alpha_{f,I}^{FAN}$ and $\alpha_{Q,I}^{FAN}$ are both estimated according to the linear fits seen for NIRAS technique but using the current variables obtained from a single reverberation signal corresponding to the strongest impact level I. Each time segment of the reverberation signal within the $p-th$ window, $y_{I,w_p^{L_p}}(n)$, is studied in the frequency domain by applying the discrete-time, discrete-frequency Fourier Transform (DFT) resulting in $Y_{I,w_p^{L_p}}[f]$:

$$Y_{I,w_p^{L_p}}[f] = DFT\{y_{I,w_p^{L_p}}(n)\} \tag{3.4.8}$$

For each position p, the peak amplitude spectrum $A_{I,p}$ is computed (Eq. 3.4.9)

$$A_{I,p} = max\{|Y_{I,w_p^{L_p}}[f]|\} \tag{3.4.9}$$

and the peak frequency $\tilde{f}_{I,p}$ is computed (Eq. 3.4.10)

$$\tilde{f}_{I,p} = max_f\{|Y_{I,w_p^{L_p}}[f]|\} \tag{3.4.10}$$

where the function $max_f\{\cdot\}$ defines the peak amplitude spectrum projected over the frequency vector. The non-linear parameter related to the resonance frequency shift $\alpha_{f,I}^{FAN}$ is obtained from the linear fit of the $A_{I,p}$ and $\tilde{f}_{I,p}$ (Eq. 3.4.11)

$$\frac{\tilde{f}_{I,0} - \tilde{f}_{I,p}}{\tilde{f}_{I,0}} = \alpha_{f,I}^{FAN} \cdot A_{I,p} \tag{3.4.11}$$

where $\tilde{f}_{I,0}$ is the resonance frequency obtained in the linear strain regime. $\tilde{f}_{I,0}$ is determined as the intersection with the y-axis of the linear relation between the peak amplitudes $A_{I,p}$ (x-axis) and the peak frequencies $\tilde{f}_{I,p}$ (y-axis).

Analogously, the damping factor $Q_{I,p}$ is also computed for each $p-th$ window position (Eq. 3.4.12):

$$Q_{I,p} = \frac{\tilde{f}_{I,p}}{\tilde{f}_{I,p,2} - \tilde{f}_{I,p,1}} \tag{3.4.12}$$

and the non-linear parameter proportional to the damping properties $\alpha^{FAN}_{I,Q}$ is obtained as the slope of the linear relation between the peak amplitudes, $A_{I,p}$, and the damping factor, $Q_{I,p}$:

$$\frac{1}{Q_{I,p}} - \frac{1}{Q_{I,0}} = \alpha^{FAN}_{I,Q} \cdot A_{I,p} \tag{3.4.13}$$

where $Q_{I,0}$ is the approximation for the linear regime damping factor related to the reverberation signal $y_I(n)$. When working with real signals (N samples acquired with a sampling frequency f_s), window shortening must stop before losing signal information (i.e. too small window). The window in FANSIRAS algorithm is decreased until the value of Q is lower than that obtained in the previous window. See [12] for further technical aspects of the algorithm.

Figure 3.4.1 shows a schematic representation of the two algorithms both in the time and frequency domains. It summarizes the differences between the procedures mainly distinguished by the number of input signals (number of blows) and the signal processing. NIRAS uses 10 measurements with varying impact force amplitude while FANSIRAS requires just one measurement at high impact force amplitude. FANSIRAS signal processing algorithm tries to reconstruct the signals of the NIRAS technique with the aim of extracting equivalent non-linear parameters from a single measurement.

3.4.3 Experimental

3.4.3.1 Materials and specimens

Six mixes of standardized Portland cement concrete (water/cement = 0.5) made of 450 g of Spanish cement CEM I-52.5-R, 1350 g of 0/2 mm crushed quartz sand and 225 g of water were carried out to obtain 18 40 × 30 × 160 mm^3 specimens. After the mixing process, iron moulds were stored in a wet chamber (20 °C and 100 % H.R.) for 24 hours. Then, the 18 mortar pieces were released and stored in the wet chamber again for 60 days in order to reach elastic properties stabilization stage. Afterwards, the specimens were dried until a constant mass at 40 °C for 7 days and wrapped with plastic film until reached room temperature again in order to characterize them in what we define to be the pristine state. Two levels of thermal damage treatment were performed according to the chemical

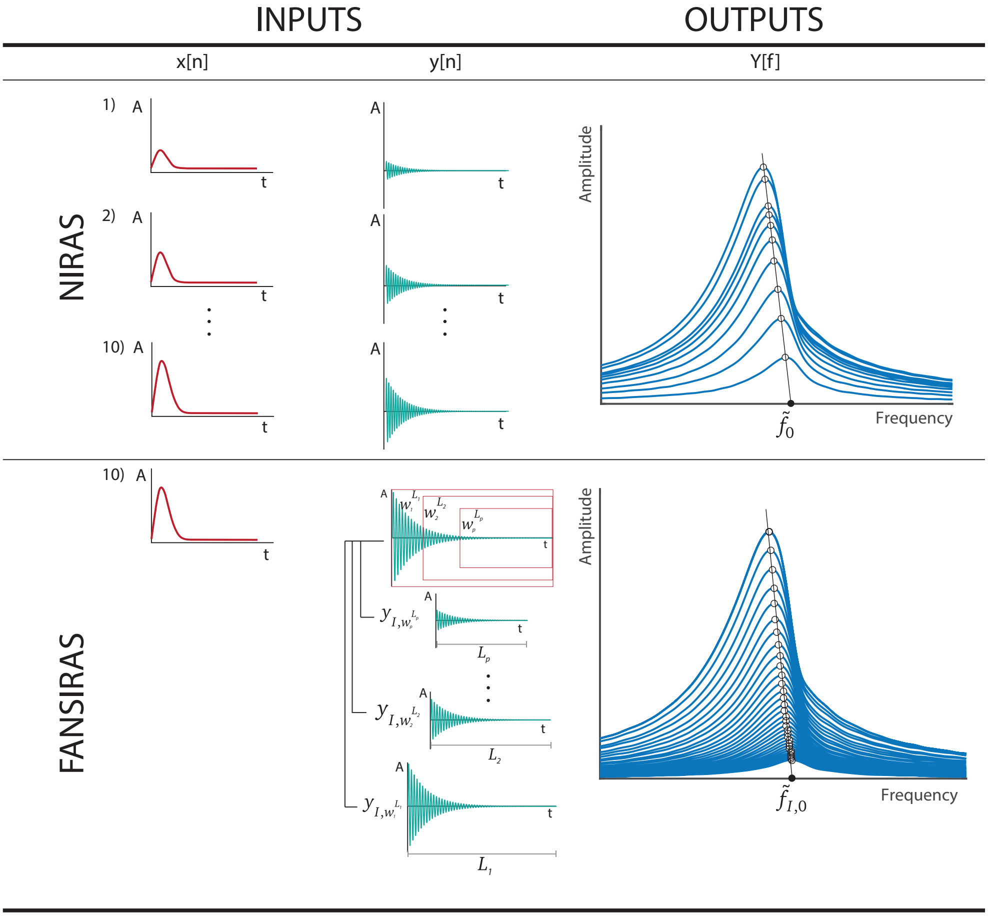

Figure 3.4.1: Schematic comparison between NIRAS and FANSIRAS techniques. NIRAS algorithm (top) is represented by 10 impact signals with varying input force amplitude $x_i[n], i \in [1,10]$, and its corresponding output reverberation signals, $y_i[n], i \in [1,10]$, and their corresponding the Fourier Transform spectra, $Y_i[f]$. The FANSIRAS algorithm (bottom) reconstructs the equivalent NIRAS signals from a single output reverberation signal, $y_I[n]$, by means of signal processing.

decomposition of Portland cement hydrates. The first level contained six specimens were thermally damaged at 400 °C (C-S-H and C-A-H decomposition took place), reaching this temperature in 2 hours, keeping it during 3 hours and slowly cooled for 12 hours inside the oven. The second level contained six specimens were thermally damaged at 525 °C ($Ca(OH)_2$ decomposition took place) following the same procedure as commented for 400 °C damaging test. Consequently, six different specimens per condition (40, 400 and 525 °C) were created to carry out the non-linear acoustic analysis. Three additional specimens per series were manufactured to carry out traditional destructive tests. In the first instance, concrete blocks were tested in three-point bending test configuration to obtain the flexural strength of the material exposed at 40, 400 and 525 °C. The remaining six semi-prisms were used to obtain compressive strength.

3.4.3.2 Test Layout

Acoustic resonance tests were carried out for the 18 specimens at the three thermal treatments. The experimental layout is composed of an impact hammer (Brüel & Kjær 8206-003) attached to an iron axle located in a metallic structure. This metallic axle is supported on two ball bearings yielding a free rotational motion in one plane with minimal friction. The specimen was located in a metallic supports, slightly sloping, allowing a centred and perpendicular impact to the specimen face. In the opposite face to the impact, in the top-left corner, a piezoelectric accelerometer sensor (PCB 352A21) was attached in order to obtain the vibrational motion of the test probe. The electric signal of the instrumented hammer and the accelerometer go through a signal conditioner (PCB 482A18) polarizing it and transmitting it to the oscilloscope (Tektronix MDO3014). The oscilloscope was configured with f_s equals to 250 kHz, N equals 10000 samples, trigger voltage equals to 120 mV and pretrigger time equals to 4 ms. Finally, the information was transmitted via USB to a computer with a control software developed by the authors based on the Instrument Control Toolbox of MATLAB.

3.4.4 Results and discussion

3.4.4.1 Mechanical and physical properties of concrete

The compressive strength results are shown in Figure 3.4.2a. Compressive strength at 40 °C, 62.5 ± 4 MPa, is slightly higher than the corresponding value for this type of dosage and cement type (52.5 MPa) due to the treatment at 40 °C. For 400 °C, a value of 55 ± 3 MPa was obtained, being a small variation (reduction in 12 %) from the initial value due to the stiffness loss of the matrix and the degradation of the interfacial transition zone between the paste and the aggregate. At 525 °C compressive strength falls dramatically obtaining 27 ± 2 MPa, loosing at least the 56 % of its initial strength. A similar trend in performance can be found for flexural strength (Figure 3.4.2b. It can be noted that this parameter is more sensitive to the thermal damage than compressive strength because spoiled interfaces, micro-cracks and defects are expected to be partially stressed with a tensile load. Reductions in flexural strengths of 40 % and 90 % were observed for 400 and 525 °C treated samples, respectively. In the case of compressive test, such defects are completely compressed, allowing it to withstand a higher stress than the tensions produced by the flexural test.

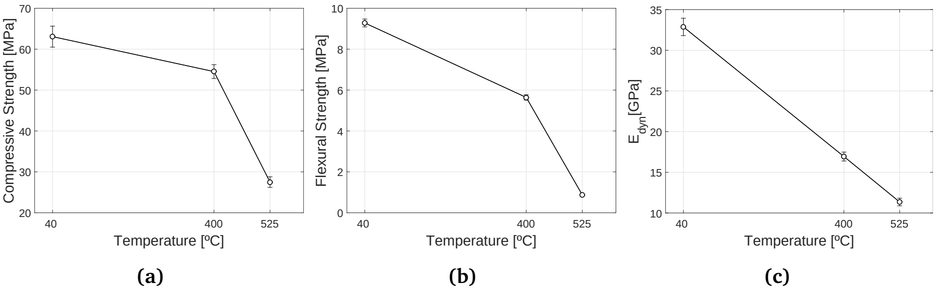

(a) (b) (c)

Figure 3.4.2: Mechanical properties as a function of exposure temperature: a) Compressive strength. b) Flexural strength. c) Transversal dynamic elastic modulus.

Figure 3.4.2c shows the dynamic modulus values calculated from the first flexural mode from the mortar specimens following ASTM C-215 standard. In this plot, a linear decay of the stiffness of the material can be observed. Linear modulus is related with the state of the cement matrix and, therefore, in the case of thermal attack, hydration products are lost during this process until the complete decomposition of portlandite (>550°C).

3.4.4.2 Resonance Techniques based on Impact Spectroscopy

Reproducibility Test

The discrete memory effects of the hysteretic behaviour have been reported in several studies [3, 24]. Impact spectroscopy techniques rely on the impact of a specimen at different amplitudes, so the importance of the order of the blows and their intensity must be taken into account. Therefore, two different configuration tests were raised: upward configuration, 10 blows progressively increasing the impact energy, and downward configuration, 10 blows decreasing the impact energy. To analyze the repeatability of the tests, five consecutive repetitions for each configuration were done. Given that memory recovery time follows $log(t)$ dependence, the test samples were left undisturbed for 48 hours between tests to ensure a consistent initial relaxed state of the material. The majority of the idealized memory recovery is achieved during the 48 hour rest period. Figure 3.4.3a plots the obtained results in the upward configuration for a representative specimen damaged at 400°C.

Two different trends can easily be identified: the first test (dashed line) shows a slope different than the remaining four tests (solid lines). Despite being parallel

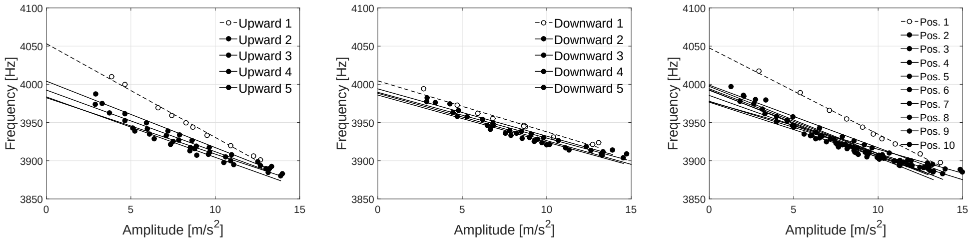

(a) **(b)** **(c)**

Figure 3.4.3: Reproducibility Tests. Repetitions of the resonance tests (10 different amplitude impacts) on the same specimen. a) Upward configuration (starting with the lowest energy impact), b) Downward configuration (starting with the highest energy impact), c) Upward configuration at different positions (Fig. 3.4.4).

lines differ on the y-axis intersection. This plot allows a graphical understanding of the anomalous non-linear concepts introduced in Section 3.4.1: fast dynamics, slow dynamics and conditioning. The slope of the linear regression indicated by the amplitude-dependent frequency shifts represents the fast dynamics behavior, which is constant from the second upward test. The decreasing intersection of each consecutive test with the y-axis represents a manifestation of the discrete memory, which is a manifestation of slow dynamics. The particular trend shown by the first test (dashed line) represents the behavior of the specimen without conditioning, when it is relaxed. Once the specimen is conditioned, after a series of blows has occurred, the observable trend are indicated by the solid lines. The specimen is conditioned in terms of fast dynamics (the slope of the linear fit is constant); however, the slow dynamics conditioning continue by decreasing the linear resonance frequency at each consecutive experiment.

Figure 3.4.3b shows the analysis of the five consecutive downward tests, where the specimen is completely conditioned from the very first and strongest impact and a constant trend is observed for the five test. Even though the specimen had relaxed, the linear regressions allow us to identify the same slope and y-axis interception than in the upward configuration after having been conditioned.

Previous tests were done by applying the impact event at one single position. To address concerns about measurement disruption cased by the hardening of the hit surface area, a further experiment has been done. In this case, 10 upward NIRAS configuration tests have been done in 10 different positions following Figure 3.4.4; five on the right-hand face of the specimen, and five on the left-hand face. The five positions are separated by 0.5 cm approximately (7-7.5-8-8.5-9). The obtained results are plotted in Figure 3.4.3c. Despite changing the hit position for each test, the same two different trends are identified: the first regression fit corresponds to the relaxed specimen, and the rest correspond to the conditioned specimen. To fully characterize the thermal damage given in the previous results, the specimens are tested using the two established configurations, an upward and a downward test, leaving 48 hours of resting time between tests.

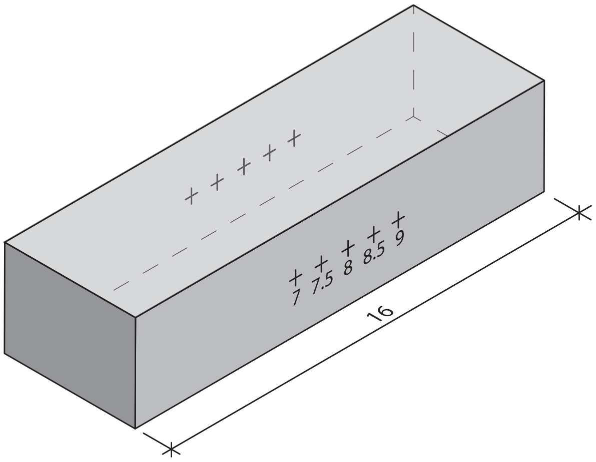

Figure 3.4.4: Testing configuration: impact sites indicated by crosses (in centimeters).

NIRAS and FANSIRAS analyses

In the present section, the non-linear parameters α_f and α_Q obtained both by NIRAS and FANSIRAS techniques are shown for three representative mortar samples at three different stages of thermal damage (40 °C, 400 °C and 525 °C). First, the two techniques for both configurations are compared to estimate the different trends arising from the conditioning effect and how it evolves along with the increasing deterioration degree of the specimens.

Figure 3.4.5 shows the effect of signal amplitude on the resonance frequency for each level of damage. It can be observed that the resonance frequency significantly drops as the damage increases (5670 Hz, 40 °C; 3890 Hz, 400 °C; and 3270 Hz, 525 °C). For the three levels of damage, the NIRAS technique (circle markers) identifies two different trends related to the applied configuration: upward (solid line) and downward (dashed line). However, the FANSIRAS algorithm (triangle markers) estimated over the strongest impact of the NIRAS technique results in a unique trend which coincides with the downward NIRAS trend. Table 3.4.1 summarizes the numerical values of α_f obtained by both algorithms NIRAS and FANSIRAS, and in each configuration. The differences between the NIRAS upward configuration and the NIRAS downward configuration seems to be proportional to the degree of conditioning of the system between the resting state and the excitation state. That conditioning angle increases as the applied thermal treatment damages the concrete matrix. The slight differences between α_f^{NIR} in the downward configuration and α_f^{FAN} are due to the differences in sensitivity of the techniques. The NIRAS algorithm has a limited range of amplitude values depending on the hardware involved in the experimental, however, FANSIRAS processing allows to increase the measurable dynamic range from smaller peak amplitudes up to the same largest value. This improves the reliability when estimating the linear regime parameters $\tilde{f}_0$ and Q_0.

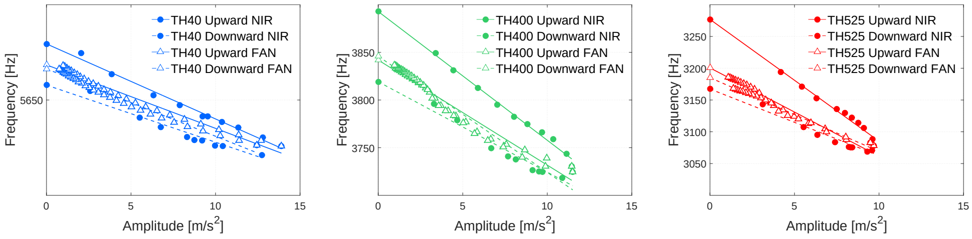

(a) **(b)** **(c)**

Figure 3.4.5: Representative results of the relative resonance frequency shift (α_f) at different exposure temperatures computed by the NIRAS technique (circle markers) and the FANSIRAS technique (triangle markers) and for the two analyzed different configurations: upward impact amplitudes (solid lines) and downward impact amplitudes (dashed line). a) 40°C (blue), b) 400°C (green) and c) 525°C (red). Table 3.4.1 summarizes the numerical values of α_f obtained by both algorithms NIRAS and FANSIRAS, and in each configuration.

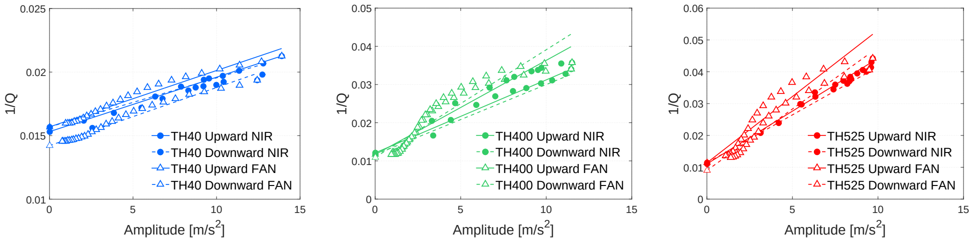

(a) **(b)** **(c)**

Figure 3.4.6: Representative results of the amplitude dependent damping factor (α_Q) at different temperatures computed by the NIRAS technique (circle markers) and the FANSIRAS technique (triangle markers) and for the two analyzed different configurations: upward impact amplitudes (solid lines) and downward impact amplitudes (dashed line). a) 40°C (blue), b) 400°C (green) and c) 525°C (red). Table 3.4.1 summarizes the numerical values of α_Q obtained by both algorithms NIRAS and FANSIRAS, and in each configuration.

Analogously, Figure 3.4.6 shows the amplitude-dependence for the damping factor Q for each level of damage. As the damage increases, the maximum value of the damping factor increases. Unlike the results for resonance frequency shift shown in Figure 3.4.5, the NIRAS technique (filled circles) does not distinguish differences between the upward (solid line) and downward (dashed line) con-

Table 3.4.1: Representative results of the relative resonance frequency shift (α_f) and the the amplitude dependent damping factor (α_Q) at different exposure temperatures (40°C, 400°C and 525°C) computed by the NIRAS technique and the FANSIRAS technique and for the two analyzed different configurations: upward impact amplitudes and downward impact amplitudes.

Sample	TH40		TH400		TH525	
(x10^{-3})	Upward	Downward	Upward	Downward	Upward	Downward
α_f^{NIR}	0.7	0.5	3.5	2.5	5.9	3.3
α_f^{FAN}	0.6	0.6	2.9	3.2	4.3	3.6
α_Q^{NIR}	0.4	0.4	1.9	1.8	3.3	3
α_Q^{FAN}	0.4	0.5	2.5	2.8	4.2	3.9

figurations. Thus, the damping factor computed by NIRAS algorithm seems to be robust against the conditioning of the specimen. Meanwhile, FANSIRAS algorithm (triangles) also allows the estimation of the damping factor, reaching similar values both for upward (solid line) and downward (dashed line) configurations. FANSIRAS estimations slightly differ from NIRAS estimations due to the lost of linearity in the regression fit as the damage increases. The damping factor data obtained with FANSIRAS exhibits a non-linear S—shaped trend with increasing signal amplitude, which is directly attributed to the estimation of the lowest bound of the resonance, $f_{i,1}$ (Eq. 3.4.12). This difference might be related to the nature of the signals used in each spectroscopy technique. NIRAS technique estimates non-linear parameters from several original reverberation signals; however, the FANSIRAS algorithm estimates the different strain levels from a single relaxing signal. Table 3.4.1 summarizes all the numerical values of α_Q obtained by both algorithms NIRAS and FANSIRAS, and in each configuration, upward and downward for three representative specimens exposed at different damage treatments.

It is important to understand the differences obtained by NIRAS and FANSIRAS. The first NIRAS upward configuration quantifies the non-linear parameters when the specimen is relaxed. This situation is not repeatable until the specimen reaches the relaxation stage once again. In contrast in the NIRAS downward configuration, the specimen is conditioned from the first driving impact, which is the largest and resulted in isolating the hysteretic parameter to the first impact. FANSIRAS technique applied over the strongest impact is not influenced by the kind of configuration used. The results shown in Figure 3.4.5 and Figure 3.4.6 have proven its robustness by virtue of using a single impact.

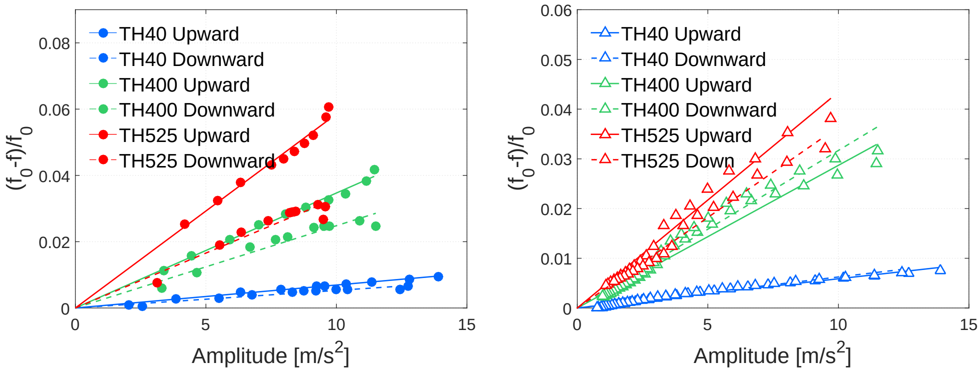

(a) **(b)**

Figure 3.4.7: Representative results of the normalized relative amplitude dependent damping factor (α_f) at different exposure temperatures: 40°C (blue), 400°C (green) and 525°C (red) computed by a) the NIRAS technique (circle markers) and b) the FANSIRAS technique (triangle markers) and for the two analyzed different configurations: upward impact amplitudes (solid lines) and downward impact amplitudes (dashed lines).

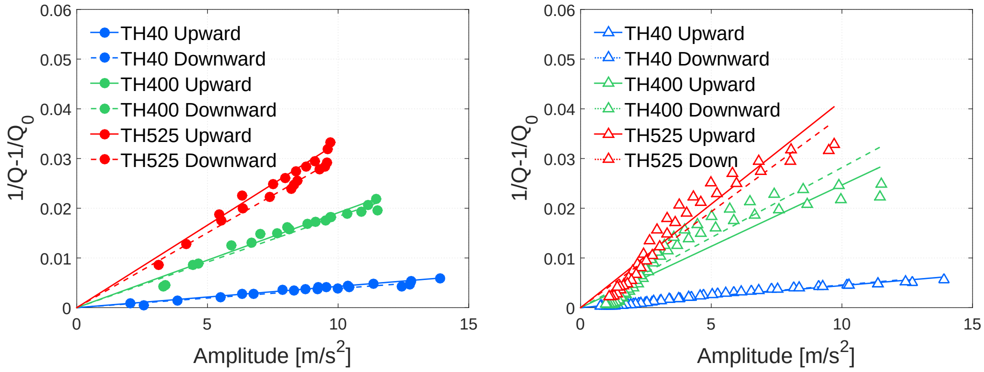

(a) **(b)**

Figure 3.4.8: Representative results of the normalized relative amplitude dependent damping factor (α_Q) at different exposure temperatures: 40°C (blue), 400°C (green) and 525°C (red) computed by a) the NIRAS technique (circle markers) and b) the FANSIRAS technique (triangle markers) and for the two analyzed different configurations: upward impact amplitudes (solid lines) and downward impact amplitudes (dashed line).

Once this conduct has been pointed out to have been influenced by the test configuration, the set of resonance frequencies and damping factor values, obtained by means of NIRAS and FANSIRAS, are normalized by its values at the linear strain regime to compare the different thermal level responses, for each technique separately, and obtain comparable outcomes.

It can be noticed in Figure 3.4.7a that NIRAS is excited by the upward configuration and displays larger non-linear parameters than those obtained with the downward configuration and FANSIRAS, as shown in Figure 3.4.7b. Without knowledge of the specimen impact history, the lack of consistency between previous states may lead to failure in damage level classification (see TH400 upward and TH525 downward). The FANSIRAS results show consistent trends, regardless of the two proposed configurations (Figure 3.4.7b. This research has also shown that the estimation of the damping factor is not influenced by the conditioning of the specimen under study (Figure 3.4.8). This behavior might be related to the nature of the Q parameter of a signal drawn by an harmonic damped oscillator, where the quality factor is the ratio between the system energy and consumed energy. This ratio seems to be more robust against the conditioning induced to the specimen impact after impact. Besides the steadiness shown when using the FANSIRAS technique regardless the excitation configuration used, characterization of thermal damage in each of the tested stages remains showing a very reliable sensitivity.

In order to understand the significance of the variation of the non-linear parameter values along with the increasing thermal damage, a comparison between α_f and α_Q parameters from a higher number of samples (6 at each of the proposed thermal damages for a total of 18 specimens) is shown in Figure 3.4.9. Figure 3.4.9a shows the resonance frequency shift amplitude-dependent parameter (α_f) in the same fashion Figure 3.4.9b shows it for the damping factor response (α_Q). The error bars depict the standard deviation of the set comprised by six α parameters computed for six independent specimens at each temperature degree. The markers, circles and triangles, denoting NIRAS and FANSIRAS techniques, respectively, represent the arithmetic mean of the aforementioned set. As was discussed in the previous results, the test configuration in impact resonance spectroscopy assessment plays an important role when quantifying the non-linear response of the material. At first, a significant divergence of the values was obtained by means of the NIRAS technique in the upward configuration regarding the other three evaluations taken into account in the present study. Thus, Figure 3.4.9 could be interpreted as a confirmation that the FANSIRAS technique seems to be robust when quantifying the α parameters. However, NIRAS upward seems sensitive to the a priori relaxed stage of the specimen. Regardless of the configuration used, FANSIRAS seems able to characterize accurately the microstructural degradation process, reproducing differentiated damage intervals and establishing a more stable evaluation scenario.

Finally, a comparison of the evolution of both non-linear parameters, α_f and α_Q, for both techniques and configurations is shown in Figure 3.4.10. It can be noticed that, regardless the level of damage, the non-linear parameters are very similar to FANSIRAS upward and downward configurations, and almost coincident

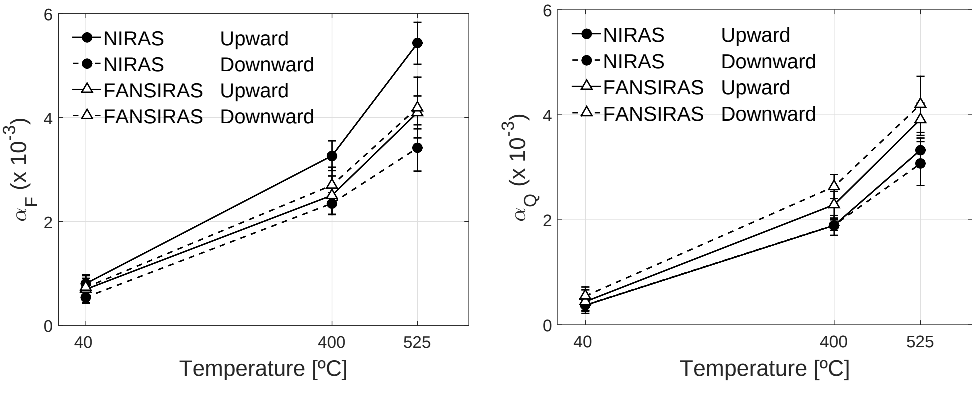

(a) **(b)**

Figure 3.4.9: Results of the non-linear hysteretic parameters at different exposure temperatures, $40°C$, $400°C$ and $525°C$, computed by the NIRAS technique (circle markers) and the FANSIRAS technique (triangle markers) and for the two analyzed different configurations: upward impact amplitudes (solid lines) and downward impact amplitudes (dashed line). The error bars depict the standard deviation of the set composed of six α parameters computed for six independent specimens at each level of exposure condition. a) Amplitude-dependent frequency shift (α_f). b) Amplitude-dependent damping factor (α_Q).

for NIRAS downward. This suggests that the results obtained by FANSIRAS are not affected by the dynamic hysteretic behavior of the material. Although both non-linear parameters must reproduce the same underlying phenomena, this similarity in the non-linear parameters has not previously been reported.

3.4.5 Conclusions

We studied the differences between impact resonance spectroscopy methods NIRAS and FANSIRAS through tests on thermally damaged mortar samples. Furthermore, the NIRAS tests were conducted using either sequentially increasing (upward) or decreasing (downward) load amplitudes. The upward and downward loading profiles allowed us to evaluate the effects of slow dynamic conditioning and recovery on the results. The mortar samples were exposed to sustained temperatures of 40 °C, 400 °C and 525 °C , providing different levels of thermal damage. The NIRAS results have shown that the non-linear hysteretic parameter related to the resonance frequency shift, α_f^{NIR}, differs between the upward and downward loading configurations. The NIRAS results as a function of the damage treatment show that differences between upward and downward series are greater as the level of damage increases. However, the results of the non-linear parameter related to the damping properties, α_Q^{NIR}, are equivalent for both upward and downward loading configurations. The damping factor, Q_i, was observed to be essentially unaffected by the slow dynamics and conditioning of the specimen.

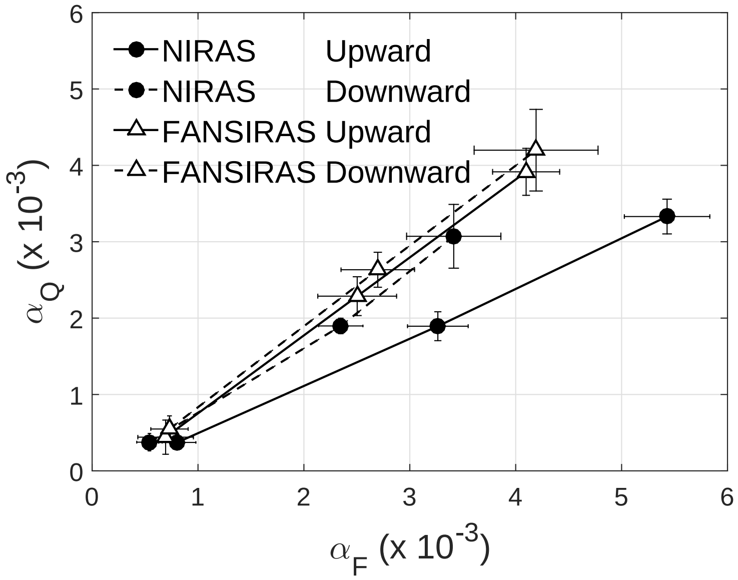

Figure 3.4.10: Comparison of the evolution of both hysteretic parameters, α_f and α_Q, for NIRAS and FANSIRAS, in upward and downward configurations. The error bars depict the standard deviation of the set composed of six α parameters computed for six independent specimens at each temperature condition.

The FANSIRAS algorithm extracts results from a single resonant signal that are equivalent results to NIRAS when the specimen is conditioned. When the specimen has been previously tested, both of the parameters α_f and α_Q obtained by NIRAS in the downward configuration and FANSIRAS are equivalent.

The disrupting effects of slow dynamic conditioning on NIRAS tests using the conventional upward loading configuration have been shown to be significant. However, erroneous conclusions related to the level of damage may be made if the previous relaxed or conditioned state of the specimen under study is not taken into account. Meanwhile, the data analyzed by the FANSIRAS algorithm are largely unaffected by slow dynamic or hysteretic effects.

Acknowledgements

This work has been supported by the Spanish Administration under grants BES2015-071469, PEJ-2014-P-00112, BIA2014-55311-C2-1-P and BIA2014-55311-C2-2-P.

References

[1] R. A. Guyer and P. A. Johnson, “Nonlinear Mesoscopic Elasticity: Evidence for a New Class of Materials,” *Physics Today*, vol. 52, no. 4, p. 30, 1999.

[2] L. D. Landau and E. M. Lifshitz, *Theory of Elasticity*, 3rd. Oxford, England: Pergamon, 1986.

[3] P. Johnson and A. Sutin, “Slow dynamics and anomalous nonlinear fast dynamics in diverse solids,” *The Journal of the Acoustical Society of America*, vol. 117, no. 1, pp. 124–130, 2005.

[4] K. Van Den Abeele, J. Carmeliet, J. A. Ten Cate, and P. Johnson, “Nonlinear ElasticWave Spectroscopy (NEWS) Techniques to Discern Material Damage, Part I: Nonlinear Wave Modulation Spectroscopy (NWMS),” *Research in Nondestructive Evaluation*, vol. 12, no. 1, pp. 17–30, 2000.

[5] L. Ostrovsky and P. A. Johnson, “Dynamic nonlinear elasticity in geomaterials,” *Rivista del Nuovo Cimento*, vol. 24, pp. 1–46, 2001.

[6] K. Van Den Abeele, P. A. Johnson, and A. Sutin, “Nonlinear Elastic Wave Spectroscopy (NEWS) Techniques to Discern Material Damage, Part II: Single-Mode Nonlinear Resonance Acoustic Spectroscopy,” *Research in Nondestructive Evaluation*, vol. 12, no. 1, pp. 17–30, 2000.

[7] J. Chen, A. R. Jayapalan, J. Y. Kim, K. E. Kurtis, and L. J. Jacobs, “Rapid evaluation of alkali-silica reactivity of aggregates using a nonlinear resonance spectroscopy technique,” *Cement and Concrete Research*, vol. 40, no. 6, pp. 914–923, 2010.

[8] C. Payan, T. J. Ulrich, P. Y. Le Bas, T. Saleh, and M. Guimaraes, “Quantitative linear and nonlinear resonance inspection techniques and analysis for material characterization: Application to concrete thermal damage.,” *The Journal of the Acoustical Society of America*, vol. 136, no. 2, p. 537, 2014.

[9] V. Genovés, J. Gosálbez, R. Miralles, L. Soriano, and J. Payá, “Ultrasonic monitoring on glass fiber reinforced cement (GRC) bending test,” *Materials Characterization*, vol. 90, pp. 149–158, 2015.

[10] J. N. Eiras, J. Monzó, J. Payá, T. Kundu, and J. S. Popovics, “Non-classical nonlinear feature extraction from standard resonance vibration data for damage detection,” *The Journal of the Acoustical Society of America*, vol. 135, no. 2, EL82–EL87, 2014.

[11] U. Dahlen, N. Ryden, and A. Jakobsson, “Damage identification in concrete using impact non-linear reverberation spectroscopy,” *NDT & E International*, vol. 75, pp. 15–25, 2015.

[12] A. Carrión, V. Genovés, G. Pérez, J. Payá, and J. Gosálbez, “Flipped accumulative non-linear single impact resonance acoustic spectroscopy (fansiras): A novel feature extraction algorithm for global damage assessment,” *Journal of Sound and Vibration*, vol. 432, pp. 454–469, 2018.

[13] P. C. Aïtcin, *Binders for durable and sustainable concrete*. CRC Press, 2014.

[14] J. Skalny and J. Marchand, *Sulphate attack on concrete*. Spon Press, 2002.

[15] M. Alexander and S. Mindess, *Aggregates in concrete*. CRC Press, 2010.

[16] U. Schneider, “Concrete at high temperatures - A general review,” *Fire Safety Journal*, vol. 13, no. 1, pp. 55–68, 1988.

[17] Q. Ma, R. Guo, Z. Zhao, Z. Lin, and K. He, “Mechanical properties of concrete at high temperature-A review,” *Construction and Building Materials*, vol. 93, pp. 371–383, 2015.

[18] V. Malhotra and N. Carino, *Handbook on Nondestructive Testing of Concrete*, ser. Civil engineering. CRC Press, 2004.

[19] S. J. Park, H. J. Yim, and H. G. Kwak, “Nonlinear resonance vibration method to estimate the damage level on heat-exposed concrete,” *Fire Safety Journal*, vol. 69, pp. 36–42, 2014.

[20] V. Genovés, F. Vargas, J. Gosálbez, A. Carrión, M. Borrachero, and J. Payá, “Ultrasonic and impact spectroscopy monitoring on internal sulphate attack of cement-based materials,” *Materials & Design*, vol. 125, pp. 46–54, 2017.

[21] K. J. Leśnicki, J. Y. Kim, K. E. Kurtis, and L. J. Jacobs, “Characterization of ASR damage in concrete using Nonlinear Impact Resonance Scoustic Spectroscopy technique,” *NDT & E International*, vol. 44, no. 8, pp. 721–727, 2011.

[22] C. Payan, V. Garnier, J. Moysan, and P. A. Johnson, “Applying nonlinear resonant ultrasound spectroscopy to improving thermal damage assessment in concrete,” *The Journal of the Acoustical Society of America*, vol. 121, no. 4, EL125, 2007.

[23] J. A. TenCate, “Slow dynamics of earth materials: An experimental overview,” *Pure and Applied Geophysics*, vol. 168, no. 12, pp. 2211–2219, 2011.

[24] R. A. Guyer, K. R. McCall, and K. Van Den Abeele, “Slow elastic dynamics in a resonant bar of rock,” *Geophysical Research Letters*, vol. 25, no. 10, pp. 1585–1588, 1998.

Chapter 4

Conclusions and future research

4.1 Conclusions

This thesis has different chapters with their objectives; thus, in every section of each chapter, particular conclusions were commented. Therefore, general and specific conclusions, with an overview of the accomplished work, are described below.

After testing hundreds of specimens, processing thousands of signals, analysing large amounts of datasets, the general conclusion we have reached is that each NDT parameter responds to a different underlying phenomena. Therefore, the best way to analyse and characterise materials lies in understanding linear and non-linear variables from different sources and natures in NDT, aversely to the general thinking in this field: non-linear parameters are more sensitive than the linear ones. Thus, the understanding of each NDT technique and signal processing algorithm is essential to get as much information as possible without invading the integrity of the specimen under study. Following this line of thinking, in Chapter 2 we described how a complete overview of a complex material under stress is achieved analysing different ultrasonic parameters of the same wave travelling trough the specimen. One of the achievements was to obtain several ultrasonic parameters (attenuation, velocity, non-linear relations...) at the same time as the 4 bending test being carried out. Each one has an exclusive information about the test, but only having in mind the evolution of each one individually we see the complete response of the system, reporting very valuable information about the performance of the GRC.

The following specific conclusions were selected from Chapter 2. Ultrasonic tests allowed distinguishing fly ash containing GRC with different water/binder ratio and provided additional information on the materials behaviour and mechanical parameters. The attenuation curves could be used to establish a relationship between the porosity parameters and some mechanical properties extracted from a four-point bending test. The P-wave velocity was also stable and indicated a strong relationship with the elastic modulus.

The bending test process of glass fiber reinforced cement (GRC) has been successfully monitored by means of the study of ultrasonic pulses. In the beginning of the plastic step in the mechanical bending test, significant changes in energy, attenuation and non-linearities (the ratio between the amplitude of the fundamental harmonic, A1, and the amplitude of the third harmonic, A3) were identified. However, the change in the velocity pulse was much less sensitive.

Linear swept-frequency ultrasonic signals (chirp) improve the effective bandwidth, covering a wide frequency range with a single measurement and equivalent accuracy, at the expense of a lower signal-to-noise ratio. In the case of highly attenuating materials, the use of different configurations of chirp signals was proposed, enabling injecting more energy, and therefore, improving the sensitivity of the technique without a high time cost.

A new method based on broadband signals (chirp) for monitoring bending tests in GRC provides a wealth of information about the material behaviour in terms of the attenuation, energy, velocity, and generation of non-linear harmonics in the signal. The energy and attenuation of the chirp signal were more sensitive than velocity, showing a significant variation previous to the plastic step of the stress–strain curve. Attenuation was more appropriate for comparing different materials and tests. The non-linearity had a sudden change as the micro-cracking began, pointing perfectly to the time instant when the GRC specimen is being critically damaged.

In Chapter 3 we tried to understand the complexity of non-linear dynamics in mesoscopic materials. This kind of effect, composed by different phenomena, is still today difficult to control due to the high influence of the memory, environmental conditions and the inner state of the system. The development of a new algorithm allowed us to understand much better the reverberation behaviour of a material under an impact excitation and solved problems about the layout and the way we test our samples. More research about fast and slow dynamics and the effect of the conditioning is needed to exploit the potential of this property in damage characterisation.

The following specific conclusions were selected from Chapter 3. NIRAS is a suitable technique to evaluate ageing process for GRC specimens. Different vibrational modes have been evaluated over a frequency range in order to compare the variations of linear and non-linear parameters with ageing. It is observed that non linear parameters are more sensitive to ageing than linear ones. Impact acoustic resonance spectroscopy and ultrasonic measures have shown the accuracy of these non-destructive techniques applied to detect and characterize an internal sulphate attack process. The dynamic modulus and ultrasonic pulse velocity have closely predicted the stiffness of the specimens. The attenuation monitoring is an interesting procedure for the assessment of low-level expansion processes in mortars which have suffered an internal sulphate attack.

The study on thermal damaged concrete demonstrated the suitability of FAN-SIRAS algorithm by means of resonance spectroscopy, but also, to shed light on the need for right practises when applying such a popular technique like NIRAS. If the previous state of the specimen under study is not taken into account, relaxed or conditioned states, erroneous conclusions may be made.

The complete characterisation of thermal damage in mortar allowed to understand the different damage mechanisms in this spoiling procedure. The NDT tests revealed different sensitivity to the matrix degradations and the incompatibility of deformation between the aggregate and the cement paste. Ultrasonic attenuation and hysteretic parameter appeared to be sensitive to the changes in the interface between paste and aggregate; also, the UPV and dynamic modulus showed proportionality to the stiffness loss of the cement paste.

4.2 Future research

Mechanical test monitoring with ultrasonic signals was an important part of this thesis. The application of the developed measurement systems to other materials and tests has an important value. Hotspot tests like shrinkage and creeping in concrete samples are very important fields of work with a lot of interest in the scientific communities. Providing more parameters from mechanical waves will shed some light to try to understand and characterise these deferred effects over time. Developing new techniques and advanced signal processing algorithms has been an important point in this thesis. For issues related to the norms established for doctoral thesis publications, this part has not been included in the written version of this document but the reader can find this publications in Chapter 5. We think that developing this kind of new techniques with advanced signal processing algorithms, that allows to increase the amount of information extracted from a system under changes, is really interesting and important for scientific communities. The technique developed with signal modality evaluation opened a new way to process ultrasonics to see the scale of inhomogeneities inside materials.

To continue exploring the potential of this technique in different kind of damage and materials more tests and variable analysis will be essential. In short-medium term our efforts are completely focused in understanding the slow and fast dynamics interactions and the effect of memory and conditioning in mesoscopic materials. We found this critical, not only because it is necessary to control the damage detection but also for the curiosity and the necessity to deeply understand a complex behaviour like that. For this, the understanding and comparison between techniques is required. A lot of authors are focused in these kind of nonlinear hysteretic techniques, giving values and parameters which are proportional to each other but without giving any correlation between them. At this moment there is a current investigation with other research groups to try to understand this phenomena, correlating different techniques like NRUS, NIRAS or DAET. The exchange of knowledge, the multidisciplinary collaboration and the continuous finding of synergies between researchers and groups will boost our scientific work improving the understanding of signals and materials.

Chapter 5

Publications and developed activities

5.1 Peer review ISI Journals

- V. Genovés, L. Soriano, M.V. Borrachero, J. Eiras, J. Payá, Preliminary study on short-term sulphate attack evaluation by non-linear impact resonance acoustic spectroscopy technique, Construction and Building Materials, vol. 78, pp. 295-302, 2015.

- V. Genovés, C. Riestra, M.V. Borrachero, J. Eiras, T. Kundu, J. Payá, Multimodal analysis of GRC ageing process using non-linear impact resonance acoustic spectroscopy, Composites Part B: Engineering, vol. 76, pp. 105-111, 2015.

- V. Genovés, J. Gosálbez, R. Miralles, M. Bonilla, J. Payá, Ultrasonic characterization of GRC with high percentage of fly ash substitution, Ultrasonics, vol. 60, pp. 88-95, 2015.

- V. Genovés, J. Gosálbez, A. Carrión, R. Miralles, J. Payá, Optimized ultrasonic attenuation measures for non-homogeneous materials, Ultrasonics, vol. 65, pp. 345-352, 2016.

- V. Genovés, J. Gosálbez, A. Carrión, R. Miralles, J. Payá, Ultrasonic broadband signals monitoring of glass-fiber reinforced cement (GRC) bending tests, Cement and Concrete Composites, vol. 80, pp. 55-63, 2017.

- V. Genovés, F. Vargas, J. Gosálbez, A. Carrión, M.V. Borrachero, J. Payá, Ultrasonic and impact spectroscopy monitoring on internal sulphate attack of cement-based materials, Materials & Design, vol. 125, pp. 46-54, 2017.
- A. Carrión, V. Genovés, J. Gosálbez, R. Miralles, J. Payá, Ultrasonic signal modality: A novel approach for concrete damage evaluation, Cement and Concrete Research, vol. 101, pp. 25-32, 2017.
- A. Carrión, V. Genovés, G. Pérez, J. Payá, J. Gosálbez, Flipped Accumulative Non-Linear Single Impact Resonance Acoustic Spectroscopy (FANSIRAS): A novel feature extraction algorithm for global damage assessment, Journal of Sound and Vibration, vol. 432, pp. 454-469. 2018.
- J. Gosálbez, W.M.D. Wright, W. Jiang, A. Carrión, V. Genovés, I. Bosch, Airborne non-contact and contact broadband ultrasounds for frequency attenuation profile estimation of cementitious materials, Ultrasonics, vol. 88, pp. 148-156. 2018.
- A. Carrión, V. Genovés, G. Pérez, J. Bittner, J. S. Popovics J. Payá, J. Gosálbez, Effects of slow dynamics and conditioning on non-linear hysteretic material evaluation, Journal of American Society of Acoustics, (*Submitted*).
- V. Genovés, A. Carrión, D. Escobar, J. Gosálbez, J. Monzó, M.V. Borrachero, J. Payá, non-linear acoustic spectroscopy and frequency sweep ultrasonics: Case on thermal damage assessment in concrete, Journal of Nondestructive Evaluation, (*Submitted*).

5.2 International Conferences

- J. Eiras, V. Genovés, L. Soriano, M. Tashima, J. Popovics, J. Payá. Evaluación del ataque por sulfatos en morteros de cemento Portland mediante técnicas no destructivas, IBRACON, 54 Congreso Brasileiro do Concreto, Algoas (Brazil), 2012.
- J. Gosálbez, V. Genovés, I. Bosch, R. Miralles, TOFD feasibility for characterizing cracks in historical stone materials, AEND, ART ’14 Madrid (Spain), 2014.
- J. Gosálbez, V. Genovés, I. Bosch, R. Miralles, Analysis of st. Nicolas church by means ground penetrating radar technique, AEND, ART ’14, Madrid (Spain), 2014.

- V. Genovés, J. Gosálbez, R. Miralles, L. Soriano, J. Payá, Ultrasonic monitoring on glass fiber reinforced cement (GRC) bending test, University of Wessex, Materials Characterisation, València (Spain), 2015.
- V. Genovés, A. Carrión, J. Gosálbez, I. Bosch, M.V. Borrachero, J. Payá, Optimized Ultrasonic Attenuation Measures for Internal Sulphate Attack Monitoring in Portland Cement Mortars, IEEE International Ultrasonics Symposium, Washington, DC (United States of America), 2017.
- A. Carrión, V. Genovés, R. Miralles, J. Payá, J. Gosálbez, An Advanced Ultrasonic Method based on Signal Modality for Structural Damage Characterization on Concrete: The Cube Problem, IEEE International Ultrasonics Symposium, Washington, DC (United States of America), 2017.
- V. Genovés, A. Carrión, J. Payá, J. Gosálbez, A new non-linear impact resonance acoustic spectroscopy algorithm: FANSIRAS, ISNA/ICNEM, International Symposium of non-linear Acoustics, Santa Fe, NM (United States of America), 2018.

5.3 National Conferences

- J. Gosálbez, V. Genovés, J.R. Albiol, Análisis mediante TOFD para la caracterización de grietas y grado de consolidación. REHABEND, Santander, 2014.
- A. Carrión, R. Miralles, V. Genovés, J. Gosálbez, J. Payá, Nuevo método ultrasónico basado en el determinismo. Aplicación al caso de daño térmico en morteros de cemento Portland. I Congreso Nacional PRE-CONPAT 16, Madrid, 2016.
- V. Genovés, D. Escobar, A. Carrión, J. Gosálbez, J. Monzó, M.V. Borrachero, J. Payá Bernabeu, Comparación de dos técnicas no destructivas (Ultrasonidos y espectroscopía acústica) aplicadas en la caracterización de hormigones con daño térmico. II Congreso Nacional PRE-CONPAT 18, Alicante, 2018.

5.4 Patents

- A. Carrión, V. Genovés, J. Gosálbez, R. Miralles, J. Payá, Método de Ensayo del Estado de Materiales, Universitat Politècnica de València, P201630212, Spain, Community of Madrid, 2016.

5.5 Institutional acknowledgements

- Ayuda Subprograma de Formación de Personal Investigador (BES-2015-071469).
- Estudio del comportamiento no lineal de ondas mecánicas para la caracterización de materiales basados en el cemento y su durabilidad (BIA 2010-19933).
- Nuevas Aplicaciones de Ensayos No Destructivos basados en Ondas Mecánicas para la Evaluación de la Degradación en Materiales Cementantes (BIA2014-55311-C2-1-P).

Bibliography

[1] V. Genovés, J. Gosálbez, R. Miralles, M. Bonilla, and J. Payá, "Ultrasonic characterization of grc with high percentage of fly ash substitution," *Ultrasonics*, vol. 60, pp. 88–95, 2015.

[2] V. Genovés, J. Gosálbez, R. Miralles, L. Soriano, and J. Payá, "Ultrasonic monitoring on glass fiber reinforced cement (grc) bending test," in *Materials Characterisation VII*, vol. 90, WIT Transactions on Engineering Sciences, 2015, pp. 149–158.

[3] V. Genovés, J. Gosálbez, R. Miralles, A. Carrión, and J. Payá, "Optimized ultrasonic attenuation measures for non-homogeneous materials," *Ultrasonics*, vol. 65, pp. 345–352, 2016.

[4] V. Genovés, J. Gosálbez, A. Carrión, R. Miralles, and J. Payá, "Ultrasonic broadband signals monitoring of glass-fiber reinforced cement (grc) bending tests," *Cement and Concrete Composites*, vol. 80, pp. 55–63, 2017.

[5] V. Genovés, C. Riestra, M. Borrachero, J. Eiras, T. Kundu, and J. Payá, "Multimodal analysis of grc ageing process using nonlinear impact resonance acoustic spectroscopy," *Composites Part B: Engineering*, vol. 76, pp. 105–111, 2015.

[6] V. Genovés, F. Vargas, J. Gosálbez, A. Carrión, M. Borrachero, and J. Payá, "Ultrasonic and impact spectroscopy monitoring on internal sulphate attack of cement-based materials," *Materials & Design*, vol. 125, pp. 46–54, 2017.

[7] V. Genovés, A. Carrión, D. Escobar, J. Gosálbez, J. Monzó, M. Borrachero, and J. Payá, "Nonlinear acoustic spectroscopy and frequency sweep ultrasonics: Case on thermal damage assessment in concrete," *Journal of Nondestructive Testing*, 2018.

[8] A. Carrión, V. Genovés, G. Pérez, J. Bittner, J. Popovics, J. Payá, and J. Gosálbez, "Effects of slow dynamics and conditioning on non-linear hysteretic material evaluation," *Journal of American Society of Acoustics*, 2018.

Epilogue

This thesis has been developed under very particular circumstances. In a more personal way, I think that the main conclusion I can extract from this work is that the best thing you can do in science and research, no matter the field, no matter the topic, is sharing knowledge with other people: the disposition and availability to learn about everything and the desire to train your creativity to solve issues. It is much more valuable to learn how people solve and face problems in science than the result itself. Knowledge is usually in books and papers but attitude, determination and passion are not.

List of Figures

List of Tables